

1-1-2008

Enhanced detection of induced fluorescence from residual radioactive materials

Craig-Alan Crawford Bias
University of Nevada, Las Vegas

Follow this and additional works at: <https://digitalscholarship.unlv.edu/rtds>

Repository Citation

Bias, Craig-Alan Crawford, "Enhanced detection of induced fluorescence from residual radioactive materials" (2008). *UNLV Retrospective Theses & Dissertations*. 2808.
<http://dx.doi.org/10.25669/z5l6-vsd7>

This Dissertation is protected by copyright and/or related rights. It has been brought to you by Digital Scholarship@UNLV with permission from the rights-holder(s). You are free to use this Dissertation in any way that is permitted by the copyright and related rights legislation that applies to your use. For other uses you need to obtain permission from the rights-holder(s) directly, unless additional rights are indicated by a Creative Commons license in the record and/or on the work itself.

This Dissertation has been accepted for inclusion in UNLV Retrospective Theses & Dissertations by an authorized administrator of Digital Scholarship@UNLV. For more information, please contact digitalscholarship@unlv.edu.

ENHANCED DETECTION OF INDUCED FLUORESCENCE
FROM RESIDUAL RADIOACTIVE MATERIALS

by

Craig-Alan Crawford Bias

Bachelor of Science
Michigan State University
1989

Master of Engineering
Old Dominion University
1995

Master of Science
Colorado State University
2002

A dissertation submitted in partial fulfillment
of the requirements for the

**Doctor of Philosophy Degree in Radiochemistry
Department of Chemistry
College of Science**

**Graduate College
University of Nevada, Las Vegas
August 2008**

UMI Number: 3338178

INFORMATION TO USERS

The quality of this reproduction is dependent upon the quality of the copy submitted. Broken or indistinct print, colored or poor quality illustrations and photographs, print bleed-through, substandard margins, and improper alignment can adversely affect reproduction.

In the unlikely event that the author did not send a complete manuscript and there are missing pages, these will be noted. Also, if unauthorized copyright material had to be removed, a note will indicate the deletion.

UMI[®]

UMI Microform 3338178

Copyright 2009 by ProQuest LLC.

All rights reserved. This microform edition is protected against unauthorized copying under Title 17, United States Code.

ProQuest LLC
789 E. Eisenhower Parkway
PO Box 1346
Ann Arbor, MI 48106-1346

Copyright by Craig-Alan Crawford Bias 2008
All Rights Reserved



Dissertation Approval

The Graduate College
University of Nevada, Las Vegas

August 1, 2008

The Dissertation prepared by

Craig-Alan Crawford Bias

Entitled

Enhanced Detection of Induced Fluorescence from Residual Radioactive Materials

is approved in partial fulfillment of the requirements for the degree of

Doctor of Philosophy in Radiochemistry

Examination Committee Chair

Dean of the Graduate College

Examination Committee Member

Examination Committee Member

Graduate College Faculty Representative

ABSTRACT

Enhanced Detection of Induced Fluorescence from Residual Radioactive Materials

by

Craig-Alan Crawford Bias

Dr. Kenneth Czerwinski, Committee Chair
Associate Professor of Chemistry
University of Nevada, Las Vegas

Radiation detection is often hampered by signal losses and noise. Conversion of decay particle energy to photons by scintillation, or induction of emissions from fluorescent materials by laser excitation, offers improved signal-to-noise ratios and the possibility of remote detection. This dissertation investigates the enhancement of induced fluorescence afforded by the application of scintillator-loaded polymer films to a radioactive material and of silanol ligand solutions to a fluorescent material.

Prompt ultraviolet fluorescence from barium fluoride (BaF_2)-loaded polymer films was induced by exposure to a ^{99}Tc source and measured by scintillation counting. Scintillation photons suffer less attenuation in media than do the ^{99}Tc beta particles and occur in a region of negligible solar background. Films with BaF_2 loaded between 0 and 80% were drawn to thicknesses between 508 and 1270 μm . BaF_2 crystals, from 0.25 and 5 μm diameter as determined by scanning electron microscopy (SEM), are significantly likely to scatter ultraviolet scintillations, thereby increasing the potential for photon absorption by EVA with a resulting decrease in detectable yield. Scintillation intensity was maximized in thin films (102 μm dry thickness) with high loading (80% by mass).

Visible fluorescence from uranyl perchlorate solids contacted with Fe(III) or functionalized polyhedral oligomeric silsesquioxanes (POSS[®]) is induced by light from a 414-nm pulsed laser, and the time-resolved intensities and lifetimes measured by intensified charge-coupled device (CCD) camera at 23 °C. Uranyl lifetimes were $4.08 \pm 0.02 \mu\text{s}$ for a $4.8 \pm 0.2 \text{ mM UO}_2(\text{ClO}_4)_2$ (aq) solution and $225 \pm 2 \mu\text{s}$ for a $0.048 \mu\text{mol UO}_2(\text{ClO}_4)_2$ solid. With 8.85 times molar excess Fe(III) added, dynamically quenched lifetimes were $3.73 \pm 0.03 \mu\text{s}$ for the $4.8 \pm 0.2 \text{ mM UO}_2(\text{ClO}_4)_2$ (aq) solution and $124 \pm 5 \mu\text{s}$ for the $0.048 \mu\text{mol UO}_2(\text{ClO}_4)_2$ solid. Fluorescence spectra of solids were red-shifted by 6 nm for each maximum due to increased hydrolysis of the uranyl ion.

The effects of ligands in 4.2 times molar excess to UO_2^{2+} were determined by dissolution in buffered ethanol and deposition onto solid $\text{UO}_2(\text{ClO}_4)_2$. Uranyl fluorescence intensity was quenched by both ligand solutions by more than ten fold. The lifetimes were reduced from $\tau_o = 225 \pm 2 \mu\text{s}$ to $\tau = 66 \mu\text{s}$ for TriSilanolEthyl POSS[®] SO1444 and to $\tau = 77 \mu\text{s}$ for TetraSilanolPhenyl POSS[®] SO1460Na, indicating increased shielding of uranyl from ethanol quenching by POSS[®] SO1460Na. The additional effects of Fe^{3+} in 8.85 times molar excess to UO_2^{2+} were determined by deposition of these ligand solutions onto solids containing $\text{UO}_2(\text{ClO}_4)_2$ and $\text{Fe}(\text{ClO}_4)_3$. Fluorescence intensity was further quenched to by more than twenty five fold. Lifetimes of $\tau = 13 \mu\text{s}$ for POSS[®] SO1444 and $\tau = 46 \mu\text{s}$ for POSS[®] SO1460Na were measured.

The feasibility of enhanced detection of surface radioactive materials using induced fluorescence measurements is demonstrated, and improved methods, including the use of nanoparticle scintillators, phosphate-based solutions, and ion imprinted polymers are recommended.

TABLE OF CONTENTS

ABSTRACT	iii
LIST OF FIGURES	viii
LIST OF TABLES	x
ACKNOWLEDGEMENTS	xi
CHAPTER 1 INTRODUCTION	1
1.1 Problem.....	1
1.2 Research Goals and Objectives.....	3
1.2.1 Radioactive Material-Induced Fluorescence Experiments	3
1.2.2 Laser-Induced Fluorescence Experiments	4
CHAPTER 2 ANALYTICAL AND CHARACTERIZATION TECHNIQUES.....	6
2.1 Introduction to Absorption and Fluorescence Spectrometry	6
2.2 Principles of Ultraviolet-Visible Absorption Spectrometry	8
2.3 Principles of Scintillation Counting.....	9
2.4 Principles of Atomic Emission Spectrometry	11
2.5 Principles of Visible Fluorescence Spectrometry	12
CHAPTER 3 RADIOACTIVE MATERIAL-INDUCED FLUORESCENCE EXPERIMENTS	14
3.1 Introduction.....	14
3.2 Background.....	15
3.3 Experimental.....	16
3.3.1 Materials and Instrumentation	16
3.3.1.1 Chemicals.....	17
3.3.1.2 Scintillator.....	18
3.3.1.3 Radioactive Material Source.....	18
3.3.1.4 Equipment.....	19
3.3.1.5 Scintillation Counting Instrumentation.....	19
3.3.2 Polymer Film Preparation and Evaluation.....	20
3.3.2.1 Polymer Solution Preparation and Evaluation.....	20
3.3.2.2 Polymer Film Preparation and Evaluation.....	20
3.3.3 BaF ₂ Characterization	21
3.3.3.1 UV-Visible Absorption Measurements.....	21
3.3.3.2 Scanning Electron Microscopy	22
3.3.4 BaF ₂ -Loaded Polymer Film Preparation.....	22
3.3.4.1 BaF ₂ -Loaded Polymer Solution Preparation.....	22

3.3.4.2	BaF ₂ -Loaded Polymer Film Preparation.....	23
3.3.5	BaF ₂ -Loaded Polymer Film Characterization.....	23
3.3.5.1	UV-Visible Transmittance Measurements.....	23
3.3.5.2	Scintillation Counting.....	24
3.4	Results and Discussion	26
3.4.1	Polymer Solution and Film Evaluation.....	26
3.4.1.1	Polymer Solution Evaluation	26
3.4.1.2	Polymer Film Evaluation	27
3.4.2	BaF ₂ Characterization	28
3.4.2.1	UV-Visible Absorption Measurements.....	28
3.4.2.2	Scanning Electron Microscopy	28
3.4.3	BaF ₂ -Loaded Polymer Film Characterization.....	29
3.4.3.1	UV-Visible Transmittance Measurements.....	30
3.4.3.2	Scintillation Counting.....	32
3.5	Conclusions.....	43
CHAPTER 4	LASER-INDUCED FLUORESCENCE EXPERIMENTS	45
4.1	Introduction.....	45
4.2	Background.....	46
4.2.1	Uranyl Fluorescence Intensity	46
4.2.2	Uranyl Fluorescence Quenching.....	48
4.2.3	Uranyl Fluorescence Lifetime.....	50
4.2.4	Uranium Speciation	50
4.3	Experimental.....	51
4.3.1	Materials and Methods.....	51
4.3.1.1	Chemicals.....	52
4.3.1.2	Filters	53
4.3.1.3	pH Measurements	54
4.3.1.4	UV-Visible Absorption Spectrometry	54
4.3.1.5	Inductively Coupled Plasma-Atomic Emission Spectrometry	55
4.3.1.6	Laser Fluorescence Intensity Measurements	55
4.3.1.7	Laser Fluorescence Lifetime Measurements	60
4.3.2	Stock Solution Preparation	62
4.3.2.1	Uranyl Perchlorate Solution.....	62
4.3.2.2	Iron(III) Perchlorate Solution	62
4.3.2.3	Ethanol Solutions	63
4.3.3	Sample Preparation	64
4.3.3.1	Aqueous Solution Samples	64
4.3.3.2	POSS [®] Solution Samples.....	64
4.3.3.3	Solid Samples.....	65
4.3.3.4	Residue Samples	66
4.4	Results and Discussion	68
4.4.1	Stock Solution Characterization	68
4.4.1.1	Uranyl Perchlorate Solution.....	68
4.4.1.2	Iron(III) Perchlorate	70
4.4.2	Effect of Iron on Uranyl Fluorescence.....	71
4.4.2.1	Solid Sample Fluorescence Intensity Measurements.....	71

4.4.2.2	Solid Sample Fluorescence Lifetime Measurements	72
4.4.3	Effect of POSS® on Uranyl Fluorescence	74
4.4.3.1	Solution and Filtrate pH Measurements	74
4.4.3.2	Filtrate and Residue Fluorescence Intensity Measurements	75
4.4.3.3	Residue Fluorescence Lifetime Measurements	80
4.4.4	Effect of Iron and POSS® on Uranyl Fluorescence	81
4.4.4.1	Solution and Filtrate pH Measurements	81
4.4.4.2	Filtrate and Residue Fluorescence Intensity Measurements	82
4.4.4.3	Residue Fluorescence Lifetime Measurements	85
4.5	Conclusions.....	87
CHAPTER 5	CONCLUSIONS AND RECOMMENDATIONS	92
5.1	Conclusions.....	92
5.1.1	Radioactive Material-Induced Fluorescence Experiments	92
5.1.2	Laser-Induced Fluorescence Experiments	95
5.2	Recommendations.....	97
5.2.1	Radioactive Material-Induced Fluorescence Experiments	97
5.2.2	Laser-Induced Fluorescence Experiments	97
BIBLIOGRAPHY	100
VITA	104

LIST OF FIGURES

Figure 2-1.	Partial energy-level diagram for a photoluminescent system.....	7
Figure 2-2.	Nomenclature for electron spin pairing in molecular electronic states.....	7
Figure 2-3.	Typical setup of scintillation detection system.....	11
Figure 2-4.	Configuration of laser-induced fluorescence system.....	12
Figure 3-1.	Solar radiation.....	15
Figure 3-2.	BaF ₂ scintillation spectrum.....	16
Figure 3-3.	⁹⁹ Tc metal electrode encased in PTFE sleeve.....	19
Figure 3-4.	UV-Nikkor lens and Nikon UV-transmittive filter.....	19
Figure 3-5.	Film preparation setup.....	21
Figure 3-6.	PIXIS 512BUV CCD Camera and UV-Nikkor 105-mm f/4.5 lens.....	24
Figure 3-7.	Scintillator-loaded sample film mounted between two washers in front wheel of filter mount.....	25
Figure 3-8.	Rear wheel of the indexed filter mount with ⁹⁹ Tc electrode mounted in silicon stopper.....	25
Figure 3-9.	Absorbance of BaF ₂ optical disks of various thicknesses.....	27
Figure 3-10.	SEM image of BaF ₂ particles at 7000x magnification.....	28
Figure 3-11.	SEM image of BaF ₂ particles at 11,000x magnification.....	28
Figure 3-12.	Dry film thickness as a function of BaF ₂ mass loading in films drawn wet at 508, 889, and 1270 μm.....	29
Figure 3-13.	BaF ₂ -loaded EVA film transmittance at 310 nm as a function of loading for increasing drawn film thicknesses.....	30
Figure 3-14.	BaF ₂ -loaded EVA film transmittance at 310 nm as a function of drawn film thicknesses for increasing loading.....	31
Figure 3-15.	Intensity image of ⁹⁹ Tc electrode behind stainless steel washers.....	32
Figure 3-16.	3-D intensity image of ⁹⁹ Tc electrode behind stainless steel washers.....	33
Figure 3-17.	Transmission spectra for Nikon UV Transmission Filter.....	33
Figure 3-18.	Quantum efficiency spectra for PIXIS CCD cameras.....	34
Figure 3-19.	Film density thickness and β ⁻ range as a function of BaF ₂ mass loading in films drawn wet at 508, 889, and 1270 μm.....	38
Figure 3-20.	Intensity plot for 80% BaF ₂ -loaded, 1270 μm (wet) EVA film in holder exposed to 1.445 mCi ⁹⁹ Tc electrode for 45 min.....	40
Figure 3-21.	Image of 80% BaF ₂ -loaded, 1270 μm (wet) EVA film exposed to 1.445 mCi ⁹⁹ Tc electrode for 45 min.....	41
Figure 3-22.	Image of 80% BaF ₂ -loaded, 508 μm (wet) EVA film exposed to 1.445 mCi ⁹⁹ Tc electrode for 45 min.....	41
Figure 3-23.	Intensity plot for 80% BaF ₂ -loaded, 508 μm (wet) EVA film in holder exposed to 1.445 mCi ⁹⁹ Tc electrode for 45 min.....	41
Figure 3-24.	Net mean scintillation intensity for films of varying thickness as a function of BaF ₂ mass loading.....	42

Figure 3-25.	Net mean scintillation intensity for films of varying BaF ₂ mass loading as a function of drawn (wet) thickness.	43
Figure 4-1.	Example of uranyl fluorescence dependence on pH.....	47
Figure 4-2.	Dynamic quenching.	49
Figure 4-3.	Static quenching.....	49
Figure 4-4.	Primary uranyl species (≥ 0.1 mM) as a function of pH.....	51
Figure 4-5.	POSS [®] SO1444 (From www.hybridplastics.com)	53
Figure 4-6.	POSS [®] SO1460 (From www.hybridplastics.com)	53
Figure 4-7.	Fluorescence of ovalene reference standard.	56
Figure 4-8.	Variation in sample chamber configuration for solution versus solid/residue samples.	57
Figure 4-9.	Configuration of laser-induced fluorescence system.....	57
Figure 4-10.	Example of fluorescence collected in pulser 'repetitive' mode (10 accumulations summed for each of 50 spectra measured).....	58
Figure 4-11.	Effect of varying spectrograph entrance slit width on fluorescence intensity of 42.7 mM UO ₂ (ClO ₄) ₂ solution.....	59
Figure 4-12.	Example of fluorescence collected in pulser 'sequential' mode (10 accumulations summed for each of 50 spectra measured).....	60
Figure 4-13.	Example of monoexponential fit of summed fluorescence intensity for increasing pulser delay times.	61
Figure 4-14.	Millipore 1225 vacuum filtration manifold (From www.millipore.com)..	67
Figure 4-15.	Example of solid or residue sample on inorganic filter, mounted on microscope slide, and secured with coverslip.....	67
Figure 4-16.	UV-Vis absorbance of aqueous 4.8 mM UO ₂ (ClO ₄) ₂	69
Figure 4-17.	Laser-induced fluorescence of aqueous 4.8 mM UO ₂ (ClO ₄) ₂	69
Figure 4-18.	Monoexponential fit of summed fluorescence intensity for aqueous 4.8 mM UO ₂ (ClO ₄) ₂ solution as a function of increasing pulser delay times.....	70
Figure 4-19.	Fluorescence intensities of solution (4.8 mM UO ₂ ²⁺) and solid (0.048 μ mol UO ₂ ²⁺) samples.	71
Figure 4-20.	Fluorescence intensity ratios for constant uranyl perchlorate solids (0.048 μ mol UO ₂ ²⁺) with increasing Fe ³⁺	73
Figure 4-21.	Residue fluorescence intensity of 0.048 μ mol UO ₂ ²⁺ contacted with EtOH-based solutions. Measurement temperature (°C) listed in legend.....	77
Figure 4-22.	AMP-based residue fluorescence intensity with POSS [®] SO1444 and POSS [®] SO1460Na in the absence of iron.....	78
Figure 4-23.	Comparison of fluorescence intensities of AMP-based residues with POSS [®] SO1444 and POSS [®] SO1460Na to solid 0.048 μ mol UO ₂ ²⁺ . Measurement temperature (°C) listed in legend.....	79
Figure 4-24.	Residue fluorescence intensity of 0.048 μ mol UO ₂ ²⁺ and 0.425 μ mol Fe ³⁺ contacted with EtOH-based solutions. Measurement temperature (°C) listed in legend.....	84
Figure 4-25.	AMP-based residue fluorescence intensity with POSS [®] SO1444 and POSS [®] SO1460Na in the presence of iron..	85

LIST OF TABLES

Table 3-1.	Solvents for polymer dissolution.	17
Table 3-2.	Polymer names, specifications, and acronyms.	18
Table 3-3.	Composition of BaF ₂ -loading polymer solutions and the resulting BaF ₂ mass loadings.	23
Table 3-4.	Evaluated polymer and solvent combinations.	26
Table 3-5.	Calculated linear range in various absorbers of beta particles from ⁹⁹ Tc electrode. Density values from Shleien et al., 1998.	36
Table 3-6.	Calculated average energy of Bremsstrahlung radiation from ⁹⁹ Tc β ⁻ interactions with external absorbers. Z _{eff} values from Naydenov (2003).	37
Table 3-7.	Film effective density and density thickness as a function of BaF ₂ loading and ⁹⁹ Tc β ⁻ ranges in those films.	38
Table 4-1.	Reported uranyl fluorescence peaks in solution for pH 1 to 10.	48
Table 4-2.	Chemicals used for stock solution and sample preparation.	52
Table 4-3.	Composition of aqueous solution samples.	64
Table 4-4.	Composition of EtOH-based solution samples.	65
Table 4-5.	Composition of solid samples.	66
Table 4-6.	Summary of summed net fluorescence intensities for constant uranyl solution (4.8 mM UO ₂ ²⁺) and solid (0.048 μmol UO ₂ ²⁺) samples with increasing Fe ³⁺	72
Table 4-7.	Lifetimes and quenching effects for aqueous solution samples compared to their solid samples.	73
Table 4-8.	EtOH-based solution or filtrate pH at room temperature. Filtrates contacted 30-min with solid 0.048 μmol UO ₂ ²⁺ samples.	74
Table 4-9.	Summed net fluorescence intensities (<i>I</i>) for residues and filtrates of EtOH-based solutions contacted with solid 0.048 μmol UO ₂ ²⁺ samples.	75
Table 4-10.	Residue fluorescence lifetimes (μs) in the absence of iron at room temperature. Monoexponential fits with σ >> mean near zero are reported as zero.	80
Table 4-11.	EtOH-based solution or filtrate pH at room temperature. Filtrates contacted 30 minutes with solid 0.048 μmol UO ₂ ²⁺ and 0.425 μmol Fe ³⁺ samples.	82
Table 4-12.	Summed net fluorescence intensities (<i>I</i>) for residues and filtrates of EtOH-based solutions contacted with solid 0.048 μmol UO ₂ ²⁺ and 0.425 μmol Fe ³⁺ samples.	83
Table 4-13.	Residue fluorescence lifetimes (μs) in the presence of iron at room temperature. Monoexponential fits with σ >> mean near zero are reported as zero.	86
Table 4-14.	Comparison of residue fluorescence intensities and lifetimes in the presence and absence of Fe ³⁺	88

ACKNOWLEDGEMENTS

Assuming the role of a student, husband, father, mentor, friend, or officer presents its challenges. Doing all at once is only possible with the support of others. This three year journey has been a marathon. Thank you to those that have taken it with me.

My committee has made the process of completing exams and this dissertation possible by being encouraging, responsive, and most importantly, constructive. My sincere appreciation goes to Ken Czerwinski, Ralf Sudowe, Ken Moody, and Cynthia Gong for their efforts and mentorship. The success and bright future of this Ph.D. program in radiochemistry is due to the guidance and initiative provide by its faculty.

My fellow suffering graduate students make leaving difficult. Nick Smith and Rich Gostic, in particular, have my deepest gratitude for providing nearly daily counsel on all things chemistry and of little importance. Julie Gostic, Kiel Holliday, Amber Wright, Chinthaka Silva, Troy Robinson, Narek Gharibyan, and Chris Klug kept me sane, entertained, and feeling like I was still their age. The funding and support of DARPA, INL, STL, Gary Cerefice, Tom O'Dou, Trevor Low, Frederic Poineau, Leisa Rodriguez, Avrina Smith, Ruby Bynum, and Kris Davidson was critical to my success... thanks!

My amazing friend and bride, Beverly, has carried so much of the family load this last year that I will hardly be able to make that up to her. Her greatest gifts of love, encouragement, our one year old Evan, and our son-to-be, Mitchell (to be born as this goes to print) keep me going. All my respect,

Craig

CHAPTER 1

INTRODUCTION

1.1 Problem

The United States maintains and seeks to improve national capabilities to detect radioactive materials remaining on surfaces from various individual, industrial or military activities, regardless of whether their purpose is viewed as legitimate or illicit. Current detection methods are limited in the types of materials, distances, and environments in which they can operate effectively. Enhanced detection of surface radioactive materials has wide application for functional communities such as crisis response, consequence management, environmental management, remediation, intelligence, and non-proliferation within industry, government, or the military.

Of primary concern to the Department of Defense (DoD), Department of Energy (DOE), and National Nuclear Security Administration (NNSA) are activities involving source, fertile, and fissile radionuclides such as ^{232}Th , ^{233}U , ^{235}U , ^{238}U , ^{239}Pu , ^{240}Pu , and ^{241}Pu ; products of their thermal fission including ^{85}Kr , ^{90}Sr , $^{95}\text{Zr-Nb}$, ^{99}Tc , ^{129}I , ^{131}I , ^{133}Xe , ^{137}Cs , and $^{140}\text{Ba-La}$; and other common radionuclides including ^{60}Co , ^{192}Ir , ^{210}Po , and ^{241}Am .

The genesis of this research was a stated need by the Defense Advanced Research Projects Agency (DARPA) and the NNSA Special Technologies Laboratory (STL) to

develop strippable films which could be applied to surfaces and then passively or actively interrogated to determine the presence or absence of residual radioactive materials. The future goal of both organizations is to enhance the detection of radioactive materials in the presence of interfering environmental conditions on surfaces contaminated by accidental or intentional releases. DARPA provided funds to incorporate scintillators, materials that emit ultraviolet (UV) photons following exposure to radioactive materials, into strippable films and assess their use in detecting radioactive materials which decay by charged particle emission. STL supported experiments to characterize the effects of alcohol-soluble ligands and the presence of iron on the fluorescence produced by uranyl solids when excited with a pulsed laser.

Candidate radionuclides for use in this research, and their primary radiation decays, included ^{238}U (4.20 MeV α and 49.6 keV γ) due to its high natural abundance and ^{90}Sr (546 keV β_{max}), ^{99}Tc (294 keV β_{max}), and ^{137}Cs (514 keV β_{max} and 661.7 keV γ) due to their large ^{235}U thermal-neutron fission yields. Current detection techniques allow rapid and standoff detection of ^{137}Cs because its photon is not significantly attenuated in the distance between the source and the detector. However, as the particle energy decreases, or the charge on the particle increases, it is subject to greater interactions with surrounding media, including air, and as a result the range at which it can be detected is reduced. Determination of the presence of α , low-energy β , or low-energy γ emitters, such as ^{238}U and ^{99}Tc , must be done at ranges less than a meter to afford adequate signal-to-noise detection. Fortunately, detection distances and limits can be improved by detecting the light, called fluorescence, emitted from the surface following its treatment and excitation from an external source. Surfaces may be treated either by applying a

scintillator that is excited by the decaying radioactive material (§1.2.1) or by applying a solution that binds to the radioactive material and enhances its intrinsic fluorescence when exposed to a light source (§1.2.2).

1.2 Research Goals and Objectives

1.2.1 Radioactive Material-Induced Fluorescence Experiments

The goals of these experiments were to: (1) select a scintillator that emits light in a UV wavelength region with low solar background, (2) choose a UV-transparent polymer solution that forms a strippable film when applied to a surface and dried, (3) determine the effect of varying a film's scintillator loading on its scintillation intensity for a fixed radioactive material source and detection geometry, and (4) determine the effect of varying the film's thickness for the same conditions.

Scintillators are excited to higher electronic states by the absorption of kinetic energy and subsequently deexcite by emission of light at characteristic wavelengths, a process termed prompt fluorescence or scintillation. For example, barium fluoride (BaF_2) scintillates by emission of UV photons at 195, 220, and 310 nm. Additional detail on the theory and measurement of fluorescence is provided in Chapter 2.

The experiments presented in Chapter 3 use ^{99}Tc to induce these scintillations from BaF_2 incorporated into strippable polymer films. Loading the scintillator into a polymer solution offers not only a means of application, but provides the additional benefits of fixing the radioactivity in place to prevent its further migration, inhalation, or ingestion. A film that is also strippable serves as a method for forensic sample collection or spot remediation. The use of a UV scintillator like BaF_2 enables photon detection and

measurement in full sunlight because nearly all solar UV radiation with wavelengths less than 315 nm is absorbed by atmospheric ozone. This very low background creates a 'solar-blind' region in which scintillation can be detected at much lower intensities. Current surface decontamination coatings are not UV-transparent and therefore scintillations that do occur are absorbed in the coating rather than transmitted to the detector.

1.2.2 Laser-Induced Fluorescence Experiments

The goals of these experiments were to: (1) select an iron(III) concentration sufficient to observably quench the fluorescence of uranyl solids; (2) determine the acid concentration required to maintain buffered-ethanol solutions at their first pKa following the addition of POSS[®] ligands, (3) characterize the effect of contacting those solutions with uranyl solids, in the absence and presence of iron(III), on the uranyl fluorescence intensity and lifetime; and (4) determine if the addition of POSS[®] ligands to the solutions enhances the uranyl solid fluorescence intensity or lifetime in the absence and presence of iron(III).

Uranium in the hexavalent (U^{6+}) oxidation state can fluoresce. However, uranium samples may often be found in the reduced, non-fluorescing tetravalent state (U^{4+}), with UO_2 as an example. In addition, the presence of some surface materials may prevent fluorescence or reduce its intensity by a process termed quenching. The free uranyl ion, $U(VI)O_2^{2+}$, dominates aqueous uranium solution chemistry and fluoresces with characteristic spectral and temporal properties that can be used in its detection. However, uranyl fluorescence is quenched by halide ions (e.g. I^- , Br^- , Cl^- , and F^-), low oxidation state metal ions (e.g. Ag^+ , Fe^{2+} , Fe^{3+} , and Mn^{2+}), and organic molecules (alcohols and

aromatic hydrocarbons) (Burrows et al., 1985; Matsushima et al., 1974; Morss et al., 2006; Moriyasu et al., 1977; Sakuraba and Matsushima, 1971; Wheeler and Thomas, 1984). This quenching may be overcome if a ligand complexes and shields the uranyl such that the fluorescence becomes again competitive as a deexcitation process. The ligands used in this research were polyhedral oligomeric silsesquioxanes (POSS[®]), where each silicon atom is formally bonded to one and a half oxygen atoms and one hydrocarbon in a hybrid inorganic-organic cage-structured composite. The functional groups on the POSS[®] can be customized to tailor properties, such as solubility. The primary ligand studied contained ethyl groups and therefore ethanol was used as its solvent. Although ethanol is a known quencher, uranyl fluorescence was measured primarily on solid samples where the solvent is presumed to have fully evaporated. Detection of uranium contamination on metal surfaces is often complicated by the presence of rust or hydrated iron(III) oxide. The effects of Fe³⁺ and any residual ethanol on the uranyl fluorescence were characterized by measuring its intensity and its time-dependent decay (lifetime) before and after contact with POSS[®] ligands. Additional information on uranyl fluorescence, including quenching and measurement, is provided in the background of Chapter 4 (§4.2).

The following chapter introduces principles of the analytical and characterization techniques used to meet the stated experimental goals of this work. A reader familiar with instrumental analysis may choose to continue with Chapter 3, Radioactive-Material Induced Fluorescence Experiments.

CHAPTER 2

ANALYTICAL AND CHARACTERIZATION TECHNIQUES

2.1 Introduction to Absorption and Fluorescence Spectrometry

Spectrometry is the measurement of radiation intensity using electronic devices, especially photoelectric transducers. Spectroscopy refers to the broader category of atomic and molecular science dealing with the interactions of matter and energy such as electromagnetic radiation, acoustic waves, ion beams, and electron beams. This chapter briefly discusses the principles and procedures associated with the spectrometry of ultraviolet (UV) and visible radiations for the purpose of characterizing standards and samples. Analytical and characterization techniques used in this research include UV-visible (UV-vis) absorption spectrometry (§2.2), atomic emission spectroscopy (§2.3), scintillation counting (§2.4), and visible fluorescence spectrometry (§2.5).

Absorption spectrometry is used in the identification and characterization of elements and compounds within a sample based on the absorption of photons from an excitation source. Photon absorption excites one or more paired electrons to singlet or triplet states of higher energy which are often followed by measurable and characteristic emissions (Figure 2-1). In the context of this research, the energy that results in excitation is provided by external sources rather than by chemical reactions. These excitation sources include the decay of radioactive materials as well as UV-visible lamps or lasers used in spectrometric instrumentation.

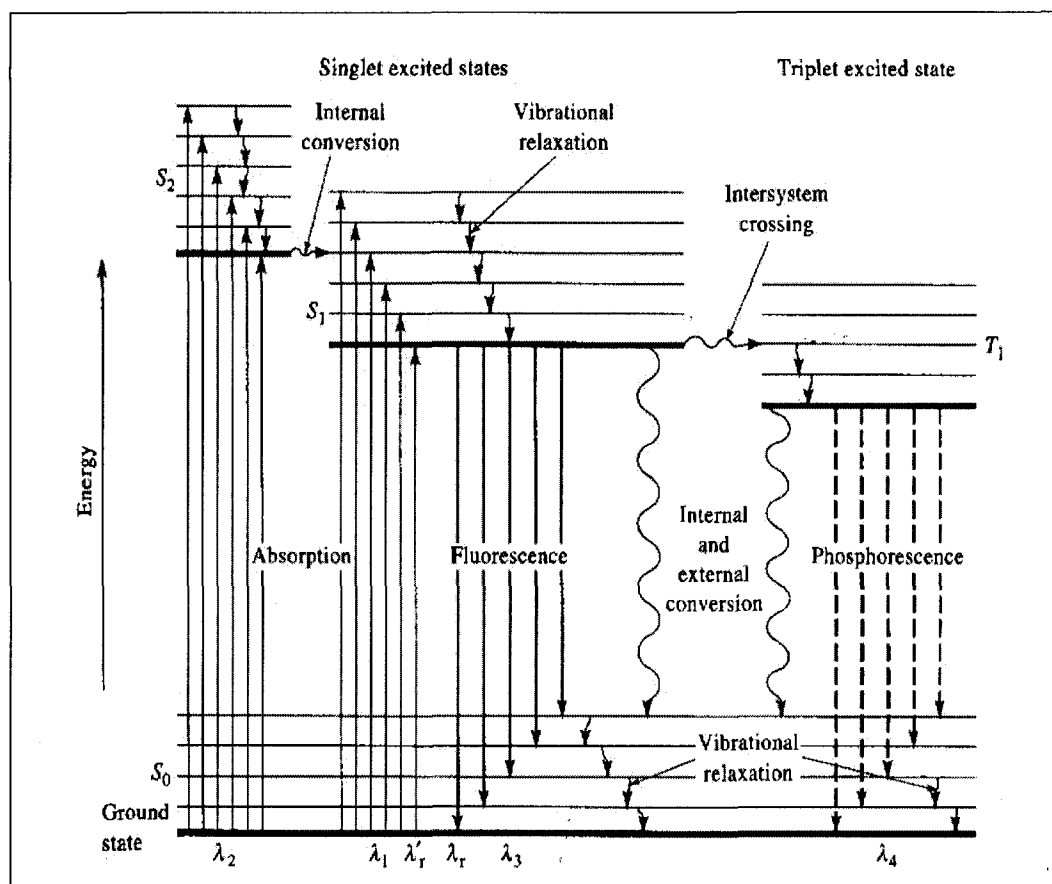


Figure 2-1. Partial energy-level diagram for a photoluminescent system. Adapted from Skoog et al., 2007.

Electrons in single states are spin paired (antiparallel spins) while those in triplet states have become unpaired and have parallel spins vectors (Figure 2-2). Since transitions between singlet and triplet states involve changes in spin angular momentum, or multiplicity, they are forbidden and therefore significantly less probable than allowed singlet-to-singlet transitions. Scintillation counting and fluorescence spectrometry, as described

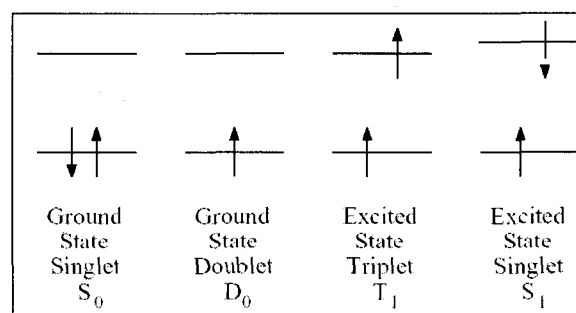


Figure 2-2. Nomenclature for electron spin pairing in molecular electronic states. Adapted from Skoog et al., 2007

herein, measure the de-excitation transitions from the singlet excited states to the singlet ground state via fluorescence. The average time for an electron to transition from an excited state to ground state is defined as the lifetime of the excited state and is inversely proportional to the probability of the transition. Accordingly, allowed singlet excited-to-singlet ground transitions occur rapidly via fluorescence with lifetimes ranging from 10^{-10} to 10^{-5} seconds and forbidden triplet excited-to-singlet ground transitions occur slowly via phosphorescence with lifetimes from 10^{-4} to 10 s or more (Skoog et al., 2007).

2.2 Principles of Ultraviolet-Visible Absorption Spectrometry

Within the ultraviolet-visible region between 180 and 700 nm, the absorbance of a sample is linearly related to the concentration of the absorbing species in the sample.

This is described by Beer's law:

$$A = -\log T = \log \frac{P_o}{P} = \epsilon bc$$

Where $A \equiv$ absorbance

$T \equiv$ transmittance $= P/P_o$

$P_o \equiv$ incident radiant power or intensity (I_o)

$P \equiv$ transmitted radiant power or intensity (I)

$\epsilon \equiv$ molar absorptivity

$b \equiv$ sample path length

$c \equiv$ absorbing species concentration

Using published values of applicable molar absorptivities and samples of fixed path length, one can use Beer's Law to determine an unknown concentration of a given species. Conversely, if a sample series of known concentrations are used to develop a calibration curve of A versus c at a given wavelength, the slope can be used to determine an unknown value of ϵ .

Despite deviations from Beer's Law at very high concentrations, UV-vis absorption spectrometry is useful for the identification and characterization of many absorbing species. All organic compounds have valence electrons that can be excited by radiation absorption, although the resulting spectral bands are usually broad due to the superposition of many overlapping transitions. Analysis can still reveal information about the functional groups in the compound. Many inorganic anions, including nitrate, absorb at UV wavelengths due to the excitation of non-binding electrons. Cations and complexes of transition metals which are active in the UV-vis region have broad absorption bands in at least one oxidation state and are therefore colored. These absorption bands are highly affected by the bonding of ligands to the outer electrons of the metal ion and are therefore sensitive to speciation. In contrast, lanthanides and actinides exhibit narrower bands because light absorption occurs in the $4f$ and $5f$ electrons shells, which are shielded from the effect of ligand bonding (Skoog et al., 2007).

2.3 Principles of Scintillation Counting

Scintillation is the process by which scintillators convert the kinetic energy of charged particles into detectable light through prompt fluorescence. By definition, the excitation of the scintillator is caused by absorption of incident ionizing radiation such as gamma, alpha, or beta radiation from the decay of radioactive materials. The number of scintillation photons produced per unit energy absorbed is the light yield and for most inorganic scintillators is proportional, although not always linearly, to the energy absorbed. Light yield is commonly linear for the following energies: gamma

(γ) radiation >400 keV, protons and deuterons >1 MeV, and alpha particles >15 MeV (Tsoulfanidis, 1995).

The choice of scintillators is usually based on properties such as emission wavelength, decay time, and light yield. Thallium-activated sodium iodide, or NaI(Tl), is the standard scintillator for photon counting due its excellent light yield of 38 photons per keV γ deposited. However, it is hygroscopic, has a long decay time that may not be feasible for high count rate applications, scintillates in the visible region, and its response is not proportional to deposited electron energy (Knoll, 2000). Information regarding the ultraviolet scintillations of the inorganic scintillator barium fluoride (BaF_2) is provided in the background of Chapter 3.

A typical set-up for scintillation counting consists of a scintillator crystal, a photon transducer such as a photomultiplier tube (PMT), an amplifier, and a pulse-height analyzer. Scintillations produced by ionization events in the crystal are transmitted to the photocathode of the PMT where they are converted to electrical pulses. These weak pulses are amplified and processed using single-channel or multichannel analyzers as required (Figure 2-3).

For research presented in Chapter 3, the scintillator crystal is replaced by a scintillator-loaded scintillating thin film and the electronics are replaced by an UV-sensitive charge-coupled device (CCD) camera and lens. Semiconductor photon transducers, such as CCDs, are prevalent within spectrometric instrumentation and allow a decoupling of the scintillator from the detector array so remote detection is possible.

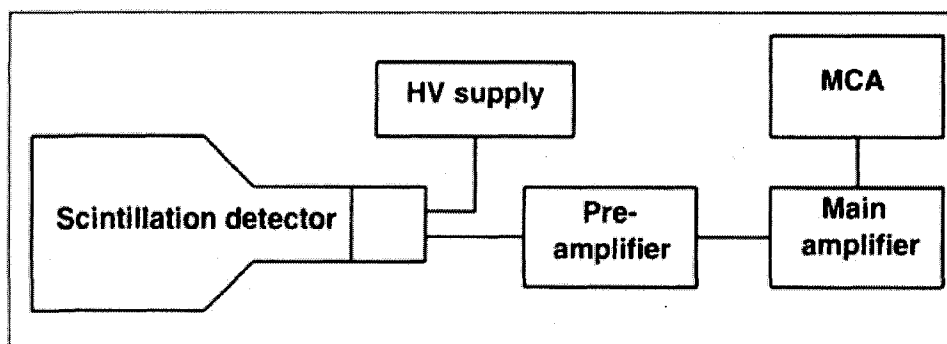


Figure 2-3. Typical setup of scintillation detection system.

2.4 Principles of Atomic Emission Spectrometry

Atomic Emission Spectrometry is the measurement of characteristic line spectra emitted following de-excitation of atomized samples. Samples are commonly injected as an aerosol into an argon plasma torch where they are atomized to gaseous atoms or elementary ions. A portion of these are elevated to higher electronic states and emit UV or visible photons that can be detected on spectrographs, such as a CCD transducer described above.

The high temperatures and nearly complete atomization produced by inductively coupled plasma (ICP) torches permit the qualitative and quantitative determination of elements at very low concentrations with correspondingly low chemical interference. Determination of all metallic elements is possible using AES, although its use is not practical for the alkalis. Their most prominent lines appear at NIR wavelengths where most spectrometers are quite inefficient because they are designed to also detect in the UV region (Skoog et al., 2007). For this research, ICP-AES techniques were used to characterize iron in prepared stock solutions.

2.5 Principles of Visible Fluorescence Spectrometry

Fluorescence materials, such as uranyl, permit rapid and high signal-to-noise detection of their characteristic emission spectra as well as the time-dependent decay of that fluorescence. Fluorescence intensity and lifetimes are measured by exciting the sample and recording its emissions at 90° in order to minimize scattering and source contributions (Figure 2-4). In some newer systems and in this research, excitation is provided by a fixed wavelength pulsed laser and fluorescence is measured using cooled CCD transducers. A portion of the laser is reflected to a power meter using an inline beamsplitter to monitor the energy of each pulse.

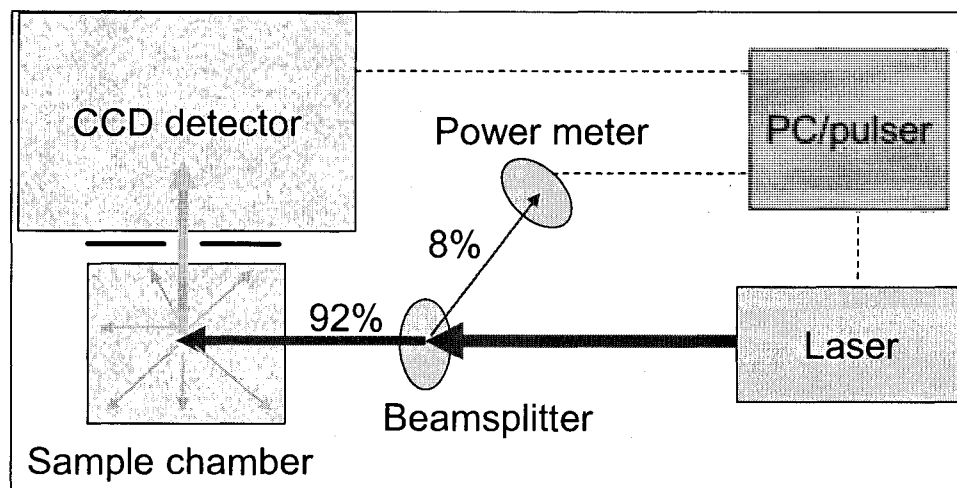


Figure 2-4. Configuration of laser-induced fluorescence system. Measurement parameters for fluorescence intensities versus lifetimes are controlled using the personal computer (PC) and pulser. The sample chamber is configurable for either solution or solid samples.

Fluorescence intensities are corrected for laser pulse fluctuations using the pulse energies recorded on the power meter. By using a pulsed laser and gating the detection of the fluorescence, one can record the intensity decay as a function of time after

excitation of the sample. The sample is excited by laser for a duration called the gate width (exposure time) and after a short increment called the delay time, the fluorescence intensity is measured for that pulse. The delay time is increased for each subsequent pulse to collect the intensity for a different portion of the exponential fluorescence decay. A logarithmic plot of the intensity as a function of the delay time results in determination of the lifetime from the slope of the decay curve (see §4.3.1.8).

The analytical and characterization techniques described above were used in the experiments detailed in the following chapters. Chapter 3 presents radioactive material-induced fluorescence experiments in which UV-vis was used to verify materials were transparent to the wavelengths of BaF₂ scintillations and scintillation counting was used to quantify those scintillations. Chapter 4 presents laser-induced fluorescence experiments in which the concentrations of uranyl and iron(III) in a prepared stock solutions were determined by UV-vis and ICP-AES, respectively. The effects of iron(III) and ligand solutions on the intensity and lifetime of uranyl fluorescence was investigated using visible fluorescence spectrometry.

CHAPTER 3

RADIOACTIVE MATERIAL-INDUCED FLUORESCENCE EXPERIMENTS

3.1 Introduction

These experiments develop and characterize polymer thin films loaded with barium fluoride (BaF_2) crystals as a method to detect prompt, ultraviolet (UV) fluorescence (scintillations) from a radioactively-contaminated surface. Nearly all solar UV radiation with wavelengths less than 315 nm is absorbed by atmospheric ozone, creating a ‘solar-blind’ region in which photon detection and measurement is possible in full sunlight with very low background. Current surface decontamination coatings are not UV-transparent and therefore scintillations that do occur are absorbed in the coating rather than transmitted to the detection system. The goal of these experiments was to determine if scintillations could be induced and detected using a radioactive material source (^{99}Tc), polymer films loaded with BaF_2 (scintillations at 195, 220, and 310 nm), and a UV-sensitive camera system.

The principles underlying the analytical and characterization techniques of ultraviolet-visible absorption spectrometry and scintillation counting used in these experiments were summarized in Chapter 2. Background information relevant to the discussion in this chapter regarding the solar-blind ultraviolet region and scintillator properties are provided in §3.2. The materials and methods used to conduct radioactive material-induced fluorescence measurements by scintillation counting are described in

§3.3.1. The preparation and characterization of polymer films, BaF_2 , and BaF_2 -loaded polymer films are outlined in §3.3.2, §3.3.3, §3.3.4, and §3.3.5. The experimental results for each are presented and discussed in §3.4.1, 3.4.2, and §3.4.3. Conclusions are highlighted in §3.5.

3.2 Background

The scintillator used in these experiments must emit ultraviolet photons with wavelengths below 315 nm. In this region, atmospheric ozone absorbs most solar-emitted ultraviolet photons such that the background irradiance, or intensity, of ground-level UV < 315 nm is very low, resulting in a region that is 'solar-blind' (Figure 3-1). Detection in this region is enhanced due to increased signal-to-noise ratios and can be conducted during daylight.

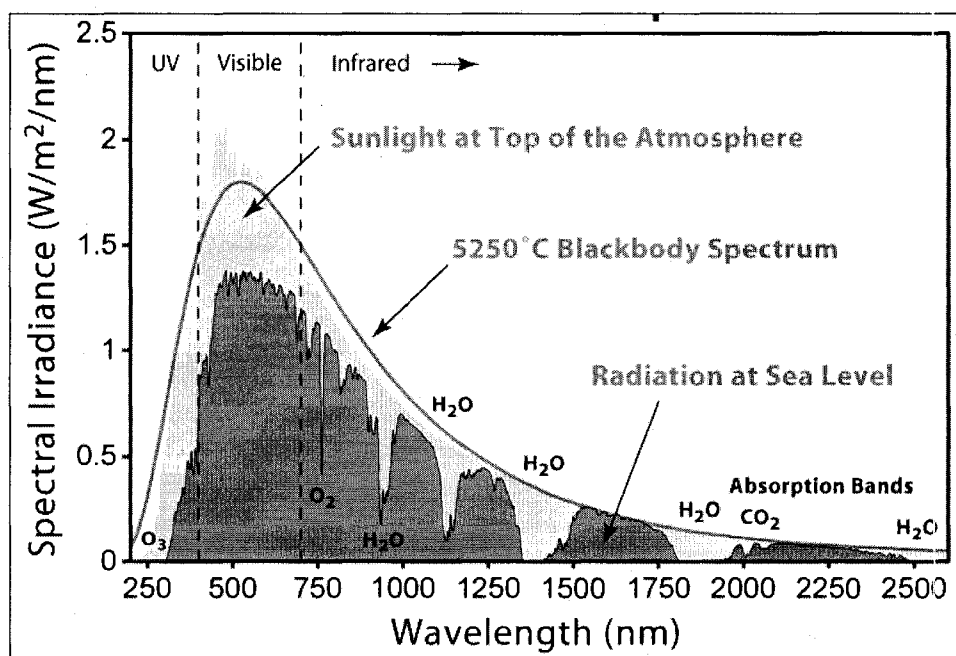


Figure 3-1. Solar radiation. Sea Level background ultraviolet is negligible in the solar-blind wavelength region < 315 nm. Reused under free license by Global Warming Art.

Common organic or inorganic scintillators that emit photons in the solar-blind region include unactivated barium fluoride (BaF_2), cerium fluoride (CeF_3), and cesium iodide (CsI), as well as lutetium aluminum garnet (LuAG) activated with scandium. CeF_3 , and CsI light yields are very low compared to NaI(Tl) and only a fraction of their scintillations are ultraviolet. LuAG(Sc) , although it has a high light yield and is non-hygroscopic (Ryskin et al., 1994), is not readily available and must custom synthesized. As a result, polymer films were individually loaded with BaF_2 and exposed to a high-activity, particulate radiation source for evaluation by scintillation counting.

BaF_2 characteristic scintillations include a slow 630 nanosecond (ns) decay, centered at 310 nm, and two very fast 0.6 ns decays, centered at 195 and 220 nm. The light yields for BaF_2 are weak compared to NaI(Tl) at only 9.5 photons per keV γ for the slow scintillation and 1.4 photons per keV γ for the fast scintillations. At room temperature,

about 80% of the total scintillation yield is measured in the slow component, but this fraction decreases rapidly with increasing temperature; the fast component scintillation is temperature independent (Figure 3-2).

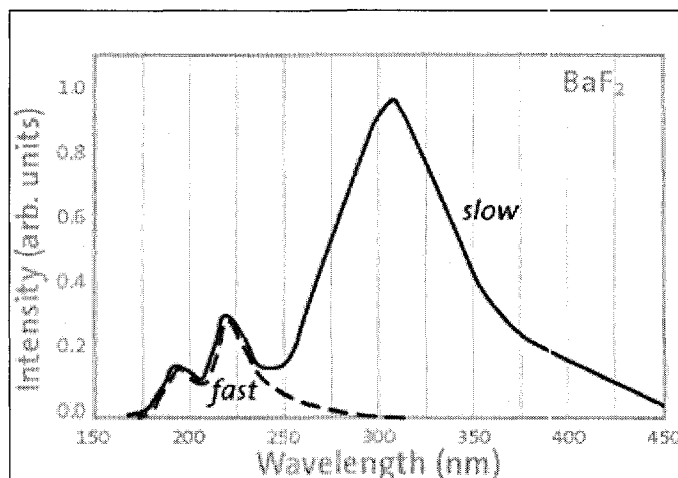


Figure 3-2. BaF_2 scintillation spectrum. From www.photonic.saint-gobain.com.

3.3 Experimental

3.3.1 Materials and Instrumentation

3.3.1.1 Chemicals

The solvents in Table 3-1 were purchased from Sigma-Aldrich or VWR and used as received.

Table 3-1. Solvents for polymer dissolution.

Solvent	Purity	Manufacturer
Acetic acid (glacial)	99.8%	Sigma-Aldrich
Acetonitrile	UV grade	Burdick & Jackson
1-Butanol	99.8%, anhydrous	Sigma-Aldrich
Carbon tetrachloride (CCl ₄)	≥99.5%, anhydrous	Sigma-Aldrich
Chloroform	≥99%, anhydrous	Sigma-Aldrich
Cyclohexane	99.5%, anhydrous	Sigma-Aldrich
Cyclohexanone	99.8%	Sigma-Aldrich
Cyclopentane	≥75%, anhydrous	Sigma-Aldrich
Decahydronaphthalene (Decalin [®])	≥99%, mixture of cis + trans, anhydrous	Sigma-Aldrich
Dichloromethane	99.8%, anhydrous	Sigma-Aldrich
Diethyl ether	>99%, anhydrous	Sigma-Aldrich
N,N-Dimethylacetamide (DMA)	99%	Sigma-Aldrich
N,N-Dimethylformamide (DMF)	99%	Sigma-Aldrich
Dimethyl sulfoxide (DMSO)	≥99.6%	Sigma-Aldrich
Ethanol (EtOH)	≥99.5%, anhydrous	Sigma-Aldrich
Ethyl acetate	HPLC grade	Burdick & Jackson
Ethylene glycol butyl ether	≥99.5%	Sigma-Aldrich
Heptane	99%, anhydrous	Sigma-Aldrich
Hexane	95%, anhydrous	Sigma-Aldrich
Methyl ethyl ketone	>99%	Sigma-Aldrich
4-hydroxy-4-methyl-2-pentanone (diacetone alcohol)	99%	Sigma-Aldrich
Methyl-2-pyrrolidone (NMP)	99%	Sigma-Aldrich
2-Propanol	99.5%, anhydrous	Sigma-Aldrich
Tetrahydrofuran (THF)	99.9%, anhydrous, inhibitor free	Sigma-Aldrich
Toluene	99.8%, anhydrous	Sigma-Aldrich
p-Xylene	>99%, anhydrous	Sigma-Aldrich

All polymers were purchased from Sigma-Aldrich or VWR. Their form, specifications, and acronym used in the remainder of this paper are listed in Table 3-2.

Table 3-2. Polymer names, specifications, and acronyms.

Polymer	Average M_w	Acronyms	Manufacturer
Poly(ethylene- <i>co</i> -vinyl acetate) beads	25 wt% vinyl acetate	EVA(a)	Sigma-Aldrich
Poly(ethylene- <i>co</i> -vinyl acetate) beads	40 wt% vinyl acetate	EVA(b)	Sigma-Aldrich
Poly(vinyl) butyral powder	70,000 – 100,000	PVB(a)	Sigma-Aldrich
Poly(vinyl) butyral powder	90,000 - 120,000	PVB(b)	Sigma-Aldrich
Poly(vinyl) butyral powder	170,000 – 250,000	PVB(c)	Sigma-Aldrich
Polyethylene powder	4,000	PE(a)	Sigma-Aldrich
Polyethylene powder	35,000	PE(b)	Sigma-Aldrich
Polyisobutylene slab	500,000	PIB(a)	Sigma-Aldrich
Polyisobutylene slab	1,000,000	PIB(b)	Sigma-Aldrich
Polyisobutylene slab	4,200,000	PIB(c)	Sigma-Aldrich
Polypropylene powder	12,000, isotactic	PP(a)	Sigma-Aldrich
Polypropylene powder	190,000, isotactic	PP(b)	Sigma-Aldrich
Polypropylene powder	250,000, isotactic	PP(c)	Sigma-Aldrich
Polypropylene powder	580,000, isotactic	PP(d)	Sigma-Aldrich
Polyvinyl acetate beads	100,000	PVAc	Sigma-Aldrich
Polyvinyl alcohol powder	77,000-79,000	PVA	J.T. Baker
Polyvinylidene fluoride powder	534,000	PVDF	Sigma-Aldrich

3.3.1.2 Scintillator

The scintillators evaluated in the experiments were barium fluoride (BaF_2 , 98%, average particle size $\leq 5 \mu m$) from Sigma-Aldrich and BaF_2 optical disks (25-mm diameter; 3, 3.5 and 6 mm thicknesses) from Del Mar Photonics.

3.3.1.3 Radioactive Material Source

The radioactive source was a ^{99}Tc ($E_{\beta^- \max} = 294 \text{ keV}$) electrode prepared at the University of Nevada, Las Vegas (UNLV) by soldering 85 mg ^{99}Tc metal onto the end of

a copper wire and encasing it in a polytetrafluoroethylene (PTFE) sleeve (Figure 3-3).

The source activity was calculated as 1.445 mCi as of 4/30/2007.

3.3.1.4 Equipment

An ultrasonic homogenizer (Omni Ruptor 250, intermediate titanium tip) from Omni International was used to mix the polymer and scintillation material. Thin films were drawn on film release paper (127 μm , silicone-coated) and a leveling drawdown plate to specified thicknesses using an adjustable film applicator (Microm II, 10.2-cm path width) from Gardco. Film viscosity and thickness was measured with a rotational viscometer (Model DV-E) from Brookfield Engineering and disk micrometer (Model 256RL-1) from Starrett. Films and sources were mounted in a double-wheel indexed filter mount (Model FWM1X12) from Newport for scintillation counting.

3.3.1.5 Scintillation Counting

Instrumentation

Instrumentation for scintillation counting included a CCD camera (PIXIS

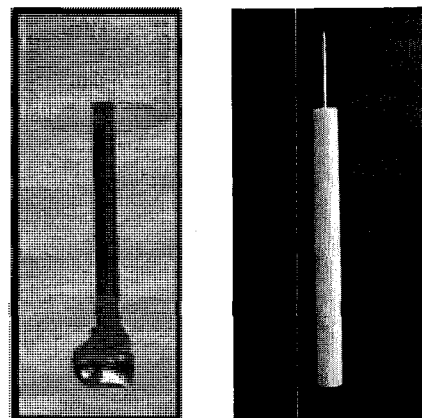


Figure 3-3. ^{99}Tc metal electrode encased in PTFE sleeve.



Figure 3-4. UV-Nikkor lens and Nikon UV-transmittive filter. Copyright by Stephen Gandy, www.CameraQuest.com. All Rights Reserved.

512BUV, Nikon bayonet 52-mm F-mount) from Princeton Instruments and a UV lens/filter (UV-Nikkor, 150-mm, f/4.5, AF-1 filter holder, UV-transmitting filter) from Nikon (Figure 3-4).

3.3.2 Polymer Film Preparation and Evaluation

3.3.2.1 Polymer Solution Preparation and Evaluation

One gram of polymer was added to 10 mL of solvent in a glass scintillation vial, mixed by vortex, and allowed to stand for 24 hours before evaluation. The polymer-solvent mixtures were visually examined for polymer dissolution, swelling, or settling and for solution color change or haziness. Solution viscosities were measured with a rotational viscometer for those polymers that dissolved completely.

Polymer solutions used for samples were prepared as stock solutions by adding weighed polymer solids to volumetrically measured solvents in glass bottles with PTFE-lined caps. The solutions were equilibrated for at least 24 hours prior to use to allow for complete polymer dissolution and swelling.

3.3.2.2 Polymer Film Preparation and Evaluation

Film release paper was clipped and taped to a leveled glass drawdown plate. A few milliliters of polymer solution were poured onto the paper and drawn into thin films using an adjustable blade film applicator (Figure 3-5). Films were dried 24-48 hours in a laboratory hood at room temperature and evaluated for surface uniformity, ease of removal, and flexibility.

Each film was visually inspected for surface uniformity to include lack of ripples, foreign matter, bubbles, or pits. Ease of removal was assessed by peeling the film from the release paper, measuring the consistency of thickness across the film, examining the

uniformity of the underside, and identifying deformations. Films that dried with smooth surfaces, released without deformation, and remained flexible were considered for further evaluation.

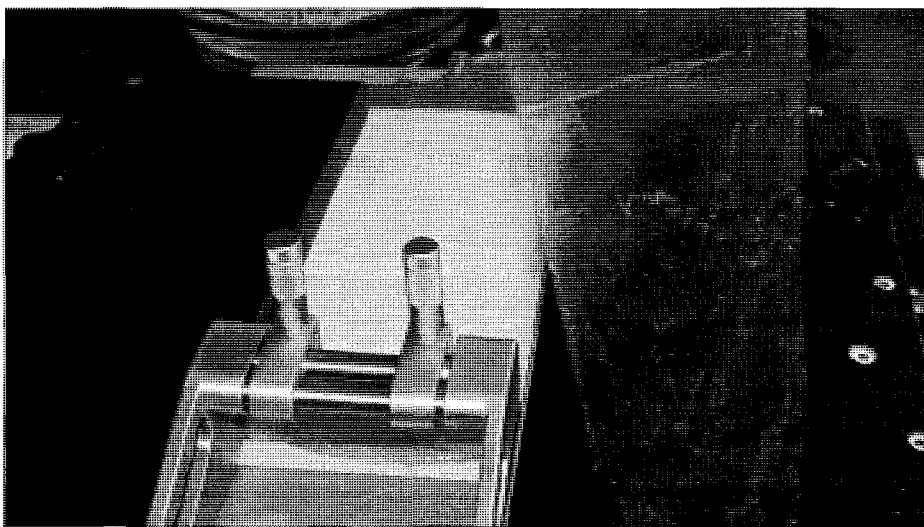


Figure 3-5. Film preparation setup. Polymer solutions drawn over release paper with adjustable blade applicator (center) between guides of jig prepared at UNLV. Sample test film displayed in foreground.

3.3.3 BaF₂ Characterization

3.3.3.1 UV-Visible Absorption Measurements

BaF₂ optical disks were taped to a solid sample stage of a Cary 6000i UV-Vis-NIR spectrometer with the disk edge 2.5 cm from the detector window. Their absorbance was measured at room temperature by UV-Vis from 185-400 nm under continuous N₂ flow (15-mm pressure). Background of an empty N₂-purged chamber was subtracted from each spectrum.

3.3.3.2 Scanning Electron Microscopy

BaF₂ powder was rinsed with acetone through a 63- μ m sieve into a glass beaker. The permeate was mixed by vortex and homogenized using ultrasound for 5 minutes at 80% power. After evaporation to dryness, prepared BaF₂ was dusted onto double-sided carbon tape on 13-mm diameter stainless-steel sample mounts. Excess BaF₂ was removed with a compressed air canister. Particle size and agglomeration within the powder were evaluated using a JEOL Model JSM-5610 scanning electron microscope (SEM) in secondary emission imaging (SEI) mode with an acceleration voltage of 15 kV.

3.3.4 BaF₂-Loaded Polymer Film Preparation

3.3.4.1 BaF₂-Loaded Polymer Solution Preparation

BaF₂-loaded polymer solutions were prepared by adding weighed BaF₂ powder to prepared polymer stock solutions in glass bottles. The stock solutions were added by mass due to their high viscosities. To enhance the quality of films prepared from the solutions, additional solvent was mixed by vortex into each solution until the viscosity measured approximately 10,000 centipoise with a rotational viscometer. The BaF₂-loaded polymer solutions were further treated by ultrasound for five minutes at 80% power. Specifically, a 17% mass/mass (m/m) stock solution of 60 g EVA(B) in 300 g CCl₄ was prepared in a glass bottle and allowed to equilibrate for 24 hours at room temperature. Increasing BaF₂ masses were added to 6 g aliquots of EVA-CCl₄ solution as listed in Table 3-3. The resulting scintillator loadings were calculated as the ratio of scintillator mass to polymer mass in the solution, since all solvent is assumed to evaporate.

Table 3-3. Composition of BaF₂-loading polymer solutions and the resulting BaF₂ mass loadings.

m _{EVA} (g) in stock solution	1.00	1.00	1.00	1.00	1.00
m _{CCl₄} (g) in stock solution	5.00	5.00	5.00	5.00	5.00
m _{BaF₂} (g) added	0.00	0.33	1.00	1.86	4.00
m _{CCl₄} (g) added	0.00	0.83	2.50	4.64	10.00
m _{solution} (g)	6.00	7.16	9.50	12.50	20.00
BaF ₂ mass loading	0%	25%	50%	65%	80%

3.3.4.2 BaF₂-Loaded Polymer Film Preparation

BaF₂ -loaded polymer solutions were drawn into films of 508, 889, or 1270 μm wet thickness on a drawdown plate using release paper and an adjustable film applicator. Films were dried for 24-48 hours in a laboratory hood at room temperature. From each BaF₂ -loaded film, 1.59-cm-diameter samples were removed with a hollow punch, labeled on the film top edge, and their dry thickness measured with a disk micrometer.

3.3.5 BaF₂-Loaded Polymer Film Characterization

3.3.5.1 UV-Visible Transmittance Measurements

Transmittance was measured in BaF₂-loaded films to verify the films were transparent to the scintillations produced at 195, 220, and 310 nm. A 2.54-cm (outer diameter) stainless-steel washer was taped to the solid sample stage with the washer's 1.27-cm diameter hole centered over the sample stage opening. The film was placed on the washer with the top facing the detector and secured with a "magnetic washer" stamped from a 0.32-cm thick magnetic sheet. Transmittance was measured using a Cary 6000i UV-Vis-NIR spectrometer from 185-350 nm under a continuous N₂ flow using 120 nm/min scan rate, double-beam mode, and baseline correction.

3.3.5.2 Scintillation Counting

The scintillation detection system consisted of an UV-sensitive camera and an UV-transmittive lens-filter combination mounted on an optical rail at an adjustable distance from a double-wheel indexed filter mount loaded with sources and samples, all housed in a dark box to minimize ambient light (Figure 3-6).

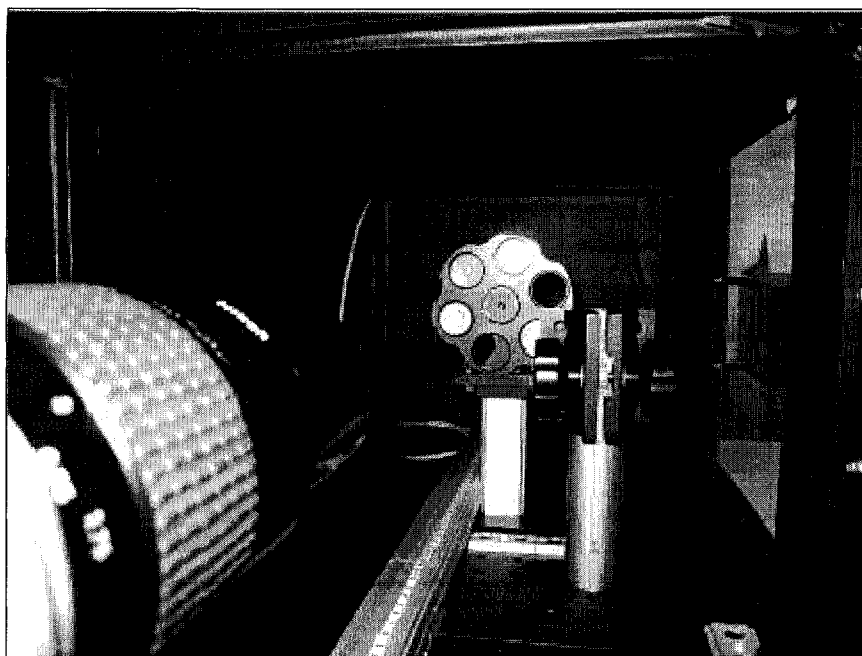


Figure 3-6. PIXIS 512BUV CCD Camera and UV-Nikkor 105-mm f/4.5 lens focused on filter wheel with films mounted 50-cm from camera's CCD in dark box.

The camera, lens, and filter wheel heights were matched using a laser level and the lens focused on the 8 o'clock position of the filter wheel using a high-resolution print in place of a sample film. The camera optical depth was calibrated to a sample film-to-CCD distance of 50-cm. Camera settings were controlled and data were processed using Winview/32 (Roper Scientific, Version 2.5.21.0). Prepared thin films were centered

between two steel washers (2.54-cm outer diameter and 1.27-cm inner diameter) and mounted in the front wheel using threaded retaining rings (Figure 3-7). The 1.445 mCi ^{99}Tc electrode was mounted in a silicon stopper in the rear wheel of the filter mount (Figure 3-8). To expose a scintillator-loaded sample film to the ^{99}Tc source, the source was rotated behind the sample to the 8 o'clock position where the camera was focused. All sample films were exposed to the source for 45 minutes and an image collected on the CCD camera in a chosen region of interest (ROI). The ROI encompassed the exposed film surface, washer, and retaining ring in a 250x250 pixel area.

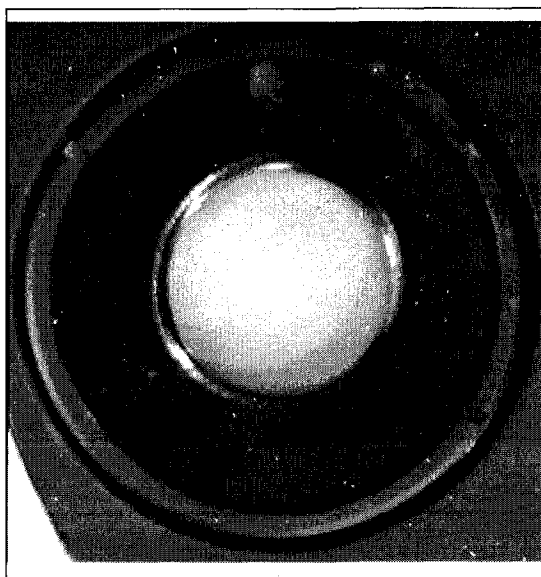


Figure 3-7. Scintillator-loaded sample film mounted between two washers in front wheel of filter mount.

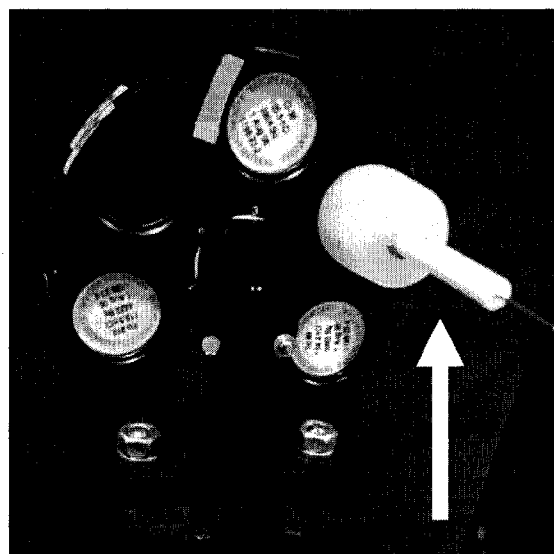


Figure 3-8. Rear wheel of the indexed filter mount with ^{99}Tc electrode (see arrow) mounted in silicon stopper.

Calculated statistics included the minimum, maximum, mean, standard deviation, and sum of the intensities within the ROI. The UV-transmittive filter was placed over the lens during measurement to exclude collection of visible light. Data were not corrected

for ambient background intensity but were processed for localized spikes in intensity due to background cosmic radiation interaction with the silicon in the CCD. This software feature compares adjacent pixel values after data acquisition and interpolates those determined to be from cosmic ray effects before data storage.

3.4 Results and Discussion

3.4.1 Polymer Solution and Film Evaluation

3.4.1.1 Polymer Solution Evaluation

The initial study of polymer dissolution in various solvents was intended to reduce the candidate combinations to those that resulted in clear solutions with no settling after 24 hours. Table 3-4 summarizes the polymer and solvent combinations that were evaluated.

Table 3-4. Evaluated polymer and solvent combinations. "X" indicates complete dissolution and clear solutions. See Table 3-1 and Table 3-2 for polymer and solvent acronyms.

Polymer	Acetic Acid (glacial)	1-Butanol	CCl ₄	Chloroform	Cyclohexane	Cyclohexanone	Diacetone Alcohol	Dichloromethane	DMA	DMF	DMSO	EtOH	Ethyl Acetate	Heptane	Hexane	NMP	2-Propoanol	THF	Toluene	p-Xylene
EVA(b)			X																X	X
PE(a)																			X	X
PIB(a)			X	X	X									X	X			X		
PIB(b)			X	X	X										X			X		
PIB(c)			X																	
PVA											X									
PVAc	X					X	X	X	X	X	X		X			X		X	X	
PVB(c)	X	X					X		X	X	X	X				X		X		

In many cases incomplete dissolution may have been resolved with additional solvent; however, in the first evaluation 1 g of polymer was added to 20 mL solvent regardless of the molecular weight of the polymer. This polymer mass to solvent volume ratio was selected as a condition for suitable films.

3.4.1.2 Polymer Film Evaluation

Each of the polymer solutions from Table 3-4 marked with an “X” (indicating complete dissolution and clear solutions) was drawn into 1270- μm films. Polymer solutions that produced thin films with smooth surfaces and released without deformation were considered for further evaluation.

Films prepared with PIB could not be removed from the release paper without significant stretching or tearing, while those prepared with PE cracked upon removal. Films prepared with PVA and PVAc resulted in clear, removable films that were too rigid for practical application for this project. Blends of solvents for a given polymer, and blends of polymers for a given solvent,

were evaluated but were considered outside of project scope and the results are not included. Similarly, the use of plasticizers and fillers was not investigated.

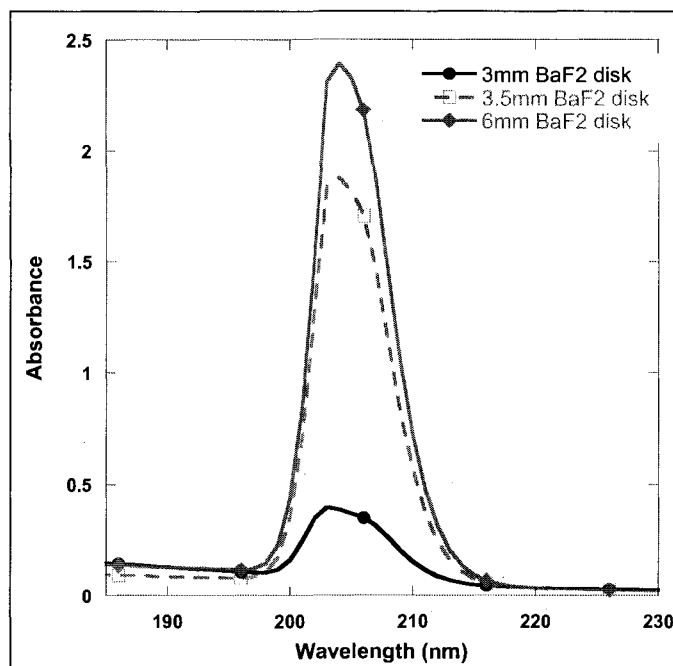


Figure 3-9. Absorbance of BaF₂ optical disks of various thicknesses. (N₂ atmosphere, 120 nm/min scan, reduced slit, solid sample holder).

EVA polymer, with 40 wt% vinyl acetate, in CCl_4 was chosen as the polymer solution for use in scintillator-loaded films. The EVA in CCl_4 films were clear, flexible, and released without deformation, even at wet thicknesses as thin as 508 μm .

3.4.2 BaF_2 Characterization

3.4.2.1 UV-Visible Absorption Measurements

Pure BaF_2 optical disks exhibit maximum UV absorbance at 204 nm that increases with path length (disk thickness) due to increased absorption and scatter losses within the disk (Figure 3-9). However, these losses do not overlap with the scintillations at 195, 220, and 310 nm and the intrinsic absorbance of BaF_2 should not impact the light yield.

3.4.2.2 Scanning Electron Microscopy

SEM imaging of prepared BaF_2 samples (Figure 3-10 and Figure 3-11) verified that individual particles averaged $\leq 5 \mu\text{m}$, as purchased, and ranged from approximately 0.25 – 5 μm . The prepared particles typically agglomerated into larger clusters, likely due to the induction of electrostatic charges from sample preparation.

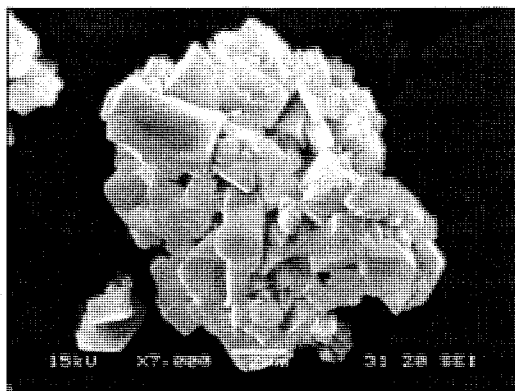


Figure 3-10. SEM image of BaF_2 particles at 7000x magnification (SEI mode, 15 kV).

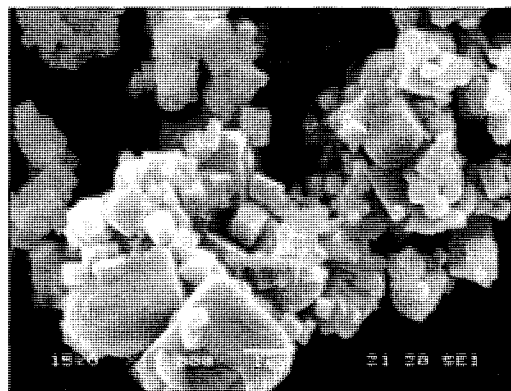


Figure 3-11. SEM image of BaF_2 particles at 11,000x magnification (SEI mode, 15 kV).

Scatter losses are usually considered negligible for particles that are small relative to the wavelength of the radiation being transmitted. As the particle size increases so does the fraction of transmitted photons that are scattered, with a resulting decrease in transmission intensity. The individual BaF_2 particles and agglomerates are significantly larger than the UV wavelengths of BaF_2 scintillation and scatter losses cannot be neglected. The large particle sizes do afford some advantage in that a large target increases the probability of interaction of the incident ionizing radiation with the target scintillator.

3.4.3 BaF_2 -Loaded Polymer Film Characterization

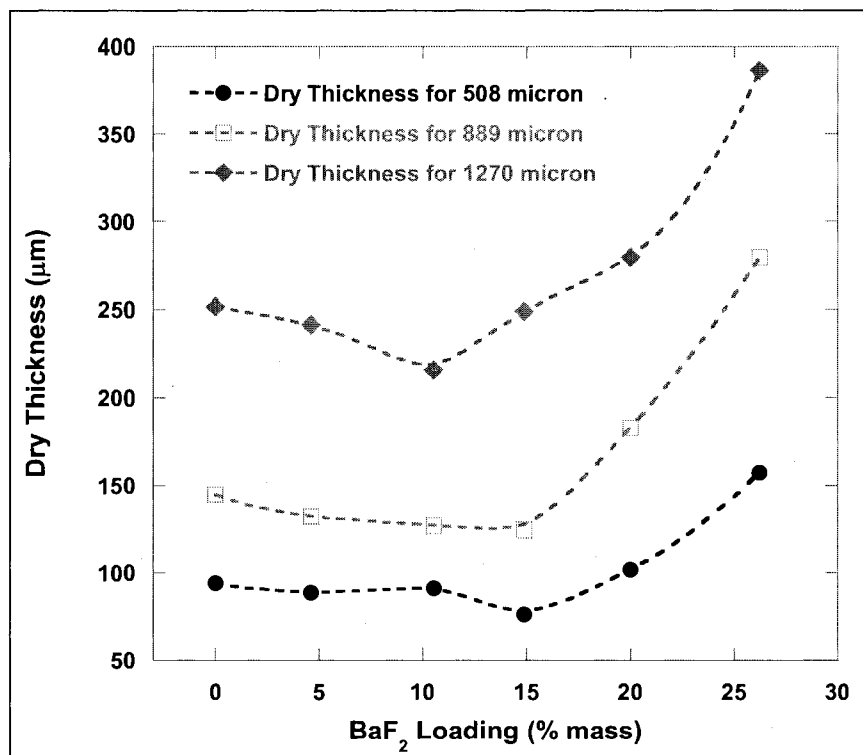


Figure 3-12. Dry film thickness as a function of BaF_2 mass loading in films drawn wet at 508, 889, and 1270 μm.

For films with <15% BaF₂, the dry thickness of the EVA films was independent of the mass loading. When dried, the films were consistently about 20% of their wet thickness at application. However, for loadings > 15% the dry thickness increased (Figure 3-12) and the films became less flexible with less uniform surfaces.

3.4.3.1 UV-Visible Transmittance Measurements

Transmittance was measured between 185 and 350 nm to encompass the BaF₂ scintillations at 195, 220, and 310 nm. UV-vis kinetic scanning verified that the films were thoroughly dried after 90 minutes and there was no residual absorption attributable to CCl₄.

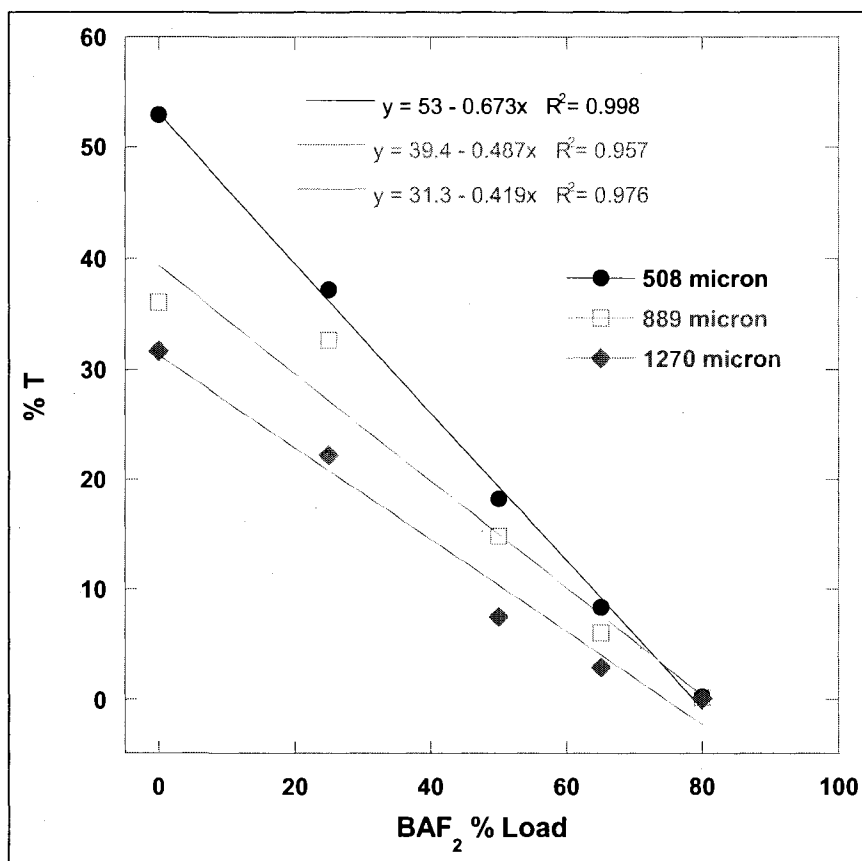


Figure 3-13. BaF₂-loaded EVA film transmittance at 310 nm as a function of loading for increasing drawn film thicknesses.

Incident light at 195 and 220 nm was not transmitted through the EVA films due its absorbance of those wavelengths. Light at 310 nm was transmitted nearly constantly at $61 \pm 6\%$ through EVA-only films drawn between 508 and 1270 μm . As BaF_2 is loaded into the films, transmittance at 310 nm decreases with both increasing BaF_2 (Figure 3-13) and increasing drawn thickness (Figure 3-14). Transmittance reaches zero for films loaded with 80% by mass BaF_2 independent of the drawn thickness, indicating absorption is primarily due to the BaF_2 and not the EVA at 310 nm.

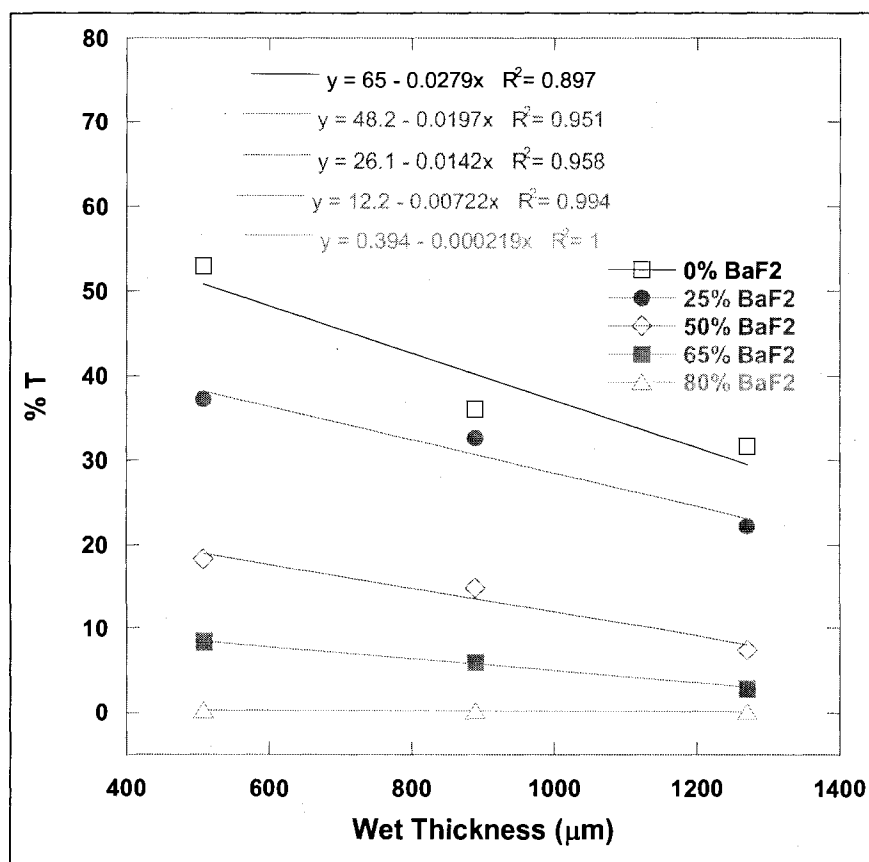


Figure 3-14. BaF_2 -loaded EVA film transmittance at 310 nm as a function of drawn film thicknesses for increasing loading.

The scintillations, however, are not incident on the film nor do they need to be transmitted through its entire path length. Since they are instead produced within the loaded film, their path length and hence their potential for scatter and absorption within the film decrease with the increasing range of the source beta particle.

3.4.3.2 Scintillation Counting

An image of the background intensity from the ^{99}Tc electrode is presented in Figure 3-15. Highlighted in concentric rings from inside to outside are the copper wire (dark), ^{99}Tc (bright white), PTFE sleeve, and silicon washer bounded by the filter wheel opening. The electrode is off-center but within an ROI selected for data analysis. The same image is presented as a 3-dimensional plot in Figure 3-16.

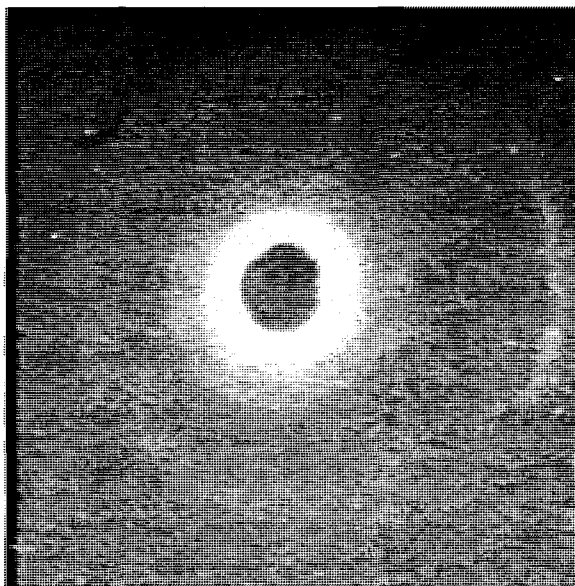


Figure 3-15. Intensity image of ^{99}Tc electrode behind stainless steel washers (PIXIS 512BUV, UV-Nikkor 150-mm, 45 min exposure, f/4.5, 50-cm film-to-CCD).

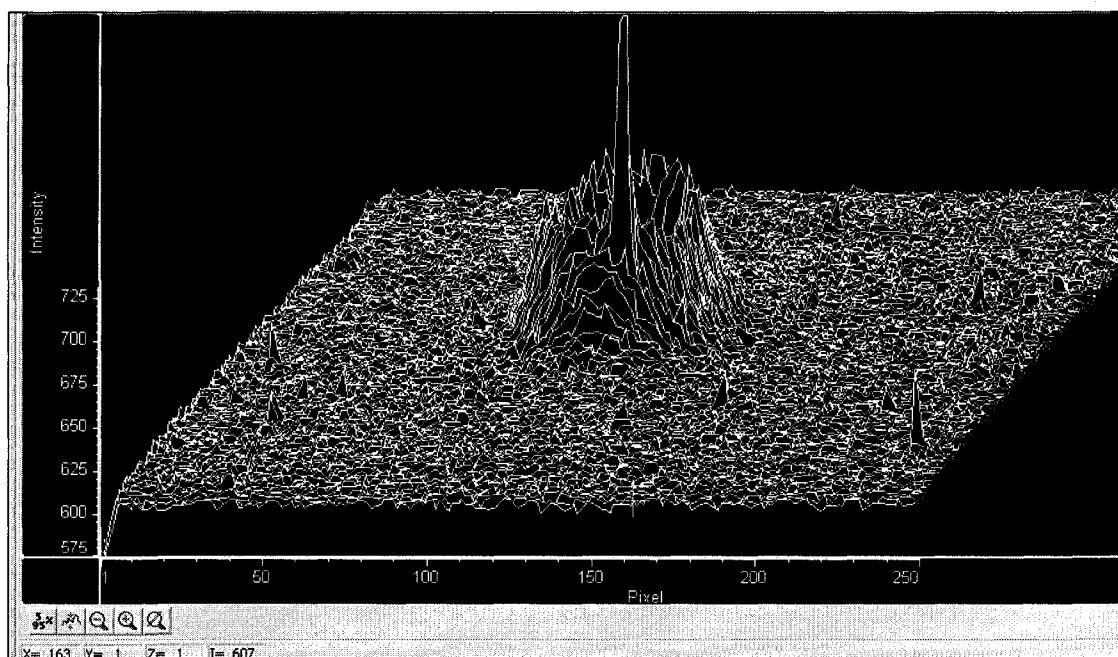


Figure 3-16. 3-D intensity image of ^{99}Tc electrode behind stainless steel washers. Cosmic radiation interaction with CCD shown in localized spike in center. (PIXIS 512BUV, UV-Nikkor 150-mm, 45 min exposure, f/4.5, 50-cm film-to-CCD).

The glass filter mounted to the lens during scintillation counting transmits photons in the UV and IR regions as shown in Figure 3-17. In addition to UV detection as designed, the CCD of the camera responds to visible and near-IR photons with wavelengths < 1000 nm (Figure 3-18). Background IR sources should not penetrate the

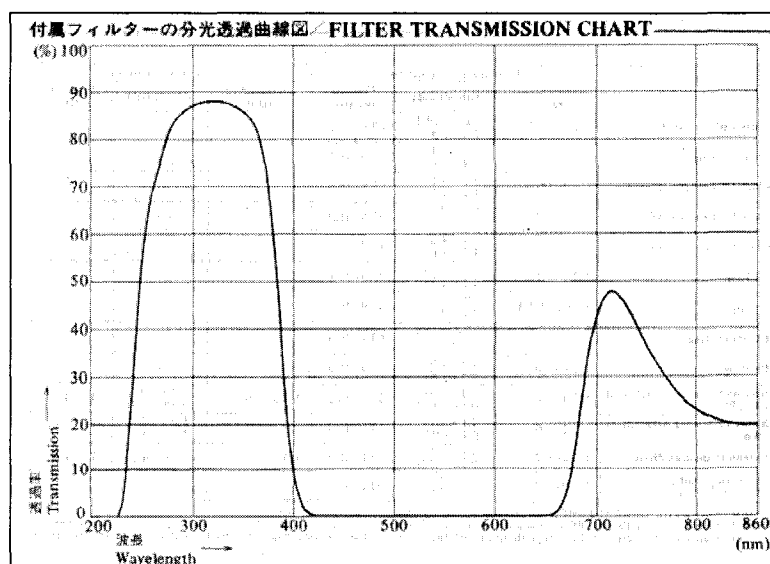


Figure 3-17. Transmission spectra for Nikon UV Transmission Filter. Reproduced from User's Manual.

dark box, however the camera is thermoelectrically air-cooled and the exhausted heat is a potential IR source within the dark box itself.

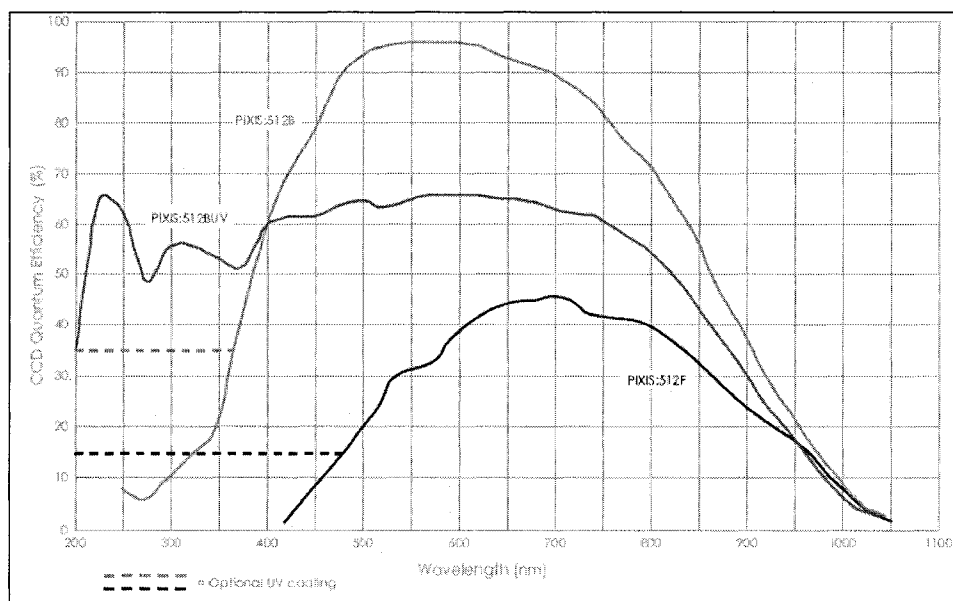


Figure 3-18. Quantum efficiency spectra for PIXIS CCD cameras. From www.piacton.com.

Beta particles, such as those emitted in the decay of ^{99}Tc , lose energy through interactions with the orbital electrons of an absorbing material. These interactions consist primarily of inelastic collisions with absorber orbital electrons and of coulomb interactions with absorber nuclei. An incident beta particle imparts energy to the absorbing material through inelastic collisions, resulting in excitation of the absorber orbital electrons. When an average of 2-3 times the first ionization potential of the absorbing material has been imparted, ionization of the least tightly bound electron results in an ion pair, consisting of the ejected electron and the remaining positively charged atom. In addition, as an incident beta particle or an ejected electron passes near

the nucleus of an absorbing material atom, the positive charge of the nucleus causes a strong coulomb attraction with the negatively charged particle and a sharp change in its direction. The change in direction results in rapid acceleration and a proportional energy loss in the form of X-rays, or Bremsstrahlung radiation (Cember, 1996).

To determine the source of the detector response for the ^{99}Tc electrode without the intentional presence of a scintillator, beta particle ranges and the energies of the Bremsstrahlung radiation produced by their interaction with available materials are calculated. The range of a beta particle is the distance it traverses a material before being completely attenuated and its full energy is absorbed. Range is dependent on the density of the absorber and the maximum energy of the beta particle (Shleien et al., 1998) such that

$$R = 0.412 \cdot E_{\beta}^{1.265 - 0.0954 \ln E_{\beta}}$$

R is the range (g/cm^2) and E_{β} is the maximum energy of the beta emitter (MeV).

For ^{99}Tc , $E_{\beta} = 0.294$ MeV and the resulting $R = 0.076$ g/cm^2 . If the density of the absorber is known, the charged particle's range can be given in terms of the absorber's linear thickness. In the system geometry used to collect the images in Figure 3-15 and Figure 3-16, β^{-} primarily interact with the electrode's copper wire and PTFE sleeve, air, the washers, and the glass filter.

Since the source-to-lens distance is approximately 35 cm, unattenuated beta particles can reach the lens filter through air but then are fully absorbed. The calculated ranges (Table 3-5) indicate they are fully attenuated in all potential absorbers and would not contribute to the CCD response.

Table 3-5. Calculated linear range in various absorbers of beta particles from ^{99}Tc electrode. Density values from Shleien et al., 1998.

Absorber	Density (g/cm ³)	β^- range (cm)	β^- range (μm)
Copper	8.96	0.01	85
PTFE (C ₂ F ₄)	2.2	0.03	345
Air	1.29E-3	58.9	5.9E04
Stainless steel	7.8	0.01	97
Glass	2.4 – 2.8	0.03	317

The energy of Bremsstrahlung radiation depends on the energy of the incident beta particle and the atomic number of the absorber. The average energy, E_{ave} , of ‘external’ or ‘outer’ Bremsstrahlung can be determined (NCRP, 1985) from

$$E_{ave} = 1.4 \times 10^{-7} \cdot Z \cdot E_{\beta}^2 \text{ keV per } \beta$$

Z is the absorber atomic number and E_{β} is the maximum energy of the beta emitter (keV).

The effective atomic number, Z_{eff} , of a compound can be calculated from

$$Z_{eff} = [f_1 (Z_1)^{2.94} + f_2 (Z_2)^{2.94} + f_3 (Z_3)^{2.94} + \dots f_n (Z_n)^{2.94}]^{1/2.94}$$

f_n is the fraction of total electrons associated with the n th element and Z_n is the atomic number of the n th element (Spiers, 1946).

The calculated energies and wavelengths of potential Bremsstrahlung radiations are in the X-ray region as expected (Table 3-6). Even for interactions with a hydrogen atom with $Z_{eff} = 1$, the resulting average Bremsstrahlung wavelength is 103 nm. Similar to the discrimination against cosmic radiation, the use of a spatial correction in the CCD response should limit the contributions of Bremsstrahlung radiations. Also, the CCD response to a high energy photon results in a localized, high intensity spike as seen in Figure 3-16. The combination of the filter transmission and the CCD response limit the

incident radiation to either UV or near IR. As such, exclusion of ^{99}Tc beta particles and Bremsstrahlung radiation suggests the source of detector response in the absence of a scintillator is reflected IR radiation emitted from the camera housing.

Table 3-6. Calculated average energy of Bremsstrahlung radiation from ^{99}Tc β^- interactions with external absorbers. Z_{eff} values from Naydenov (2003).

Absorber	Z_{eff}	E_{ave} (keV)	E_{ave} (nm)
Copper	29	0.35	3.5
PTFE	5.9	0.07	17.5
Air	7.5	0.09	13.2
Stainless steel	27	0.33	3.8
Glass	11	0.13	9.3

Since the range of the incident β^- depends on the attenuating potential of the film, the addition of the high density BaF_2 ($\rho = 4.89 \text{ g/cm}^3$) to the films significantly changes the range of the incident β^- . Since $R = 0.076 \text{ g/cm}^2$ is constant and independent of the absorber, the ^{99}Tc β^- in pure BaF_2 has a range of only $155 \mu\text{m}$. Pure EVA has a reported density of $0.93 - 0.95 \text{ g/cm}^3$ (Lide 2007) and based on the percent mass of EVA to BaF_2 , an effective density can be calculated to determine the β^- range in a given film (Table 3-7). The attenuating potential of the film depends on its density thickness (g/cm^2), defined as the product of a material's density (g/cm^3) and its linear thickness (cm). For BaF_2 -loaded films, density thickness is then the product of the film effective density and dry thickness. These parameters are listed in Table 3-7.

Table 3-7. Film effective density and density thickness as a function of BaF₂ loading and ⁹⁹Tc β⁻ ranges in those films.

BaF ₂ Loading (% mass)	Effective Density (g/cm ³)	Dry Thickness or Range (μm)				Density Thickness (g/cm ²)		
		⁹⁹ Tc β ⁻ range	Film 508 μm wet	Film 889 μm wet	Film 1270 μm wet	Film 508 μm wet	Film 889 μm wet	Film 1270 μm wet
0	0.94	809	94	144.8	251.5	8.8E-03	1.4E-02	2.4E-02
25	1.93	394	88.9	132.1	241.3	1.7E-02	2.5E-02	4.7E-02
50	2.92	260	91.4	127	215.9	2.7E-02	3.7E-02	6.3E-02
65	3.51	217	76.2	124.5	248.9	2.7E-02	4.4E-02	8.7E-02
80	4.10	185	101.6	182.9	279.4	4.2E-02	7.5E-02	1.1E-01

The β⁻ range and film density thickness can be co-plotted to determine at what BaF₂ loading the range is exceeded (Figure 3-19).

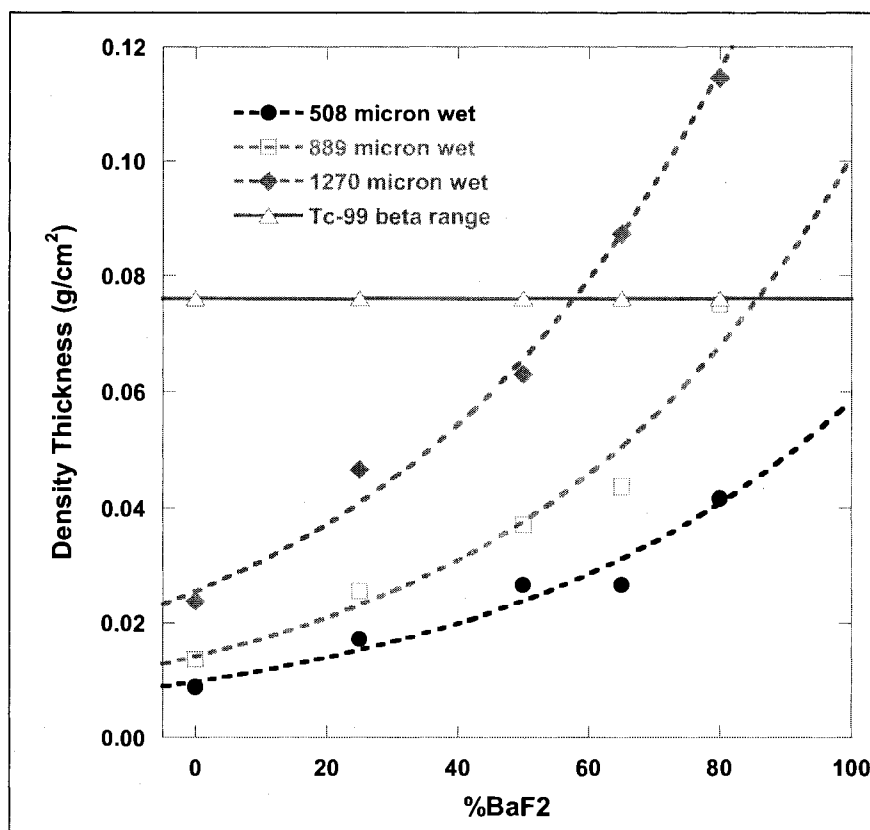


Figure 3-19. Film density thickness and β⁻ range as a function of BaF₂ mass loading in films drawn wet at 508, 889, and 1270 μm.

As the BaF₂ mass loading increases, so does the film density thickness, the attenuation of β^- , and therefore the number of scintillations produced within the film until the beta particle range is reached. At this loading, all incident β^- and any secondary electrons produced from ionizations are attenuated and the total scintillations produced in the film plateau. This range is reached in a 1270 μm (wet) BaF₂-doped EVA film when the BaF₂ mass loading is approximately 60% and in an 889 μm film at 80%. The range is not reached in the 508 μm films for the loads investigated.

‘Detectable’ scintillations are those that reach the CCD without being absorbed. For a scintillation to occur, the energy from the decay of the residual radioactive material must be deposited in the scintillator crystal rather than the polymer. As the mass of BaF₂ increases relative to that of EVA, and hence the relative mole ratio, the probability of scintillation increases. Since scintillations are generally produced isotropically, detection geometry introduces solid angle losses which increase proportional to the square of the film-to-CCD distance. Scattering of the scintillations increases the effective distance they traverse through a medium and therefore increase the probability of absorption in media such as the film, air, and detector. Absorption of the 195 and 220 nm scintillations in the film occurs due to EVA (Figure 3-14) rather than BaF₂ (Figure 3-9). However, as the BaF₂ load increases, the elevated scatter results in a higher probability of absorption by the EVA. At room temperature, the fast component scintillations (195 and 220 nm) account for 20% of the total scintillations (§2.3) and therefore detectable scintillations are only likely for the remaining 80% due to the slow component at 310 nm. The camera lens transmits nearly 90% at 310 nm (Figure 3-17), but the camera only responds to approximately 50% of the incident scintillations (Figure 3-18).

Detectable scintillation intensities are likely to be significantly lower than those produced but the fixed source and detection geometry enables comparison of varying films. Figure 3-20 through Figure 3-23 are provided as examples of the recorded image and 3-dimensional intensity plots for 80% BaF₂ films of differing thicknesses (1270 and 508 μm).

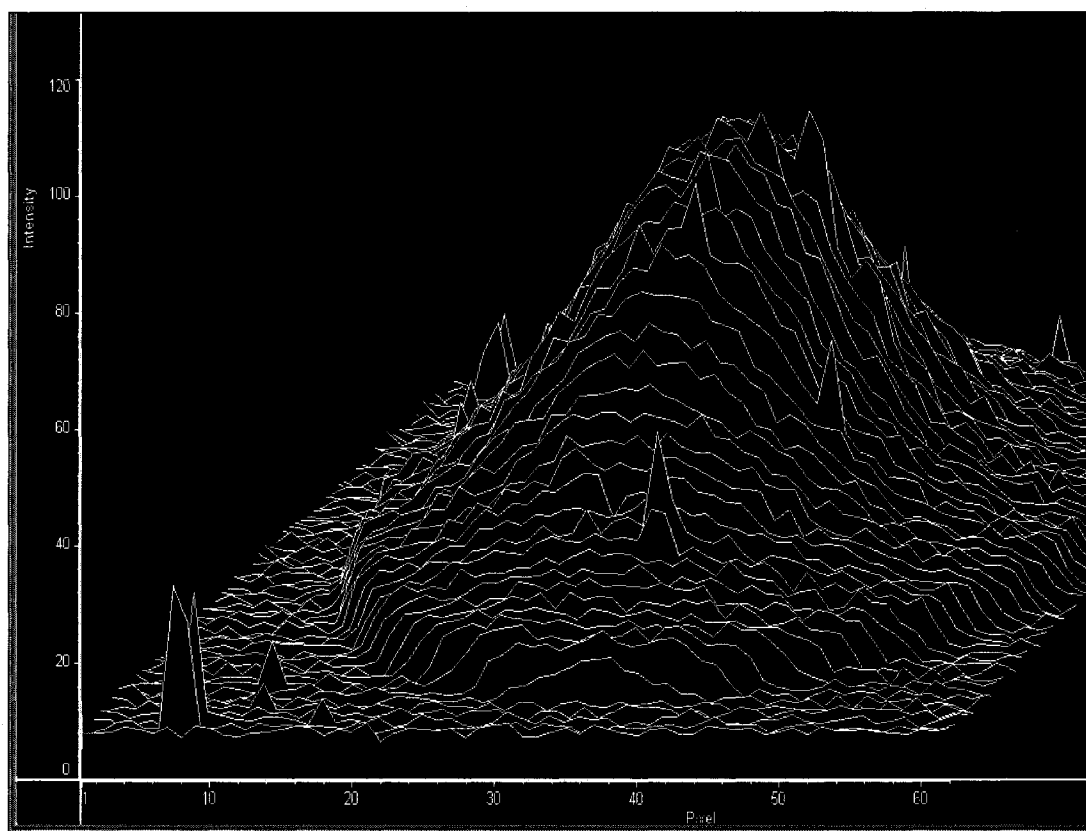


Figure 3-20. Intensity plot for 80% BaF₂-loaded, 1270 μm (wet) EVA film in holder exposed to 1.445 mCi ⁹⁹Tc electrode for 45 min.

The higher intensity of the thinner film is evident by the wider bright area in the image and the higher intensity of the ridge in the 3-D plot where the film is exposed through the stainless steel washer.

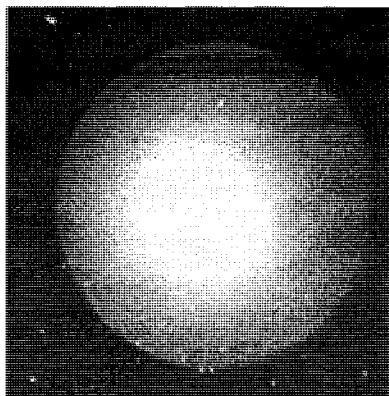


Figure 3-21. Image of 80% BaF₂-loaded, 1270 μ m (wet) EVA film exposed to 1.445 mCi ⁹⁹Tc electrode for 45 min.

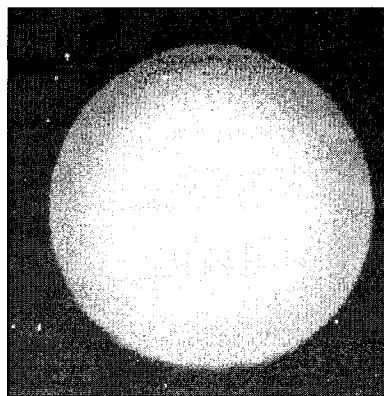


Figure 3-22. Image of 80% BaF₂-loaded, 508 μ m (wet) EVA film exposed to 1.445 mCi ⁹⁹Tc electrode for 45 min.

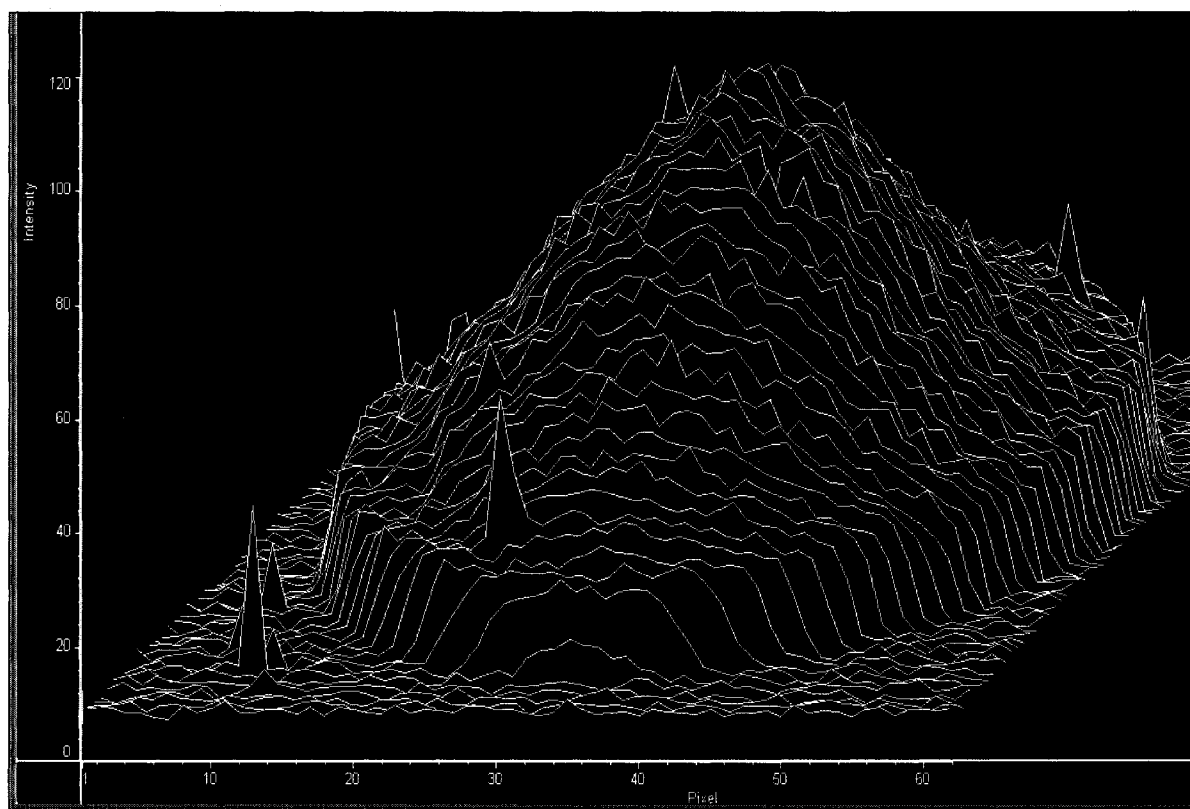


Figure 3-23. Intensity plot for 80% BaF₂-loaded, 508 μ m (wet) EVA film in holder exposed to 1.445 mCi ⁹⁹Tc electrode for 45 min.

The scintillations were averaged over the ROI for each film and the mean of the 0% BaF₂ film subtracted from the others of that thickness. The resulting net mean intensities for all films are summarized in Figure 3-24 against BaF₂ loading and in Figure 3-25 against drawn thickness. Inflection points are observed near 60% BaF₂ load for the 1270 μ m film and 80% BaF₂ for the 889 μ m film, but one is not observed in the 508 μ m film for the loads investigated. These agree with the expected dependence of scintillation intensity on the range of the beta particles in a film and therefore on the BaF₂ load. In addition, the contrast between the 508 and 1270 μ m films with 80% BaF₂ highlighted in the figures above is supported by the difference in measured intensities.

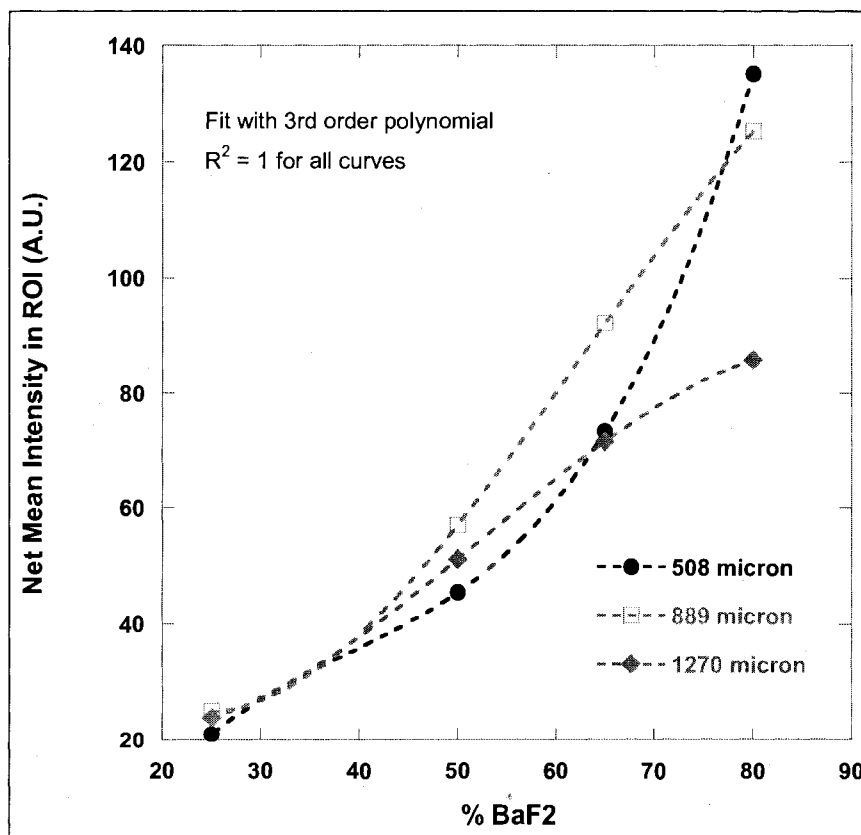


Figure 3-24. Net mean scintillation intensity for films of varying thickness as a function of BaF₂ mass loading.

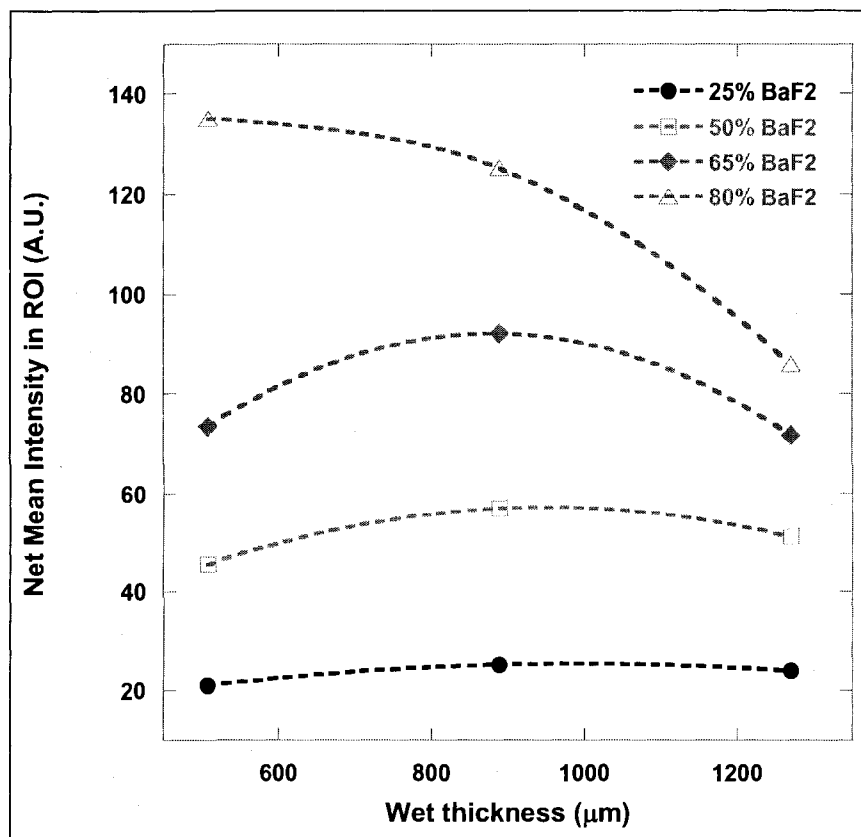


Figure 3-25. Net mean scintillation intensity for films of varying BaF₂ mass loading as a function of drawn (wet) thickness.

3.5 Conclusions

Passive detection of the presence of surface, residual radioactive materials is challenging, yet achievable, using scintillation counting. The maximum potential scintillation intensity is governed by the rate and type of radioactive material decay as well as the light yield of the scintillator. Detectable scintillations are reduced from this maximum by losses due to source attenuation, scintillation scatter and absorption, background noise, and detection geometry. The use of a 1.445 mCi ⁹⁹Tc source in this research is likely to far exceed the source strengths encountered on surfaces. While the use of solar-blind scintillators, such as BaF₂, offer the advantages of reduced solar UV

background and daylight detection operations, their low light yield relative to other visible region scintillators must be considered. Since scatter increases with the scintillator particle size, the use of nanoparticles would ensure the particles are much smaller than the wavelength of their scintillations to minimize potential scatter and subsequent absorption by surrounding media. Nanoparticles also afford high loading in thin films, which has been shown to maximize scintillation production while minimizing absorption losses. Requiring the scintillator-loaded coating to be strippable compounds the difficulty in choosing an appropriate polymer that will not absorb the scintillations. While EVA produced clear, flexible, and strippable films, it absorbs the fast scintillations of BaF₂ at 195 and 220 nm, which account for 20% of those produced at room temperature. The use of other polymers, such as polyethylene or polypropylene, which are transparent to solar-blind wavelength photons may require the use of plasticizers to enhance their flexibility and strippability. These plasticizers must in turn be UV-transparent. Finally, the feasibility of remote detection is governed by the distance of the surface of interest to the detector. The solid angle losses for an isotropically-scintillating source reduce the effective scintillation intensity so dramatically that the exposures times required for adequate signal-to-noise ratios may make detection impractical for a given distance.

CHAPTER 4

LASER-INDUCED FLUORESCENCE EXPERIMENTS

4.1 Introduction

These experiments investigate the effects of iron(III) and polyhedral oligomeric silsesquioxane (POSS[®]) ligands on the fluorescence of uranyl in solids. Uranyl fluorescence is quenched by an electron transfer between the excited free uranyl ion, $(\text{UO}_2^{2+})^*$, and metal ions such as Fe^{3+} that results in the transition of uranyl to its ground state without fluorescent emission. The goals of these experiments were to: (1) select an iron(III) concentration sufficient to quench the fluorescence of uranyl solids; (2) determine the acid concentration required to maintain buffered-ethanol solutions at their first pK_a following the addition of POSS[®] ligands, (3) characterize the effect of contacting those solutions with uranyl solids, in the absence and presence of iron(III), on the uranyl fluorescence intensity and lifetime; and (4) determine if the addition of POSS[®] ligands to the solutions enhances the uranyl solid fluorescence intensity or lifetime in the absence and presence of iron(III).

Two POSS[®] ligands were chosen based on their potential to complex UO_2^{2+} or Fe^{3+} and thereby provide sufficient shielding of the uranyl ion from quenching. Ethanol (EtOH) also quenches uranyl fluorescence by electron transfer (§4.2.2) but is used as a solvent for multidentate POSS[®] ligands that are insoluble in water. The laser-induced

fluorescence intensity and lifetimes of uranyl solids were measured following contact with POSS[®] solutions, both in the absence and presence of Fe³⁺.

The principles underlying the analytical and characterization techniques of ultraviolet-visible absorption spectrometry, atomic emission spectrometry, and visible fluorescence spectrometry used in these experiments were summarized in Chapter 2. Background information relevant to the discussion in this chapter regarding uranyl speciation and fluorescence is summarized in §4.2. The materials and methods used to conduct laser-induced fluorescence intensity and lifetime measurements are described in §4.3.1. Stock solution and sample preparations are described in §4.3.2 and §4.3.3 followed by the stock solution characterization results in §4.4.1. Experimental results for the effects of iron, POSS[®], and POSS[®] with iron on uranyl fluorescence are presented and discussed in §4.4.2, §4.4.3, and §4.4.4, respectively. Conclusions are highlighted in §4.5.

4.2 Background

4.2.1 Uranyl Fluorescence Intensity

Hexavalent uranium as the rigid, linear UO_2^{2+} is highly fluorescent partly due to a reduction in the internal conversion processes that deactivate the excited ion without emission (Skoog et al., 2007). However, because the transitions resulting in uranyl fluorescence are electronic in nature, their intensity is affected by speciation, molecular structure, and chemical environment (Syt'ko and Umreiko, 1998). Complexation of uranyl can result in increased molar absorptivity, fluorescence intensity, and fluorescence lifetime with an accompanying emission red-shift. For example, these properties increase

with the number of coordinated hydroxyl groups and with pH. Free uranyl fluorescence maxima occur at 473, 488, 509, 534, 560, and 588 nm with a lifetime that is measurable using time-resolved spectrometry (Bell and Biggers, 1965; Geipel et al., 2000). The change in peak location as a function of the solution pH is highlighted in Table 4-1. Note that Peaks 2, 3, and 4 each red-shift 9-10 nm between the listed pH ranges. Although not evident from the table, the well-defined uranyl emission peaks are broadened significantly at pH 7, and the spectrum resembles a continuum (Figure 4-1).

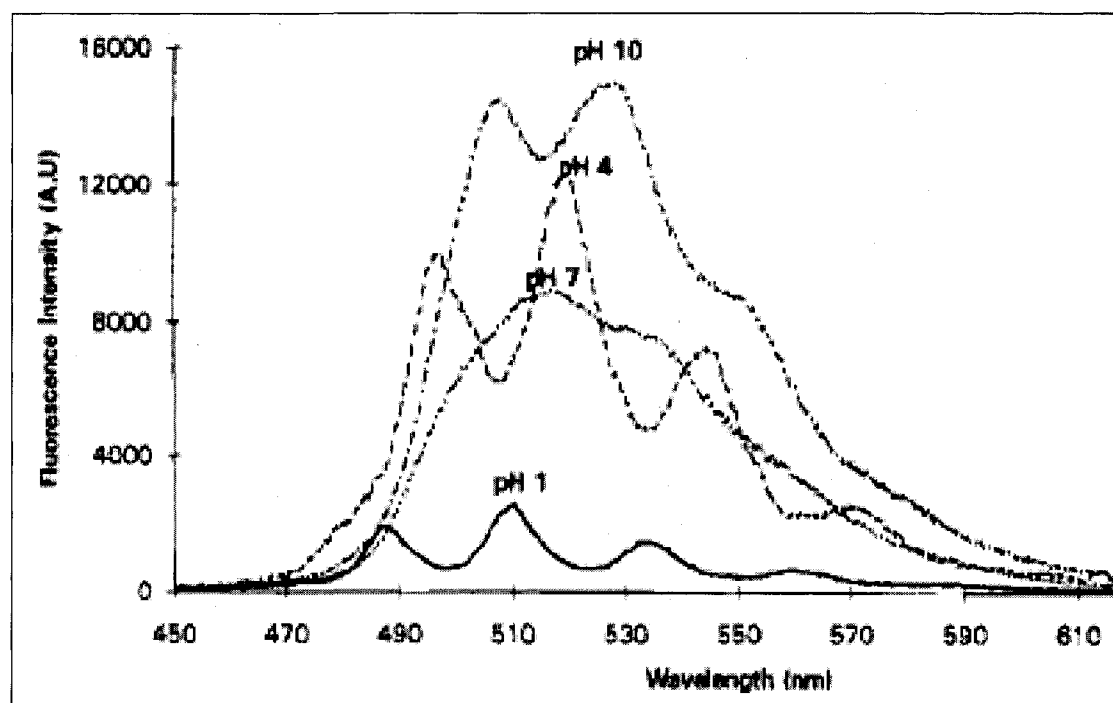


Figure 4-1. Example of uranyl fluorescence dependence on pH. From Moulin, C.; Decambox, P.; Moulin, V.; Decaillon, J. G. Uranium Speciation in Solution by Time-Resolved Laser-Induced Fluorescence. *Anal. Chem.* **1995**, *67*, p 349.

Table 4-1. Reported uranyl fluorescence peaks in solution for pH 1 to 10. Adapted from Baumann et al., 2005; Gunther et al., 2007; Kirishima et al., 2004; Meinrath et al., 1993; Meinrath 1997; and Moulin et al., 1995. sh \equiv shoulder

Uranyl fluorescence wavelengths (nm) between 22-24 °C						
pH	Peak 1	Peak 2	Peak 3	Peak 4	Peak 5	Peak 6
1	471 - 473	487 - 488	509 - 510	533 - 534	559 - 560	584 - 588
4		497	520	544	570	
7			516	533 (sh)		
5 - 8.5	478 - 482	497 - 499	518 - 521	540 - 544	562 - 565	586 - 590
10		507	528	552 (sh)		

4.2.2 Uranyl Fluorescence Quenching

Uranyl fluorescence is known to be dynamically quenched as the result of electron transfers with metal ions (Burrows et al., 1985; Matsushima et al., 1974; Moriyasu et al., 1977) and alcohols (Sakuraba and Matsushima, 1971; Wheeler and Thomas, 1984). The following is a discussion regarding the mechanism of iron quenching to illustrate its effect on measured fluorescence intensities and lifetimes. Ethanol used in these experiments also dynamically quenches uranyl fluorescence and more information may be found in the references provided.

Upon collision of the excited uranyl ion, $(\text{UO}_2^{2+})^*$ and Fe^{3+} ions, Fe^{3+} either abstracts the excited electron from $(\text{UO}_2^{2+})^*$ or transfers an electron to it (Meinrath, 1997). In either case, the deactivation of $(\text{UO}_2^{2+})^*$ to the ground state UO_2^{2+} without emission is called dynamic quenching. The probability of uranyl fluorescence being dynamically quenched increases with temperature and with $[\text{Fe}^{3+}]$. Quenching effects are typically reported as the ratios I_o/I or τ_o/τ , where I_o and τ_o are the fluorescence intensity and lifetime measure in the absence of a quencher. These ratios can also be used to determine the quencher concentration required to produce a desired effect. For example, to ensure

uranyl fluorescence intensity was sufficiently quenched prior to contact with POSS[®] ligands, an iron concentration was chosen to provide at least 75% quenching or an I_0/I ratio ≥ 4 . At this ratio, any further quenching or potential enhancement of the fluorescence intensity attributable to the POSS[®] solution would still be observable (§4.4.2.1). Uranyl fluorescence quenching can also be static, in which the quencher forms a non-fluorescent, or dark, complex with the ground state UO_2^{2+} . Stern-Volmer plots allow comparison of I_0/I to τ_0/τ for a given quencher concentration, and highlight differences between dynamic (Figure 4-2) and static (Figure 4-3) quenching that cannot be observed using solely intensity measurements. Dynamic quenching is characterized by an equivalent decrease in fluorescence intensity and lifetime such that I_0/I always equals τ_0/τ . In contrast, static quenching results in decreasing intensity with increasing quencher concentration, but has no affect the lifetime and $\tau_0/\tau = 1$.

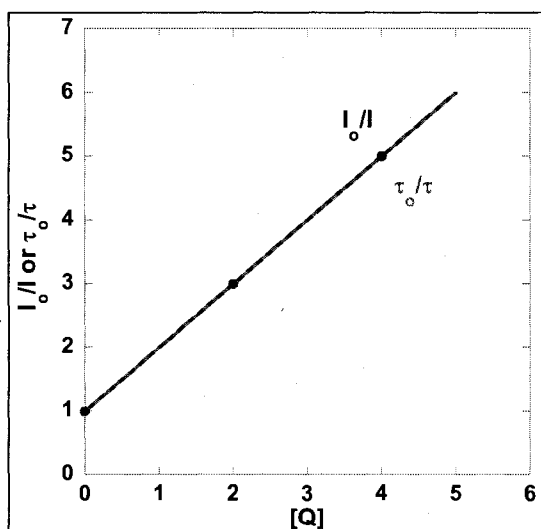


Figure 4-2. Dynamic quenching.

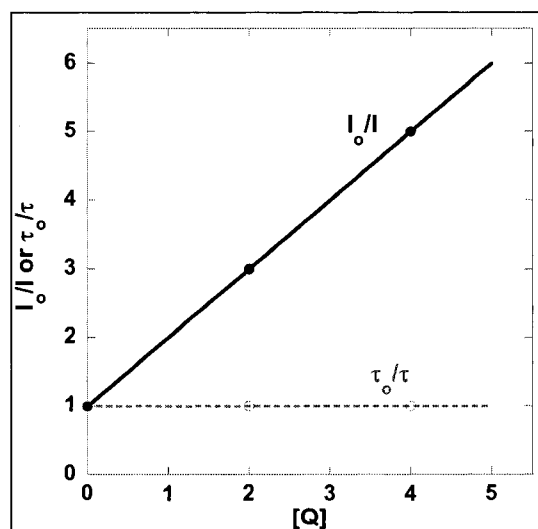


Figure 4-3. Static quenching.

Both figures adapted with permission from Fig. 4.2 of Bernard Valeur: Molecular Fluorescence. Page 90. 2002. Copyright Wiley-VCH Verlag GmbH & Co. KGaA.

4.2.3 Uranyl Fluorescence Lifetime

The uranyl fluorescence lifetime is generally considered to be 2 μ s at 20 °C in acidic (pH < 3) media (Kirishima et al., 2004; Lopez and Birch, 1997; Meinrath et al., 1993; Meinrath, 1997; Moulin et al., 1995). Above pH 3, the emission maxima and lifetimes are convolutions of the individual free and coordinated uranyl species, whose ratios vary with pH. As a result, uranyl lifetimes are often calculated using monoexponential fits of the decaying fluorescence intensity below pH 3 and using biexponential fits above pH 3 (Billard et al., 2001; Bonhoure et al., 2007; Bouby et al., 1999). Lifetimes increase with increasing hydrolysis and concentration and with decreasing temperature. Coordinated hydroxyl groups shield the uranyl ion from the quenching of water and other ligands, resulting in reported lifetimes up to 80 μ s in the absence of other complexers in solution (Kirishima et al., 2004). Published reports indicate that complexation with phosphates results in uranyl fluorescence lifetimes greater than 200 μ s (Meinrath, 1998; Moulin et al., 2005). Decreasing temperature increases the uranyl lifetime in solution from 2 μ s at room temperature to about 270 μ s at liquid helium temperature (Geipel, 2006). Finally, as the concentration or viscosity increases, for example in solids, so does the lifetime due to the decreasing contribution of dynamic (collisional) quenching. DeNeufville et al. (1981) measured lifetimes in excess of 500 μ s in certain uranyl minerals .

4.2.4 Uranium Speciation

The stable uranyl ion, UO_2^{2+} , is coordinated with four, five, or six neighbor ligands in the plane equatorial to the axial oxygens, resulting in absorbance and emission spectra with characteristic transition intensities, positions, and lifetimes. The UO_2^{2+} ion dominates aqueous speciation at pH < 3. As pH increases toward pH 7, UO_2^{2+}

precipitates as Schoepite, $(\text{UO}_2)_4\text{O}(\text{OH})_6 \cdot 6\text{H}_2\text{O}$, and forms polynuclear hydrolysis species if the uranyl concentration is sufficiently high. Species with concentrations greater than 0.1 mM are plotted as a function of pH in Figure 4-4 for an aqueous solution of 4.8 mM $\text{UO}_2(\text{ClO}_4)_2$, the concentration used in this work.

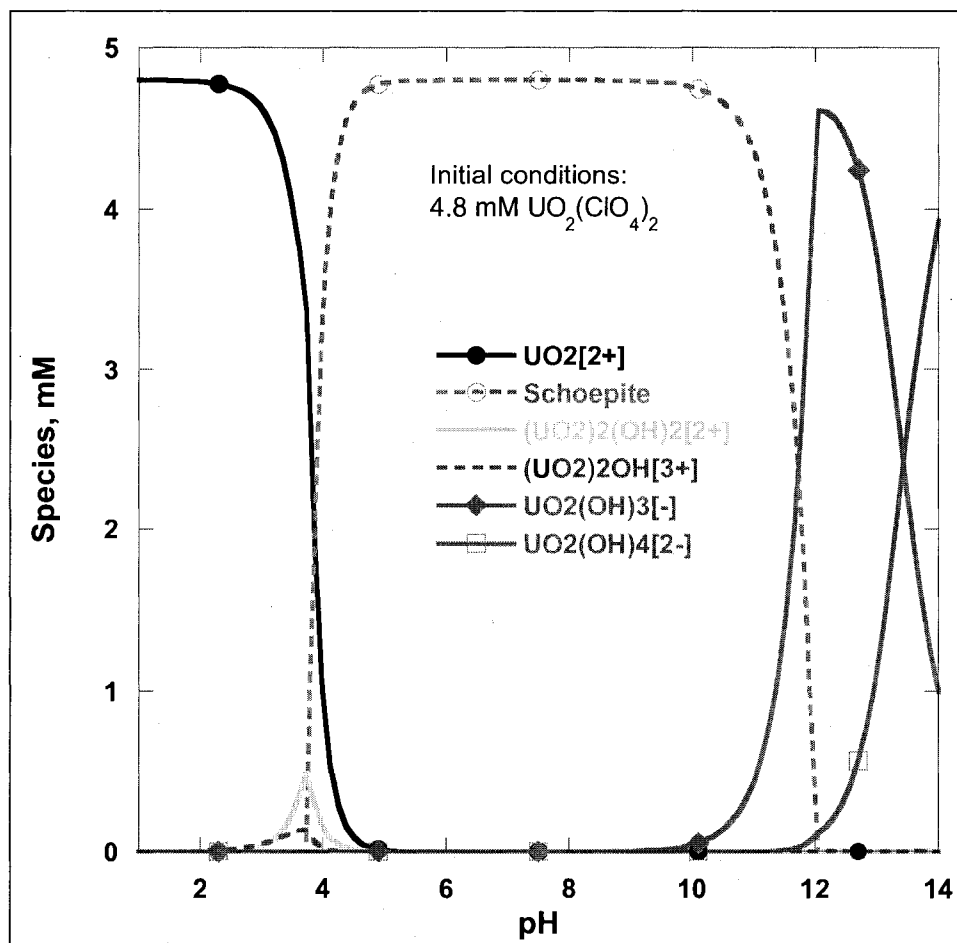


Figure 4-4. Primary uranyl species (≥ 0.1 mM) as a function of pH (JCHESS[®] Version 2.0, Release 3).

4.3 Experimental

4.3.1 Materials and Methods

4.3.1.1 Chemicals

The following chemicals were used as received for experiments.

Table 4-2. Chemicals used for stock solution and sample preparation.

Chemical	Formula	Purity or Form	Vendor	Product No.
Uranyl acetate hydrate (UAc)	$\text{UO}_2(\text{C}_2\text{H}_3\text{O}_2)_2 \cdot 2\text{H}_2\text{O}$	Powder	General Chemical	Cat #2404
Iron(III) perchlorate hydrate	$(\text{Fe}(\text{ClO}_4)_3 \cdot x\text{H}_2\text{O})$	Low-Cl, crystals	Sigma-Aldrich	Cat #326348
Iron(III) chloride	$\text{FeCl}_3 \cdot 6\text{H}_2\text{O}$	97.0-102.0%, powder	EM Science	Cat #FX0210-1
Lithium chloride	LiCl	$\geq 99\%$, powder	Sigma-Aldrich	Cat #L4408
Sodium sulfate	Na_2SO_4	$\geq 99.0\%$, anhydrous, granular powder	J.T. Baker	Cat #3891-01
Sodium fluoride	NaF	$(\geq 99.0\%)$, powder	J.T. Baker	Cat #3688-04
Sodium nitrate	NaNO_3	$\geq 99.0\%$, crystal	J.T. Baker	Cat #3770-01
Sodium metasilicate	Na_2SiO_3	Anhydrous, powder	Alfa Aesar	Cat #14106
Sodium phosphate dibasic	Na_2HPO_4	99.0%, powder,	Sigma-Aldrich	Cat #S7907
TriSilanolEthyl POSS® (SO1444)	$\text{C}_{14}\text{H}_{38}\text{O}_{12}\text{Si}_7$	See Figure 4-5, powder	Hybrid Plastics	Cat #SO 1444
TetraSilanolPhenyl POSS® (SO1460Na)	Sodium salt of $\text{C}_{48}\text{H}_{44}\text{O}_{14}\text{Si}_8$	See Figure 4-6, powder	Hybrid Plastics	Sodium salt of Cat #SO1460
Nitric acid	HNO_3	68-70%	VWR	Cat #VW4815-6
Perchloric acid	HClO_4	60%	Sigma Aldrich	Cat #311413
Sodium hydroxide	NaOH	98.8%, pellets	J.T. Baker	Cat #3722-01
2-Amino-2-methyl-1-propanol (AMP)	$(\text{CH}_3)_2\text{C}(\text{NH}_2)\text{CH}_2\text{OH}$	$\geq 95\%$, viscous liquid	Sigma Aldrich	Cat #A9199
Triethanolamine (TEA)	$(\text{HOCH}_2\text{CH}_2)_3\text{N}$	98%, viscous liquid	Sigma Aldrich	Cat #T58300
Deionized (DI) water	H_2O	18.2 mΩ-cm at 25 °C	Pall	Using Cascade IX Mk2
Ethanol (EtOH)	$\text{CH}_3\text{CH}_2\text{OH}$	200 proof, $\geq 99.5\%$, anhydrous	Sigma-Aldrich	Cat #459836

TriSilanolEthyl POSS®		SO1444
<p>R = ethyl</p>	$C_{14}H_{38}O_{12}Si_7$	FW 595.04
	Solvent Solubility	tetrahydrofuran, chloroform
	Solvent Insolubility	water, acetonitrile
	Appearance	white powder
	Uses	surface modification (dispersant), additive to thermoplastics and thermoset polymers for improving moisture resistance and processability
		50g/\$480 100g/\$640

Figure 4-5. POSS® SO1444 (From www.hybridplastics.com)

TetraSilanolPhenyl POSS®		SO1460
	$C_{48}H_{44}O_{14}Si_8$	FW 1069.54
	Solvent Solubility	tetrahydrofuran, acetone, ethylacetate
	Solvent Insolubility	methanol, ethanol, water, acetonitrile, chloroform
	Resin Solubility	most aliphatic and aromatic monomers, oligomers, polymers, PP, PE, PA, PET, PC
	Appearance	white crystalline solid
	Uses	processing aid, surface modification, modulus retainment, cure promotion in epoxy, BMI
		50g/\$480 100g/\$640

Figure 4-6. POSS® SO1460 (From www.hybridplastics.com)

4.3.1.2 Filters

Glass fiber filters from Pall (Type A/E, 1 μ m average pore size, 47-mm diameter, Cat #61631) were used to filter uranyl acetate solutions in the preparation of uranyl perchlorate. Hydrophilic alumina oxide filters from Whatman (Anodisc 25, Cat #6809-6022, 0.2 μ m average pore size, 25-mm diameter, with polypropylene support ring) and hydrophobic polytetrafluoroethylene (PTFE) filters from Millipore (Fluoropore, Cat #FHL P02500, 0.5 μ m pore size, 25-mm diameter, with polyethylene support) were used to prepare solid and residue samples.

4.3.1.3 pH Measurements

The pH of aqueous solutions was measured with an Orion Triode™ 9107BN pH probe and Orion 720 meter from Thermo Scientific. The electrode was filled with 3 M potassium chloride, calibrated using four aqueous buffers, and included automatic temperature correction. The pH of alcohol solutions was measured with a Solvotrode pH electrode, 799 GPT Titrino meter, and Tiamo software (Version 1.1) from Metrohm®. The electrode was filled with saturated LiCl in EtOH, calibrated using four aqueous buffers (pH 1.00 from VWR and pH 4.01, 7.00, and 10.01 from Thermo Scientific) and the laboratory temperature recorded at the time of pH measurement. Ethanol-based buffers were not available. Measurement of pH is used only as a qualitative indicator of changing solution conditions and therefore EtOH-based sample pH results were not corrected for the use of aqueous buffers.

4.3.1.4 UV-Visible Absorption Spectrometry

Absorbance was measured on a Cary 6000i UV-Vis-NIR spectrometer using four-sided, 10-mm pathlength cuvettes made of either PMMA or glass. All EtOH-based samples were measured in glass cuvettes with PTFE stoppers (Precision Cells, Type 23G10) to inhibit evaporation. Glass cuvettes were triple rinsed with 25% HNO₃ solution, rinsed with acetone, and dried in an oven at 80 °C for one hour between uses. Measurements were made in air using double-beam mode and 600 nm/min scan rate from 800 nm to 200 nm without baseline correction. A temperature-controlled sample block maintained each cell at either 22 or 25 °C, as indicated.

4.3.1.5 Inductively Coupled Plasma-Atomic Emission Spectrometry

The iron concentration of a prepared iron perchlorate stock solution (§4.3.2.2) was determined by Inductively Coupled Plasma-Atomic Emission Spectrometry (ICP-AES) (Thermo iCAP 6000 series). A calibration curve was generated using a gravimetrically-prepared FeCl_3 standard and subsequent volumetric dilutions. A 1% HNO_3 solution was used as a diluent for the standards and samples and for rinses between measurements.

4.3.1.6 Laser Fluorescence Intensity Measurements

The laser fluorescence system consists of a Q-switched, neodymium-doped yttrium aluminum garnet (Nd:YAG) pulsed laser (Quantel Brilliant, 10 Hz), spectrograph (Princeton Instruments Acton SP2500i), and CCD camera with pulser (Princeton Instruments PI-MAX Model 7397-0021 and Programmable Timing Generator™ Model 7513-0001). The laser beam was focused through a beamsplitter (R8% T92%, Thorlabs, Cat #BP108) and the reflected pulse energy monitored on a pyroelectric energy meter (Ophir Model PE25-SH-V2 and Nova II display, Cat #1Z01550). The laser was tuned with an Optical Parametric Oscillator and its harmonics adjusted manually (targeted at 2 mJ reflected energy). The spectrograph was calibrated at 411 nm (150 groove grating, center wavelength of 550 nm at pixel 512.5). System performance was verified using an Ovalene fluorescence reference (Starna Scientific Cat #6BF) excited at 422 nm. Ovalene exhibits a sharp and intense emission peak at 482 nm (Figure 4-7) which can be used as verification of the spectrograph calibration.

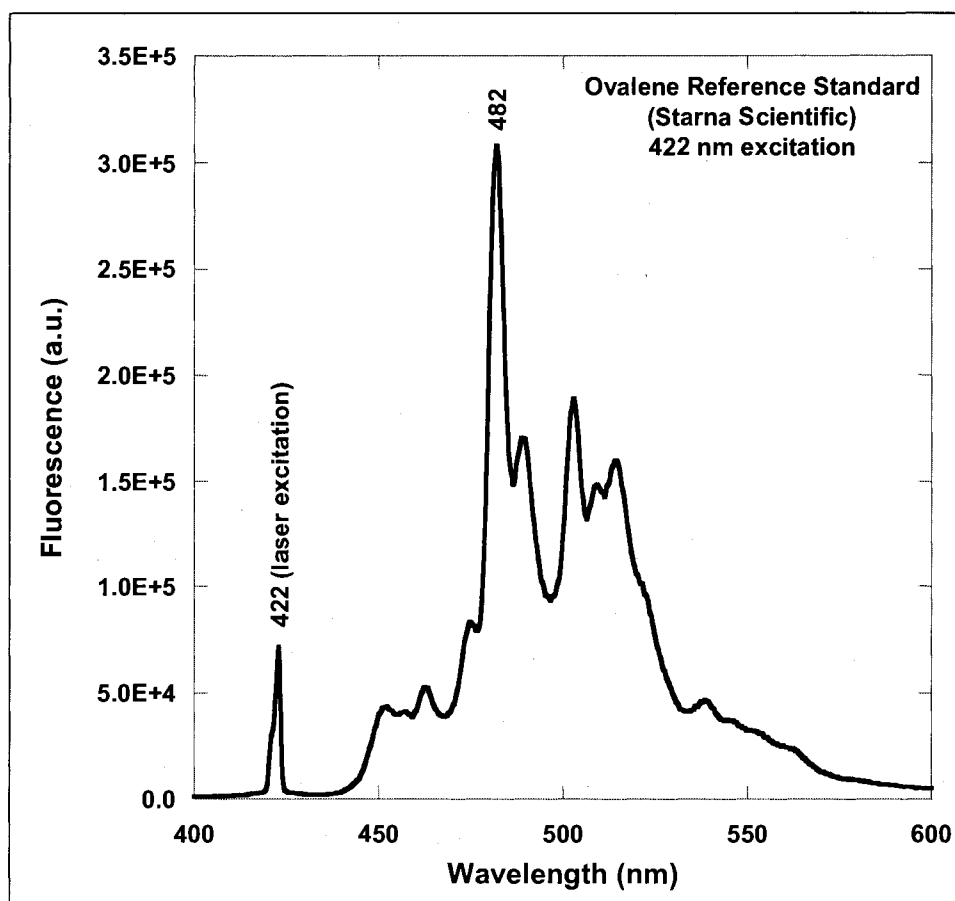


Figure 4-7. Fluorescence of ovalene reference standard.

Solution samples were measured in four-sided, stoppered glass cuvettes at room temperature or cooled to 22 °C in a temperature-controlled stage of an UV-vis spectrometer. Solid and residue samples¹, mounted on microscope slides, were measured in a slide holder at room temperature. Samples were placed in a sample chamber (Acton Research Model SC447) and the induced fluorescence detected at 90° to the laser path (Figure 4-8) through a manually-adjusted entrance slit to the spectrograph (Figure 4-9). For solution samples, the width of the spectrograph entrance slit was adjusted to 500 μm such that the measured fluorescence intensity of an aqueous 4.8 mM uranyl perchlorate

¹ 'Solid samples' are the dried deposits of aqueous solution samples on inorganic filters. 'Residue samples' are the vacuum filtered and dried products of contacting ethanol-based solutions with solid samples.

solution was approximately 75% that of detector saturation. For solids and residues, the width of the spectrometer entrance slit was adjusted to 25 μm such that the measured fluorescence intensity of a 0.048 μmol uranyl perchlorate solid was approximately 75% that of detector saturation. Spectrograph, pulser, and camera operations were controlled using Winspec/32 software (Roper Scientific, Version 2.5.21.0).

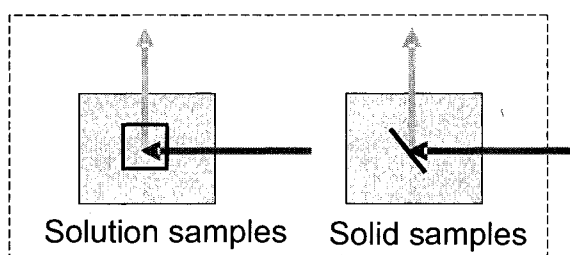


Figure 4-8. Variation in sample chamber configuration for solution versus solid/residue samples.

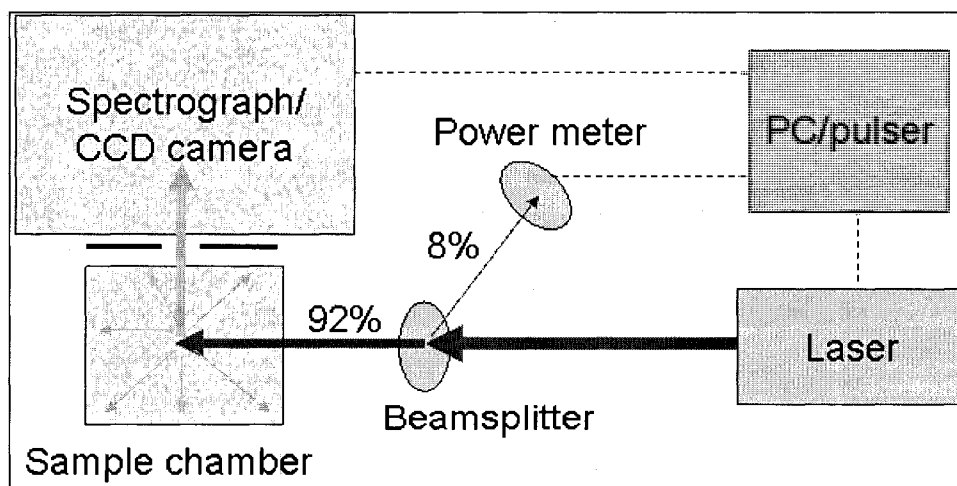


Figure 4-9. Configuration of laser-induced fluorescence system.

Laser-induced fluorescence intensity was measured between 375 nm and 725 nm beginning at 0.2 μ s after pulse initiation using a gate width of 10 ms. Intensities were summed for 10 pulses for each of 50 recorded spectra (Figure 4-10) and pulse energies were averaged and recorded per pulse. Both were converted to comma-separated value text files and the latter multiplied by a factor of 92%/8% to account for the beamsplitter. Each intensity value was divided by the mean pulse energy and by the number of pulses. The normalized spectra were then averaged to produce a mean spectrum for each sample plotted as fluorescence intensity per mJ per pulse as a function of wavelength.

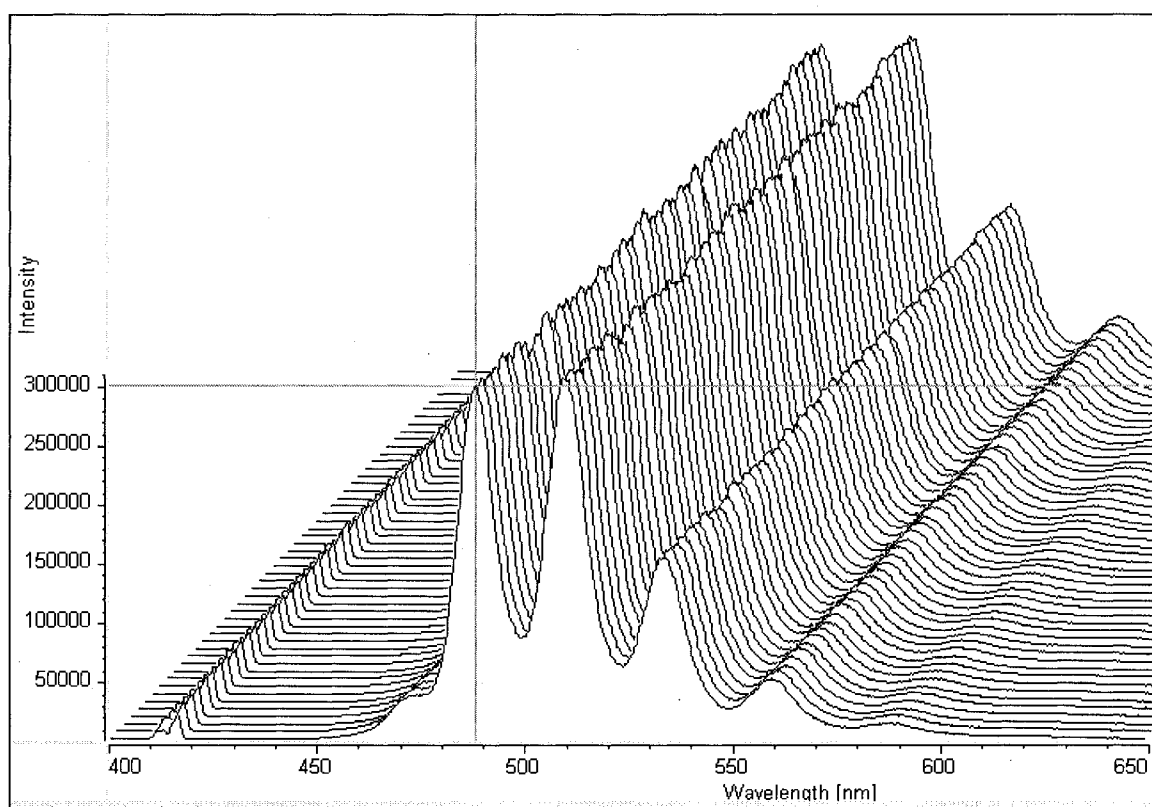


Figure 4-10. Example of fluorescence collected in pulser 'repetitive' mode (10 accumulations summed for each of 50 spectra measured).

The solution intensity spectra in Figure 4-11 were collected while determining the slit width that would not saturate the detector for various concentrations of uranyl in solution (§4.3.1.6). Even though they result from a uranyl concentration 10-fold greater than that used in this work, they illustrate that the peak maxima are not shifted as the slit width varies. Similar data for solid and residue samples are red-shifted 6 nm (see §4.4.1.1 for discussion) but do not vary with slit width.

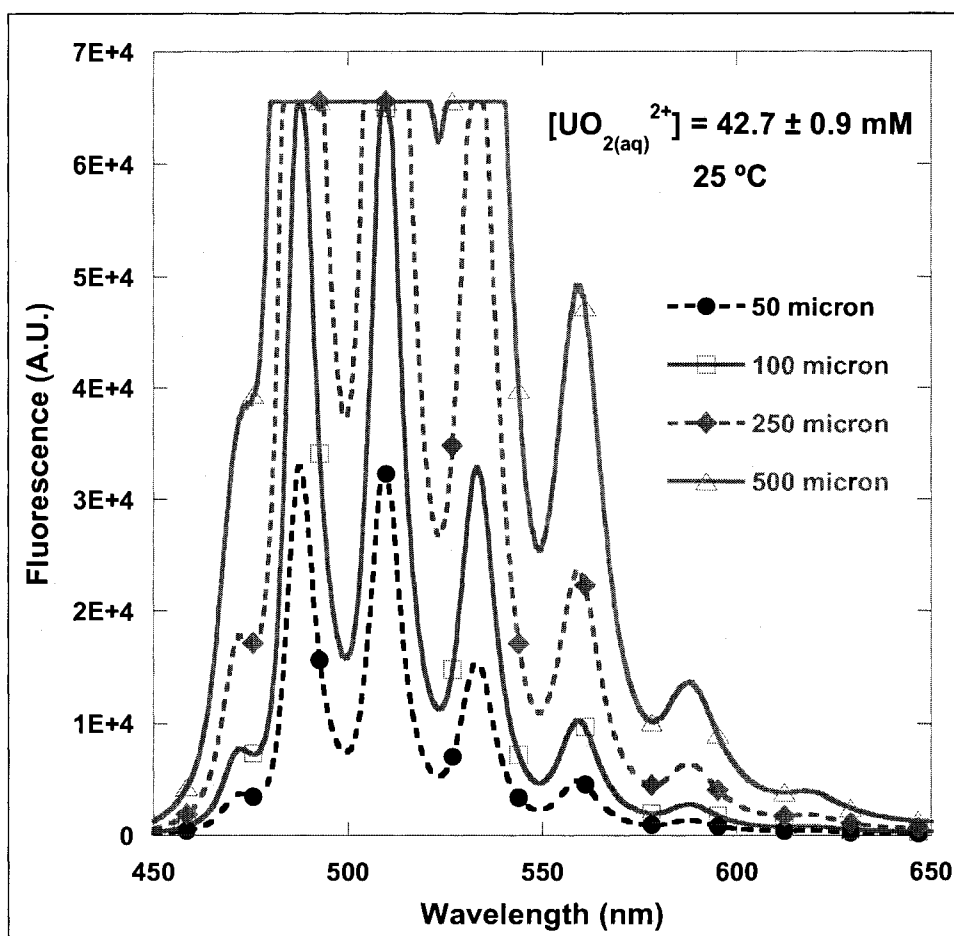


Figure 4-11. Effect of varying spectrograph entrance slit width on fluorescence intensity of 42.7 mM $\text{UO}_2(\text{ClO}_4)_2$ solution.

To compare fluorescence among solid and residue samples, the intensities of each mean spectrum were summed between 450.0 nm and 650.8 nm and the total background of the blank subtracted. The intensity ratio for a given sample, I_o/I , was calculated using the summed net intensity of a 0.048 μmol $\text{UO}_2(\text{ClO}_4)_2$ solid sample as I_o .

4.3.1.7 Laser Fluorescence Lifetime Measurements

Lifetime measurements were performed using time-resolved laser fluorescence spectroscopy (TRLFS) with the system described in §4.3.1.6. The pulser was changed to sequential mode, with a gate width of 1 ms and gate delay end times (pulser delays) ranging from 1 μs to 600 μs , depending on the sample (Figure 4-12). Data were collected and normalized as described for fluorescence intensity measurements.

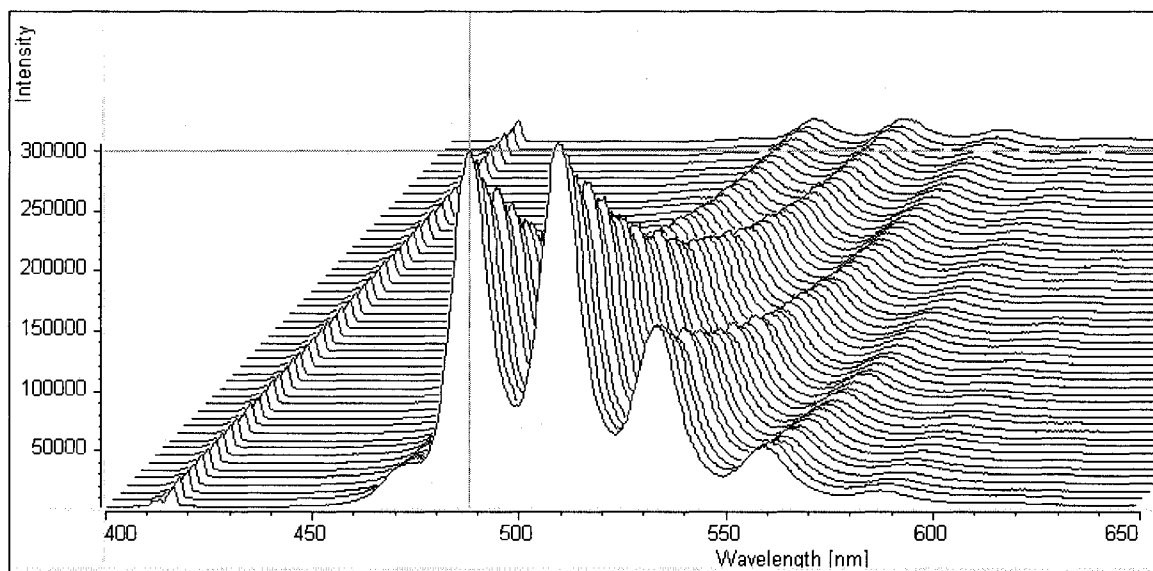


Figure 4-12. Example of fluorescence collected in pulser 'sequential' mode (10 accumulations summed for each of 50 spectra measured)

To calculate the fluorescence lifetime of samples, the gross intensities for each measured spectrum were summed between 450.0 nm and 650.8 nm and plotted as a

function of gate delay end time (pulser delay). Background was constant for each spectrum and was not subtracted from the summed intensities. The summed fluorescence intensities were iteratively fit using a single-component, exponential decay function in KaleidaGraph (Synergy Software, Version 4.03) until the parameters converged with minimal χ^2 values and maximum R^2 values. The inverse of the resulting exponential coefficient is the fluorescence lifetime for the sample (Figure 4-13). In the presented experiments the lifetime, τ , was measured in μs .

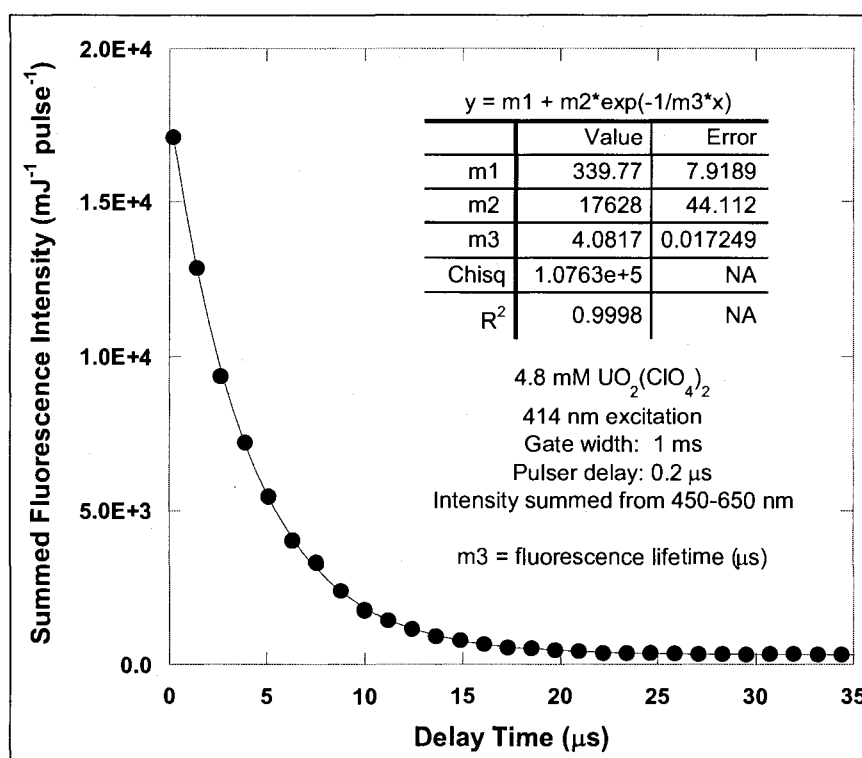


Figure 4-13. Example of monoexponential fit of summed fluorescence intensity for increasing pulser delay times.

4.3.2 Stock Solution Preparation

4.3.2.1 Uranyl Perchlorate Solution

Aqueous $\text{UO}_2(\text{ClO}_4)_2$ was prepared by dissolving 106.05 g UAc in 1675 mL of DI water and filtering the solution through 1 μm glass fiber filters. The filtrate was placed in 50-mL polypropylene centrifuge tubes (45-mL aliquots each) and uranyl hydroxides precipitated with 4 mL 10 M NaOH each (prepared in DI water using NaOH pellets). Each tube was mixed by vortex, centrifuged at 3000 rpm for five minutes (Eppendorf Centrifuge 5804), and the supernatants decanted. The precipitates were dried in the tubes for approximately 15 hours at 80 $^\circ\text{C}$, redissolved in 60% HClO_4 , and diluted volumetrically 30-fold with DI water for use as a uranyl perchlorate stock solution. The $\text{UO}_2(\text{ClO}_4)_2$ stock solution pH measured 0.6 at room temperature. A diluent was prepared for future sample preparations by adjusting DI water with HClO_4 until its pH measured 0.6.

The unknown UO_2^{2+} concentration of the uranyl perchlorate stock solution was determined by UV-Vis at 25 $^\circ\text{C}$ in PMMA cuvettes (Cary 6000i in double-beam mode without baseline correction). The background of the diluent in a PMMA cuvette was subtracted before concentration calculations. The fluorescence intensities and lifetimes of a 4.8 mM UO_2^{2+} solution and of a 0.048 μmol UO_2^{2+} solid sample were measured to compare to the published literature.

4.3.2.2 Iron(III) Perchlorate Solution

$\text{Fe(III)(ClO}_4)_3 \cdot x\text{H}_2\text{O}$ crystals are very hygroscopic and as such the molecular weight is reported on an anhydrous basis. A high concentration parent solution was prepared by

dissolving 30.33 g $\text{Fe(III)(ClO}_4)_3 \cdot x\text{H}_2\text{O}$ in DI water, made up to 50 mL, and estimated to be 1700 mM Fe^{3+} .

The unknown Fe^{3+} concentration was determined by ICP-AES. Aqueous FeCl_3 standards were prepared by dissolving 3.379 g $\text{FeCl}_3 \cdot 6\text{H}_2\text{O}$ in DI water, made up to 50 mL, and diluting volumetrically with 1% HNO_3 solution to create 0.5, 1, 2.5 and 5 mM Fe^{3+} standards. The $\text{Fe(ClO}_4)_3$ parent solution was diluted volumetrically with 1% HNO_3 solution to create < 425 mM and < 248.2 mM solutions and these were further diluted 100-fold with 1% HNO_3 solution for analysis. A blank of 1% HNO_3 and each of the FeCl_3 standards were used to generate a calibration curve for Fe^{3+} prior to analysis of each $\text{Fe(ClO}_4)_3$ sample. The $\text{Fe(ClO}_4)_3$ stock solution pH measured < 1 at room temperature (calibration slope = 99.1% with pH 1.00, 2.00, 3.00 and 4.00 buffers).

4.3.2.3 Ethanol Solutions

AMP- and TEA-buffered EtOH solutions were prepared by diluting the viscous buffers (Table 4-2) to 500 mM with EtOH. The EtOH and buffered-EtOH solutions were stored in sealed, glass bottles with 1 g zeolite beads per 100 mL between uses to minimize water absorption. The initial AMP stock solution pH measured 10.9 at 20.8 °C (calibration slope = 99.4% with pH 4.01, 7.00 and 10.01 buffers). The initial TEA stock solution pH measured 9.7 at 22.5 °C (calibration slope = 99.4% with pH 4.01, 7.00 and 10.01 buffers). Concentrated HNO_3 was diluted with EtOH to 500 mM for adjusting the pH of the EtOH-based solutions prior to POSS[®] addition.

4.3.3 Sample Preparation²

4.3.3.1 Aqueous Solution Samples

Aqueous uranyl - iron(III) solution samples were prepared by combining $\text{UO}_2(\text{ClO}_4)_2$ and $\text{Fe(III)(ClO}_4)_3$ stock solutions volumetrically in glass scintillation vials as shown in Table 4-3. Within this series, solution samples contained a constant 4.8 mM UO_2^{2+} concentration and an increasing Fe^{3+} concentration from 0 mM to 85 mM.

Table 4-3. Composition of aqueous solution samples.
 $[\text{UO}_2^{2+}]_{\text{stock}} = 9.6 \text{ mM}$; $[\text{Fe}^{3+}]_{\text{stock}} = 850 \text{ mM}$

Sample #	Solutions				
	$\text{UO}_2(\text{ClO}_4)_2$ stock (mL)	$[\text{UO}_2^{2+}]$ in 5 mL (mM)	$\text{Fe}(\text{ClO}_4)_3$ stock (mL)	$[\text{Fe}^{3+}]$ in 5 mL (mM)	Diluent (mL)
VF-1	2.50	4.80	0.00	0.0	2.50
VF-2	2.50	4.80	0.01	1.7	2.49
VF-3	2.50	4.80	0.05	8.5	2.45
VF-4	2.50	4.80	0.10	17.0	2.40
VF-5	2.50	4.80	0.25	42.5	2.25
VF-6	2.50	4.80	0.50	85.0	2.00
VF-7	2.50	4.80	1.00	170.0	1.50

4.3.3.2 POSS[®] Solution Samples

POSS[®] SO1444 and POSS[®] SO1460Na ligands were dissolved in EtOH and buffered-EtOH solutions (§4.3.2.3). Since POSS[®] decomposes in basic environments³, the buffered alcohols were adjusted with 500 mM HNO_3 in EtOH such that the final pH following ligand addition would measure 9.4 for AMP-based solutions and 7.8 for TEA-based solutions. These target pH values were chosen based on the pK_a values of the buffers. The required acid volume was determined through a series of acid or ligand

² 'Solid samples' are the dried deposits of aqueous solution samples on inorganic filters. 'Residue samples' are the vacuum filtered and dried products of contacting ethanol-based solutions with solid samples.

³ Joseph Schwab, Hybrid Plastics, personal communication (December 2007).

titrations and verified through batch dissolutions. The intended POSS[®] concentration for each ligand solution was 20 mM to provide excess ligand relative to the uranyl concentration. Volume increases resulting from solid dissolution and from the acid additions were calculated to be less than 2% and therefore POSS[®] concentrations are referred to as 20 mM without correction. The resulting sample compositions of EtOH and buffered-EtOH solutions, with and without POSS[®], are outlined in Table 4-4. Each solution pH was measured as described in §4.3.1.3.

Table 4-4. Composition of EtOH-based solution samples.

Sample	EtOH (mL)	AMP-EtOH (mL)	TEA-EtOH (mL)	500 mM HNO ₃ in EtOH (μL)	POSS 1444 (mg)	POSS 1460N (mg)
EtOH	10					
AMP-EtOH		10				
AMP-EtOH-HNO ₃		10		90		
TEA-EtOH			10			
TEA-EtOH-HNO ₃			10	20		
EtOH-POSS1444	10				119	
AMP-EtOH-POSS1444		10			119	
AMP-EtOH-HNO ₃ -POSS1444		10		90	119	
AMP-EtOH-HNO ₃ -POSS1460Na		10		150		248.5
TEA-EtOH-POSS1444			10		119	
TEA-EtOH-HNO ₃ -POSS1444			10	20	119	

4.3.3.3 Solid Samples

Uranyl solid samples were prepared by depositing 10 μL of 4.8 mM UO₂(ClO₄)₂ stock solution onto a hydrophilic inorganic filter, located in between a stainless steel washer and a hydrophobic filter. The washer kept the filters flat and provided an opening through which to deposit the solution on the top filter. The hydrophobic filter prevented solution breakthrough that would have otherwise resulted in mass loss of the sample. The assembly was dried in an oven (Hybaid Mini Oven MkII) for 2 hours at 50 °C and

the solid sample removed. Each uranyl solid sample therefore contained 0.048 μmol UO_2^{2+} . Similarly, uranyl–iron(III) solid samples were prepared by depositing 10 μL of each aqueous solution sample (§4.3.3.1) onto an inorganic filter as before. Each uranyl–iron(III) solid sample therefore contained a constant 0.048 μmol UO_2^{2+} with Fe^{3+} ranging from 0 μmol to 0.85 μmol (Table 4-5). The fluorescence intensity of each solid was measured as described in §4.3.1.6. The constant amount of Fe^{3+} used in experiments with POSS[®] was chosen based on the amount of fluorescence intensity quenching measured in the uranyl–iron(III) solid samples.

Table 4-5. Composition of solid samples.

Sample #	Solids	
	UO_2^{2+} in 10 μL (μmol)	Fe^{3+} in 10 μL (μmol)
VF-1	0.048	0.000
VF-2	0.048	0.017
VF-3	0.048	0.085
VF-4	0.048	0.170
VF-5	0.048	0.425
VF-6	0.048	0.850

4.3.3.4 Residue Samples

Residue samples were prepared by contacting an EtOH-based solution with a solid sample. Solution listed in Table 4-4 were contacted with both a uranyl solid sample (0.048 μmol UO_2^{2+}) and a uranyl–iron(III) solid sample (0.048 μmol UO_2^{2+} and 0.425 μmol Fe^{3+}), resulting in a total of 22 residue samples prepared as follows.

Prepared solid samples, of either uranyl or uranyl–iron(III), were mounted on the support screens of a vacuum filtration manifold (Millipore Model 1225, Cat #M2536). Centrifuge tubes were loaded to collect filtrates and the apparatus assembled as shown in Figure 4-14. Aliquots (3 mL) of each EtOH-based solution sample from Table 4-4 were deposited in the sample cups onto the solid samples with a pipettor and each cup covered with a rubber stopper to inhibit evaporation.

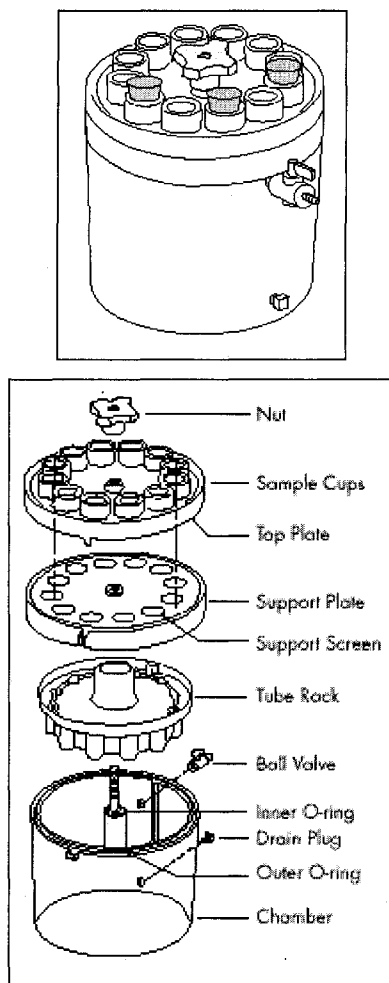


Figure 4-14. Millipore 1225 vacuum filtration manifold (From www.millipore.com)

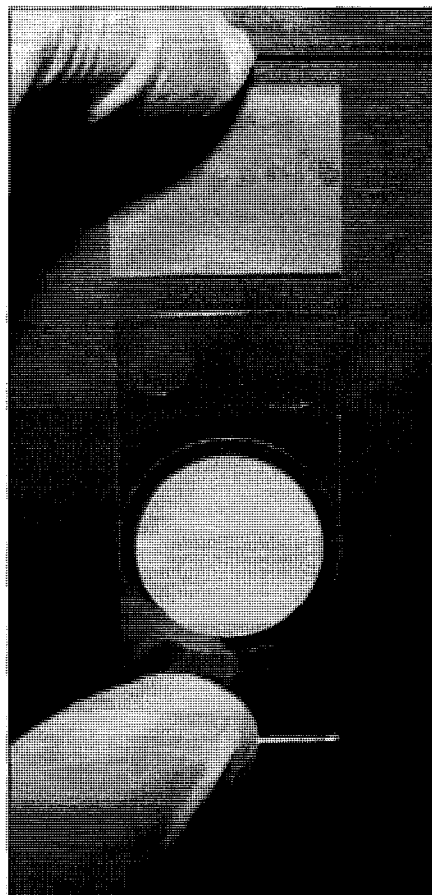


Figure 4-15. Example of solid or residue sample on inorganic filter, mounted on microscope slide, and secured with coverslip.

Following a 30-minute contact, vacuum was applied for 5 minutes (Dryfast Model 2012B-01, 22 L/min) and the filtrates collected. The residue samples were dried (2 hours at 50 °C) and mounted on microscope slides. A template slide was placed underneath to ensure the sample residue would be centered within the laser spot and a square glass coverslip secured over the filter to the underlying slide with cyanoacrylate cement (Figure 4-15).

The fluorescence intensity and lifetime of each residue sample was measured as described in §4.3.1.6 and §4.3.1.7, respectively, to determine the effects of the EtOH,

buffers, HNO_3 , and POSS[®] on the uranyl fluorescence, in both the absence and presence of iron. The pH and fluorescence intensity of each filtrate was measured to indicate if uranyl was being redissolved in the applied EtOH-based solution and lost into the filtrate.

4.4 Results and Discussion

4.4.1 Stock Solution Characterization

4.4.1.1 Uranyl Perchlorate Solution

The uranyl perchlorate stock solution concentration was determined by UV-vis. Using a molar absorptivity of $9.7 \pm 0.2 \text{ L mol}^{-1} \text{ cm}^{-1}$ for the free uranyl ion ($\text{pH} < 3$) at the maximum absorbance peak of 414 nm (Meinrath, 1997) resulted in UO_2^{2+} concentrations of $9.58 \pm 0.94 \text{ mM}$ for the stock solution and $289.57 \pm 5.97 \text{ mM}$ for the parent solution. Aqueous solution samples for experiments were prepared using a 2-fold dilution of the stock solution with diluent for a constant concentration of 4.8 mM UO_2^{2+} . The absorption spectrum of the $4.8 \text{ mM UO}_2(\text{ClO}_4)_2$ solution is presented in Figure 4-16 and its fluorescence spectrum in Figure 4-17. The wavelength of each measured absorption and emission maximum corresponds within 1-2 nm of those published for free uranyl (Bell and Biggers, 1965; Gunther et al., 2007; Meinrath, 1998). The locations of the maxima are dependent on pH and are consistent with those listed for pH 1 uranyl solutions in Table 4-1.

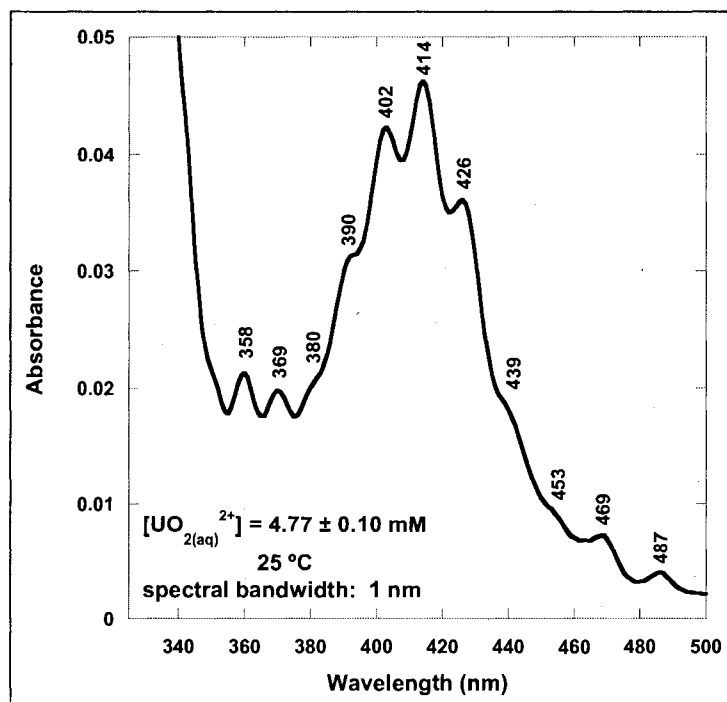


Figure 4-16. UV-Vis absorbance of aqueous 4.8 mM $\text{UO}_2(\text{ClO}_4)_2$.

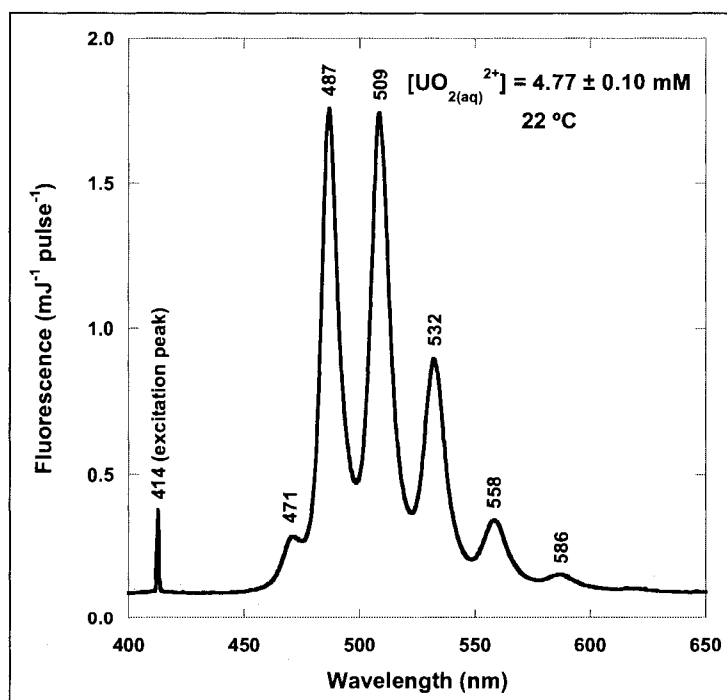


Figure 4-17. Laser-induced fluorescence of aqueous 4.8 mM $\text{UO}_2(\text{ClO}_4)_2$.

The monoexponential fit of the aqueous 4.8 mM $\text{UO}_2(\text{ClO}_4)_2$ solution fluorescence decay and the calculated lifetime are provided in Figure 4-18. The calculated lifetime of $4.08 \pm 0.02 \mu\text{s}$ ($R^2 = 1$) at pH = 0.6 and 23 °C is very consistent with similar conditions in a perchlorate environment (Bouby et al., 1999).

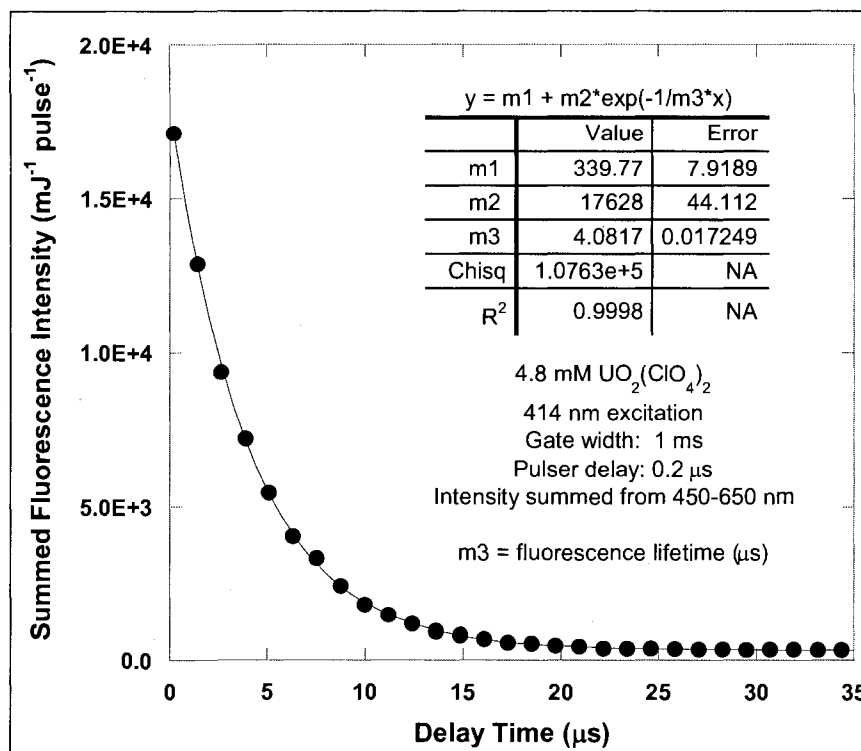


Figure 4-18. Monoexponential fit of summed fluorescence intensity for aqueous 4.8 mM $\text{UO}_2(\text{ClO}_4)_2$ solution as a function of increasing pulser delay times. The fitted value of m3 is the UO_2^{2+} lifetime (μs).

4.4.1.2 Iron(III) Perchlorate

The $\text{Fe}(\text{ClO}_4)_3$ dilutions were determined to have concentrations of 343 mM and 146 mM Fe^{3+} , respectively, and by extrapolation the $\text{Fe}(\text{ClO}_4)_3$ parent solution concentration was 850 mM Fe^{3+} . The $\text{Fe}(\text{ClO}_4)_3$ stock solution pH measured <1 at room temperature.

4.4.2 Effect of Iron on Uranyl Fluorescence

4.4.2.1 Solid Sample Fluorescence Intensity Measurements

A co-plot of the fluorescence spectra for the 4.8 mM UO_2^{2+} solution and the corresponding 0.048 μmol UO_2^{2+} solid sample highlights a consistent red-shift in the spectrum of the solid (Figure 4-19). Each of the characteristic free uranyl fluorescence maxima appear at a 6 nm greater wavelength in the solid than in the solution. As the deposited solution dries, water preferentially coordinates uranyl over the perchlorate, resulting in complexed hydrolysis species similar to those that would be formed in solution by increasing the pH. The shift in spectrum is similar to that of a pH 5 – 8.5 solution environment; however, the speciation in the solid would need to be determined using spectral deconvolution or time resolution (Moulin et al. 1995).

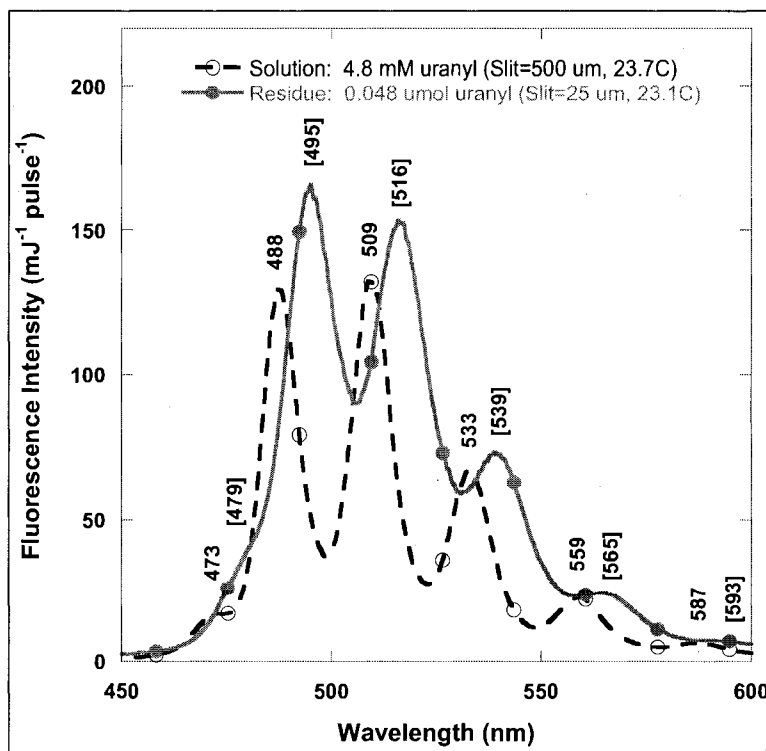


Figure 4-19. Fluorescence intensities of solution (4.8 mM UO_2^{2+}) and solid (0.048 μmol UO_2^{2+}) samples.

Net fluorescence intensities, summed between 450 nm and 650 nm, are listed in Table 4-6 for both uranyl solution and solid samples. The ratio I_o/I for each sample was calculated using the summed net intensity of the sample with no iron as I_o . This ratio increases linearly with increasing $[\text{Fe}^{3+}]$ for solutions (slope = 0.002, $R^2 = 1$) and for solids (slope = 8.7, $R^2 = 0.999$).

Table 4-6. Summary of summed net fluorescence intensities for constant uranyl solution (4.8 mM UO_2^{2+}) and solid (0.048 μmol UO_2^{2+}) samples with increasing Fe^{3+} .

Solutions			Residues		
$[\text{Fe}^{3+}]$, mM	Sum 450-650 nm	I_o/I	Fe^{3+} , μmol	Sum 450-650 nm	I_o/I
0.0	15540	1.000	0.000	21403	1.000
1.7	15277	1.017	0.017	18906	1.132
8.5	15247	1.019	0.085	11567	1.850
17.0	14943	1.040	0.170	9114	2.348
42.5	14175	1.096	0.425	4595	4.657
85.0	12120	1.282	0.850	2541	8.424

When $I_o/I = 4$, the baseline sample fluorescence is quenched by 75%. For experiments with POSS[®] in the presence of iron, the solid samples containing 0.048 μmol UO_2^{2+} and 0.425 μmol Fe^{3+} were used since they were the only samples that quenched near 75% (Figure 4-20). This diminished intensity allowed observation of any fluorescence enhancement or any additional quenching resulting from the POSS[®].

4.4.2.2 Solid Sample Fluorescence Lifetime Measurements

The calculated monoexponential lifetimes for the aqueous samples used in work, and the solid samples prepared from them, are listed in Table 4-7 with their associated lifetime quenching ratios, τ_o/τ . The ratio τ_o/τ for each sample was calculated using the lifetime of the sample with no iron as τ_o .

Table 4-7. Lifetimes and quenching effects for aqueous solution samples compared to their solid samples.

Sample	Sample Lifetime (μs)	τ_o/τ
Solution: 48 mM UO_2^{2+}	4.08 ± 0.02 ($R^2=1$)	1.00
Solution: 48 mM UO_2^{2+} and 42.5 mM Fe^{3+}	3.73 ± 0.03 ($R^2=0.999$)	1.09
Solid: 0.048 μmol UO_2^{2+}	225 ± 2 ($R^2=0.999$)	1.00
Solid: 0.048 μmol UO_2^{2+} and 0.425 μmol Fe^{3+}	124 ± 5 ($R^2=0.9826$)	1.81

The reduction in both fluorescence intensity and lifetime in the presence of iron results from the high excess of iron to uranyl. Electron transfer in the interaction of Fe^{3+} and the excited uranyl, $(\text{UO}_2^{2+})^*$ occurs very effectively, especially as the solution dries and the distances between ions and their ability to reorient relative to each other decreases. In solutions, $I_o/I = \tau_o/\tau$ indicating fluorescence is dynamically quenches as expected. In solids, processes related to thermal agitation (collisions with solvent molecules, intramolecular

vibrations and rotations, etc) are minimized and so is the contribution of dynamic quenching. The interaction of UO_2^{2+} and Fe^{3+} ions should therefore result only in static quenching and decreased intensity, without an

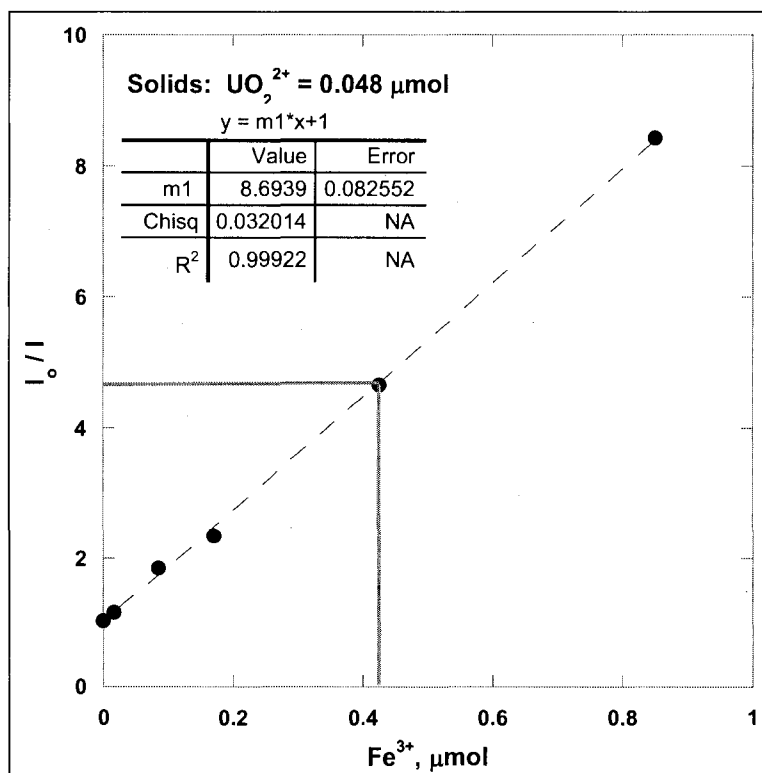


Figure 4-20. Fluorescence intensity ratios for constant uranyl perchlorate solids (0.048 μmol UO_2^{2+}) with increasing Fe^{3+} .

accompanying decrease in lifetime. The inequality between I_o/I and τ_o/τ for the solid samples does indicate static quenching, with τ_o/τ greater than unity due to some residual water and therefore small dynamic quenching within the sample.

4.4.3 Effect of POSS[®] on Uranyl Fluorescence

The use of POSS[®] ligands in EtOH-based solutions were evaluated to baseline their effects on intensity (§4.4.3.2) and lifetime (§4.4.3.3) before iron is added to the samples in section §4.4.4. Recall that ‘solid samples’ are the dried deposits of aqueous solution samples on inorganic filters, ‘residue samples’ are the vacuum filtered and dried products of contacting ethanol-based solutions with solid samples, and the filtrates are collected EtOH-based solutions following contact and vacuum filtration. For the results presented and discussed in this section, the solid samples are 0.048 $\mu\text{mol UO}_2^{2+}$ on inorganic filters.

4.4.3.1 Solution and Filtrate pH Measurements

Table 4-8 lists the measured pH of the EtOH-based solutions as prepared and the collected filtrates following a 30 minute contact with solid 0.048 $\mu\text{mol UO}_2^{2+}$ samples.

Table 4-8. EtOH-based solution or filtrate pH at room temperature. Filtrates contacted 30-min with solid 0.048 $\mu\text{mol UO}_2^{2+}$ samples.

Sample	pH, solution	pH, filtrate
EtOH	8.1	0.4
EtOH + 20mM POSS1444	7.5	0.5
500mM AMP-EtOH	10.6	9.9
500mM AMP-EtOH + 20mM POSS1444	9.7	9.7
500mM AMP-EtOH-HNO ₃	9.5	9.5
500mM AMP-EtOH-HNO ₃ + 20mM POSS1444	9.4	9.4
500mM TEA-EtOH	9.3	8.0
500mM TEA-EtOH + 20mM POSS1444	8.5	7.5
500mM TEA-EtOH-HNO ₃	7.8	7.6
500mM TEA-EtOH-HNO ₃ + 20mM POSS1444	7.8	7.3
500mM AMP-EtOH-HNO ₃ + 20mM POSS1460Na	11.9	11.9

Measurement of pH was used only as a qualitative indicator of changing solution conditions. The solutions are well buffered, especially those with AMP, and significant pH change is only observed in the non-buffered solutions.

4.4.3.2 Filtrate and Residue Fluorescence Intensity Measurements

Net fluorescence intensities, summed between 450 and 650 nm, are listed in Table 4-9 for the residues and collected filtrates resulting from contacting each EtOH-based solution (see Table 4-4) with a solid 0.048 $\mu\text{mol UO}_2^{2+}$ sample. The ratio I_o/I for each sample was calculated using the summed net intensity of the solid 0.048 $\mu\text{mol UO}_2^{2+}$ sample as I_o .

Table 4-9. Summed net fluorescence intensities (I) for residues and filtrates of EtOH-based solutions contacted with solid 0.048 $\mu\text{mol UO}_2^{2+}$ samples.

Sample	Residue		Filtrate
	I	I_o/I	I
I_o : 0.048 $\mu\text{mol UO}_2^{2+}$	19961	1	45
EtOH	964	21	897
EtOH + 20mM POSS1444	1295	15	241
500mM AMP-EtOH	2207	9	261
500mM AMP-EtOH + 20mM POSS1444	1977	10	279
500mM AMP-EtOH-HNO ₃	2998	7	362
500mM AMP-EtOH-HNO ₃ + 20mM POSS1444	2029	10	134
500mM TEA-EtOH	798	25	113
500mM TEA-EtOH + 20mM POSS1444	601	33	41
500mM TEA-EtOH-HNO ₃	933	21	127
500mM TEA-EtOH-HNO ₃ + 20mM POSS1444	451	44	232
500mM AMP-EtOH-HNO ₃ + 20mM POSS1460Na	2055	10	274

Ideally, $I_o/I \rightarrow 1$ for the residues since $I_o = I$ indicates all of the UO_2^{2+} remained on the filter and its fluorescence was not quenched. Residue $I_o/I > 1$ indicates that the fluorescence of the residue is quenched or that UO_2^{2+} redissolved into the filtrate. The

nearly equal values of I for the EtOH residue and filtrate are due to dissolution of the original solid uranyl perchlorate into the EtOH. This conclusion is supported by the change in pH from 8.1 to 0.4 between the EtOH solution and the resulting filtrate. The addition of POSS[®] SO1444 to EtOH reduced the intensity observed in the filtrate; however, there was still uranyl dissolution into the solution as evidenced by the filtrate pH of 0.5.

Ethanol significantly quenches the residue fluorescence intensity as evidenced by all of the high I_o/I ratios. Even at higher uranyl and low EtOH concentrations than used here, Burrows and Formosinho (1978) reported $I_o/I \sim 1.3, 1.5,$ and 1.8 for $[\text{UO}_2^{2+}] = 10$ mM and $[\text{EtOH}] = 5, 10,$ and 15 mM, respectively, using uranyl nitrate hexahydrate solutions. The use of AMP buffers decreases the quenching effect of EtOH however the use of TEA buffers tend to increase quenching. The addition of POSS[®] has little effect on the resulting intensities for the residues from AMP-buffered solutions but increases quenching in those from TEA-buffered solutions. POSS[®] SO1460Na was included only to assess its potential for future studies and based on the results shown for POSS[®] SO1444, a single POSS[®] SO1460Na sample was prepared using the AMP-buffered EtOH adjusted with HNO_3 .

Fluorescence spectra of residues without POSS[®] are presented in Figure 4-21. Fluorescence exceeds background however; ‘dead’ pixels on the spectrograph give consistently lower responses at 506 and 550 nm. The locations of the maxima in the AMP-EtOH and AMP-EtOH- HNO_3 residue spectra are consistent with hydrolyzed uranyl similar to that reported for solutions with pH between 5 and 8.5 (Table 4-1). The broad spectra for the TEA-EtOH and TEA-EtOH- HNO_3 residues reflect a different combination

of species and are similar to those of solutions with pH values near 7. Additional measurements using varying gate widths and pulser delays are required for speciation based on the fluorescence spectra (Kirishima et al., 2005; Meinrath, 1997).

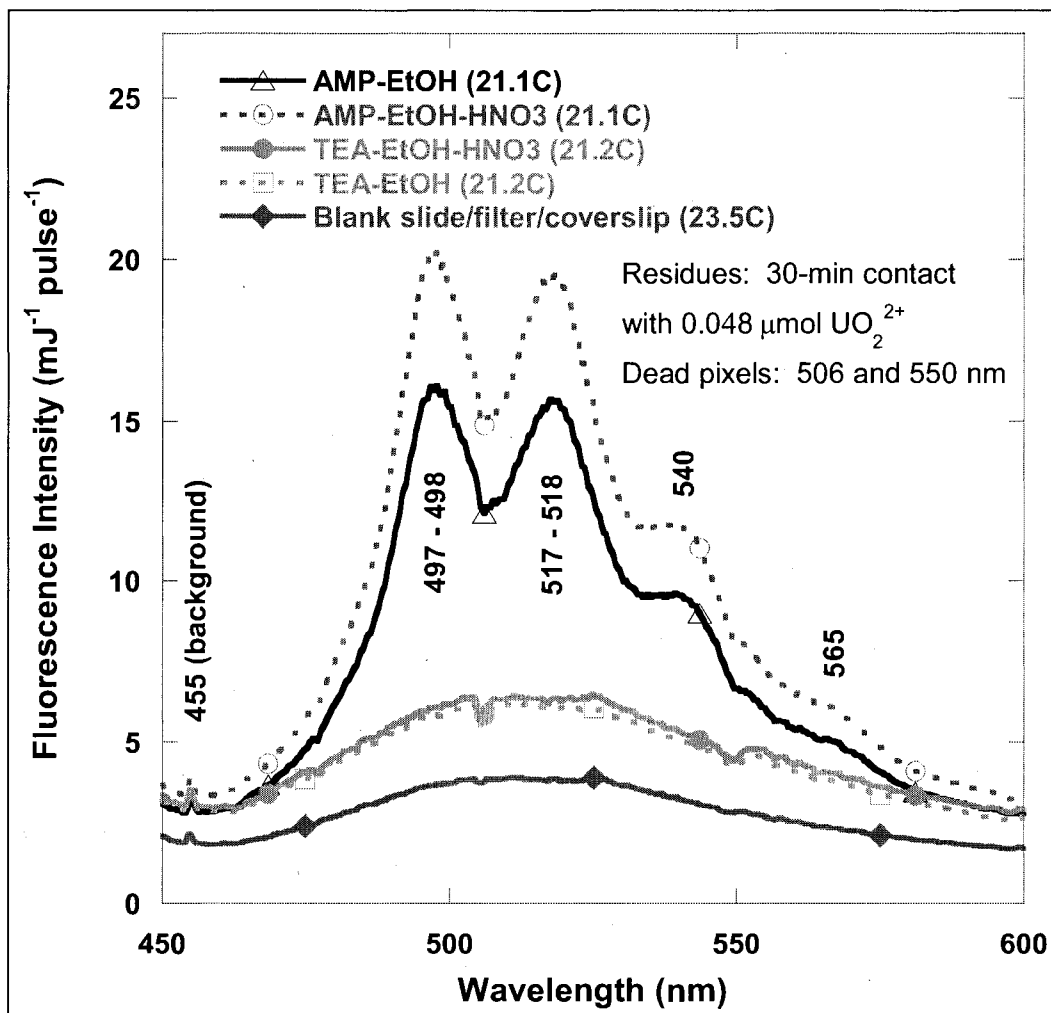


Figure 4-21. Residue fluorescence intensity of 0.048 $\mu\text{mol UO}_2^{2+}$ contacted with EtOH-based solutions. Measurement temperature ($^{\circ}\text{C}$) listed in legend.

Residue samples containing POSS[®] SO1444 (Figure 4-22) result in slightly less intense fluorescence emissions (higher I_o/I) than those without the ligand (Figure 4-21). The lack of change in the pH of the original solution, the peak locations in the residues,

or the pH of the collected filtrate indicate solution conditions have not changed upon POSS[®] SO1444 addition. The addition of POSS[®] SO1460Na to the solutions results in a residue spectral red-shift of approximately 10 nm consistent with the higher pH of 11.9 for the applied solution and indicates a higher degree of coordination than demonstrated without POSS[®] or with POSS[®] SO1444.

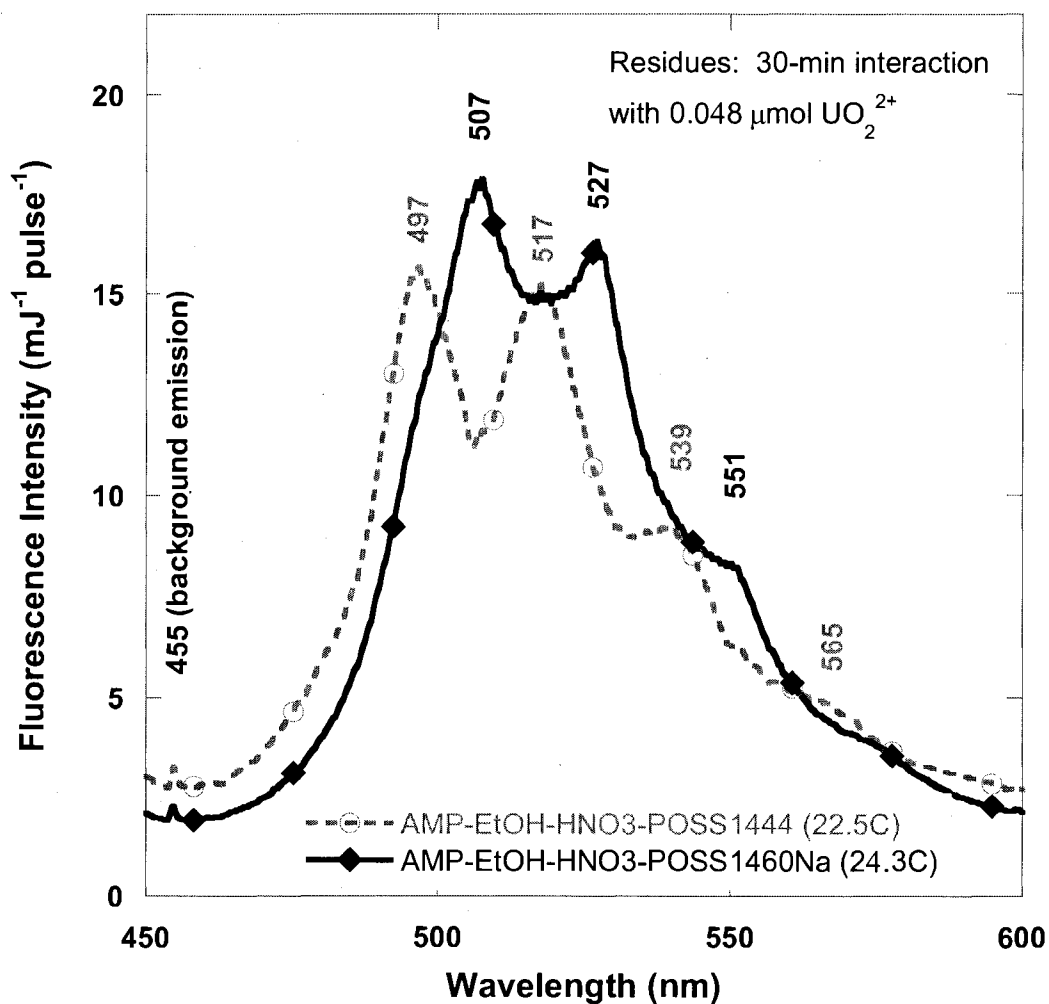


Figure 4-22. AMP-based residue fluorescence intensity with POSS[®] SO1444 and POSS[®] SO1460Na in the absence of iron. Measurement temperature (°C) listed in legend.

Comparison of the spectra for the residues yielding the highest intensities to the baseline spectrum of the solid $0.048 \mu\text{mol UO}_2^{2+}$ sample (Figure 4-23) highlight that the small intensity enhancements observed with POSS[®] cannot counter the significant quenching by EtOH. Under the system conditions investigated, the detection of residual surface uranyl may not be practical using fluorescence intensity measurements alone, even in the absence of iron, with and ethanol solvent.

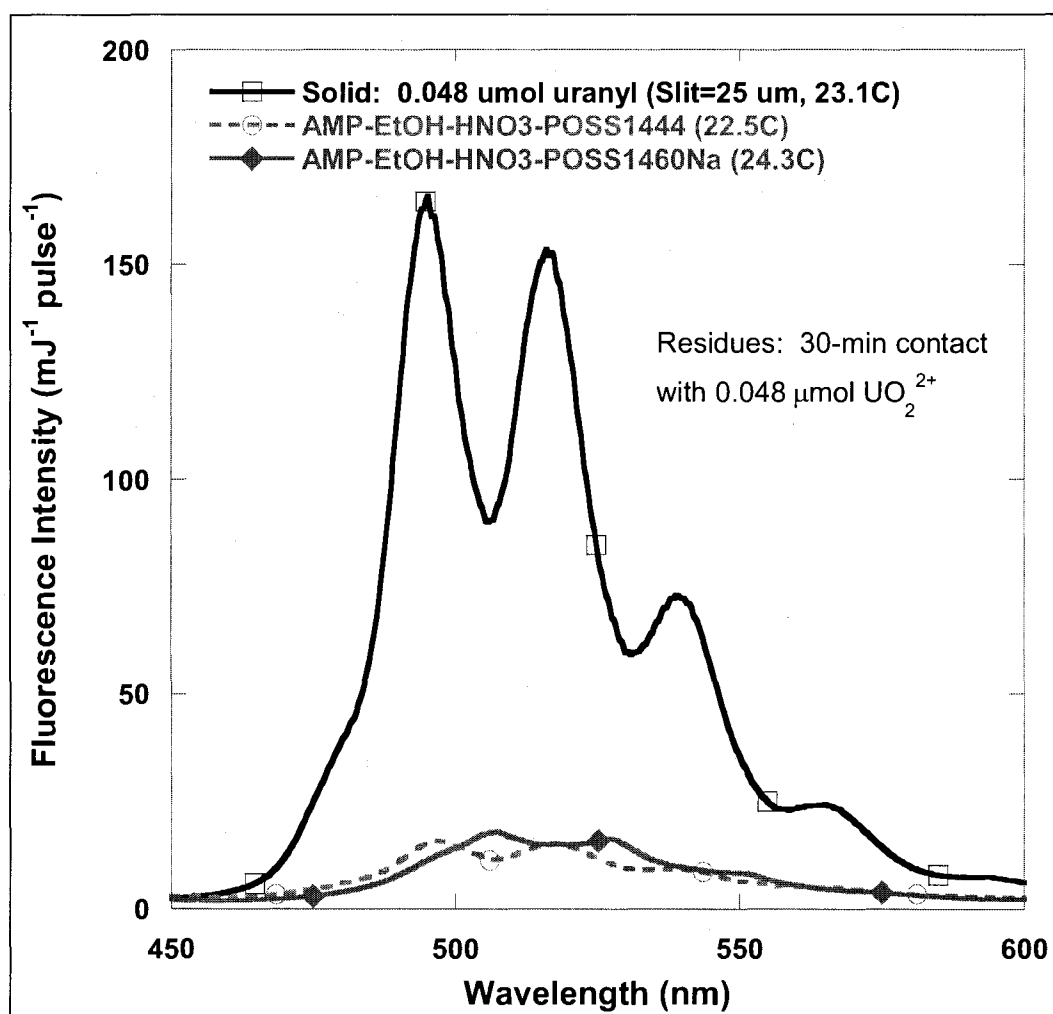


Figure 4-23. Comparison of fluorescence intensities of AMP-based residues with POSS[®] SO1444 and POSS[®] SO1460Na to solid $0.048 \mu\text{mol UO}_2^{2+}$. Measurement temperature ($^{\circ}\text{C}$) listed in legend.

4.4.3.3 Residue Fluorescence Lifetime Measurements

The calculated monoexponential lifetimes for the residues of EtOH-based solutions contacted with solid 0.048 $\mu\text{mol UO}_2^{2+}$ samples are listed in Table 4-10. The ratio τ_o/τ for each sample was calculated using the lifetime of the 0.048 $\mu\text{mol UO}_2^{2+}$ sample (225 μs) as τ_o .

Table 4-10. Residue fluorescence lifetimes (μs) in the absence of iron at room temperature. Monoexponential fits with $\sigma \gg$ mean near zero are reported as zero.

Sample	Residue Lifetime (μs)	τ_o/τ
τ_o : 0.048 $\mu\text{mol UO}_2^{2+}$	225 ± 2 ($R^2=0.999$)	1.00
EtOH	67.5 ± 4.7 ($R^2=0.952$)	3.33
EtOH + 20mM POSS1444	66.5 ± 4.4 ($R^2=0.956$)	3.38
500mM AMP-EtOH	52.0 ± 2.6 ($R^2=0.977$)	4.33
500mM AMP-EtOH + 20mM POSS1444	63.1 ± 3.2 ($R^2=0.975$)	3.57
500mM AMP-EtOH-HNO ₃	67.0 ± 3.2 ($R^2=0.975$)	3.36
500mM AMP-EtOH-HNO ₃ + 20mM POSS1444	69.3 ± 3.4 ($R^2=0.976$)	3.25
500mM TEA-EtOH	0	n/a
500mM TEA-EtOH + 20mM POSS1444	0	n/a
500mM TEA-EtOH-HNO ₃	0	n/a
500mM TEA-EtOH-HNO ₃ + 20mM POSS1444	0	n/a
500mM AMP-EtOH-HNO ₃ + 20mM POSS1460Na	77.1 ± 5.2 ($R^2=0.956$)	2.92

The quenching effect of EtOH is evident in the 3 to 4-fold shorter ($\tau_o/\tau = 3$ to 4) lifetime values in the EtOH and AMP-based samples and the lack of measurable lifetimes in the TEA-based samples. Monoexponential fitting of the fluorescence decays resulted in high correlations for all but the TEA-based samples. These samples had errors orders of magnitude higher than the calculated mean lifetime and as such are reported as zero. The significant fluorescence intensity and lifetime quenching in these samples suggest the interaction of TEA with uranyl forms a dark, or non-fluorescent, complex. The EtOH

and AMP-based residue lifetimes exceed 50 μ s but appear to be governed by the presence of EtOH rather than the addition of AMP or POSS[®] under the conditions investigated. Within 1 σ , there is no significant difference in the lifetime with POSS[®] SO1444 (≤ 72.7 μ s) compared to POSS[®] SO1460Na (≥ 71.9 μ s) in the AMP-EtOH-HNO₃ residues. Given that residue intensities are quenched 10-fold and the lifetimes are quenched approximately 3-fold, clearly utilizing a solvent other than EtOH would be a prudent approach to improving detection.

4.4.4 Effect of Iron and POSS[®] on Uranyl Fluorescence

Recall that ‘solid samples’ are the dried deposits of aqueous solution samples on inorganic filters, ‘residue samples’ are the vacuum filtered and dried products of contacting ethanol-based solutions with solid samples, and the filtrates are collected EtOH-based solutions following contact and vacuum filtration. For the results presented and discussed in this section, the solid samples are 0.048 μ mol UO₂²⁺ and 0.425 μ mol Fe³⁺ on inorganic filters.

Solution and Filtrate pH Measurements Table 4-11 lists the measured pH of the EtOH-based solutions as prepared and the collected filtrates following a 30 minute contact with solid 0.048 μ mol UO₂²⁺ and 0.425 μ mol Fe³⁺ samples on inorganic filters. Measurement of pH was used only as a qualitative indicator of changing solution conditions. The solutions are well buffered, especially those with AMP, and significant pH change is only observed in the non-buffered solutions. The presence of Fe³⁺ has negligible effect on the measured filtrate pH when compared to pH values measured in its absence (Table 4-8).

Table 4-11. EtOH-based solution or filtrate pH at room temperature. Filtrates contacted 30 minutes with solid 0.048 μmol UO_2^{2+} and 0.425 μmol Fe^{3+} samples.

Solution or Filtrate	pH, solution	pH, filtrate
EtOH	8.1	0.4
EtOH + 20mM POSS1444	7.5	0.6
500mM AMP-EtOH	10.6	9.8
500mM AMP-EtOH + 20mM POSS1444	9.7	9.7
500mM AMP-EtOH-HNO ₃	9.5	9.5
500mM AMP-EtOH-HNO ₃ + 20mM POSS1444	9.4	9.4
500mM TEA-EtOH	9.3	7.7
500mM TEA-EtOH + 20mM POSS1444	8.5	7.5
500mM TEA-EtOH-HNO ₃	7.8	7.4
500mM TEA-EtOH-HNO ₃ + 20mM POSS1444	7.8	7.3
500mM AMP-EtOH-HNO ₃ + 20mM POSS1460Na	11.9	12.0

4.4.4.1 Filtrate and Residue Fluorescence Intensity Measurements

Net fluorescence intensities, summed between 450 nm and 650 nm, are listed in Table 4-12 for the residues and collected filtrates resulting from contacting each EtOH-based solution (see Table 4-4) with a solid 0.048 μmol UO_2^{2+} and 0.425 μmol Fe^{3+} sample. The ratio I_o/I for each sample was calculated using the summed net intensity of the solid 0.048 μmol UO_2^{2+} sample as I_o . Recall from §4.4.3.2 that the more the residue I_o/I value exceeds unity, the greater the fluorescence quenching or the loss of UO_2^{2+} to the filtrate. The decrease in residue I_o/I value upon the addition of either POSS[®] SO1444 and POSS[®] SO1460Na to a similar solution is two- or three-fold, indicating enhanced detection potential of uranyl fluorescence in the presence of Fe^{3+} . For example, the I_o/I value for 500 mM AMP-EtOH-HNO₃ residue is 73. With the addition of POSS[®] SO1444 to the applied solution, the I_o/I value for the resulting residue decreases to 28. The net relative fluorescence increase due to the presence of POSS[®] SO1444 is 2.6 as determined by a ratio of the net fluorescence intensities. Fluorescence is further quenched upon POSS[®]

addition in the TEA-based residues. For example, the I_o/I value for 500 mM TEA-EtOH-HNO₃ is 32. With the addition of POSS[®] SO1444 to the applied solution, the I_o/I value of the resulting residue increases to 48. The net relative fluorescence increase due to the presence of POSS[®] SO1444 is 0.7, indicating a decrease.

Table 4-12. Summed net fluorescence intensities (I) for residues and filtrates of EtOH-based solutions contacted with solid 0.048 $\mu\text{mol UO}_2^{2+}$ and 0.425 $\mu\text{mol Fe}^{3+}$ samples.

Sample	Residue		Filtrate
	I	I_o/I	I
I_o : 0.048 $\mu\text{mol UO}_2^{2+}$	19961	1	45
0.048 $\mu\text{mol UO}_2^{2+}$ and 0.425 $\mu\text{mol Fe}^{3+}$	3153	6	n/a
EtOH	539	37	585
EtOH + 20mM POSS1444	812	25	55
500mM AMP-EtOH	296	67	106
500mM AMP-EtOH + 20mM POSS1444	597	33	96
500mM AMP-EtOH-HNO ₃	274	73	88
500mM AMP-EtOH-HNO ₃ + 20mM POSS1444	724	28	135
500mM TEA-EtOH	426	47	51
500mM TEA-EtOH + 20mM POSS1444	207	97	72
500mM TEA-EtOH-HNO ₃	619	32	52
500mM TEA-EtOH-HNO ₃ + 20mM POSS1444	414	48	62
500mM AMP-EtOH-HNO ₃ + 20mM POSS1460Na	582	37	469

Fluorescence spectra of residues without POSS[®] are presented in Figure 4-24. Fluorescence in the presence of iron is measurably above background, but the intensities are less than in its absence. Uranyl fluorescence in these residues is significantly quenched ($37 \leq I_o/I \leq 73$) and lack the spectral structure observed in the EtOH and AMP-based residues in the absence of iron (Figure 4-21). The presence of iron caused a change in the speciation, such that all of the residues without POSS[®] appear to have similar speciation to solutions with pH 7, but with very low fluorescence intensity.

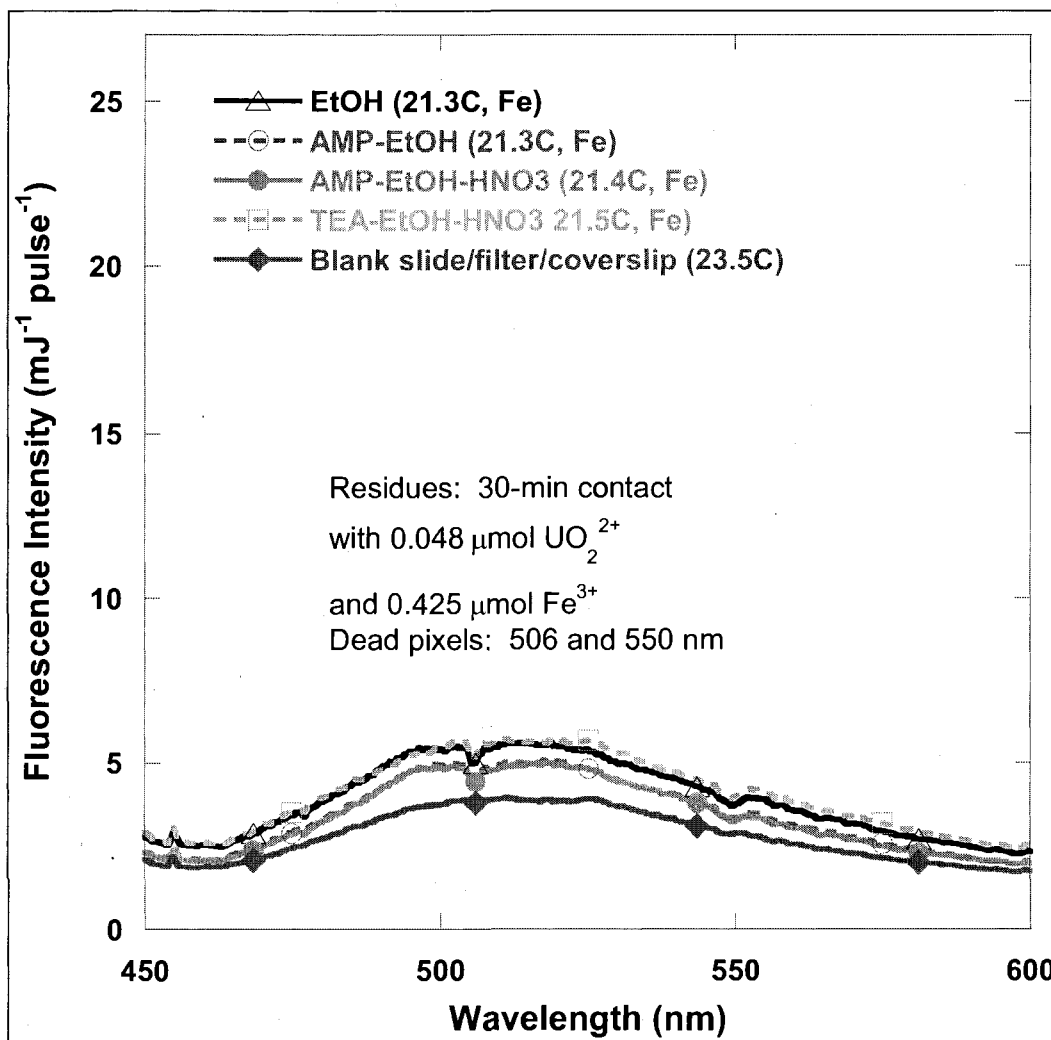


Figure 4-24. Residue fluorescence intensity of 0.048 $\mu\text{mol UO}_2^{2+}$ and 0.425 $\mu\text{mol Fe}^{3+}$ contacted with EtOH-based solutions. Measurement temperature ($^{\circ}\text{C}$) listed in legend.

Similar to the residues prepared in the absence of iron (§4.4.3.2), the addition of POSS[®] to the solutions contacted with solid 0.048 $\mu\text{mol UO}_2^{2+}$ and 0.425 $\mu\text{mol Fe}^{3+}$ samples enhanced the fluorescence intensity. However, the overall fluorescence is still negligible due to the quenching from EtOH and Fe^{3+} . The addition of POSS[®] SO1460Na to the applied solutions results in a residue spectral red-shift of approximately 10 nm, consistent with the higher pH of 11.9 for the applied solution and indicates a higher

degree of coordination than demonstrated without POSS[®] or with POSS[®] SO1444 (Figure 4-25).

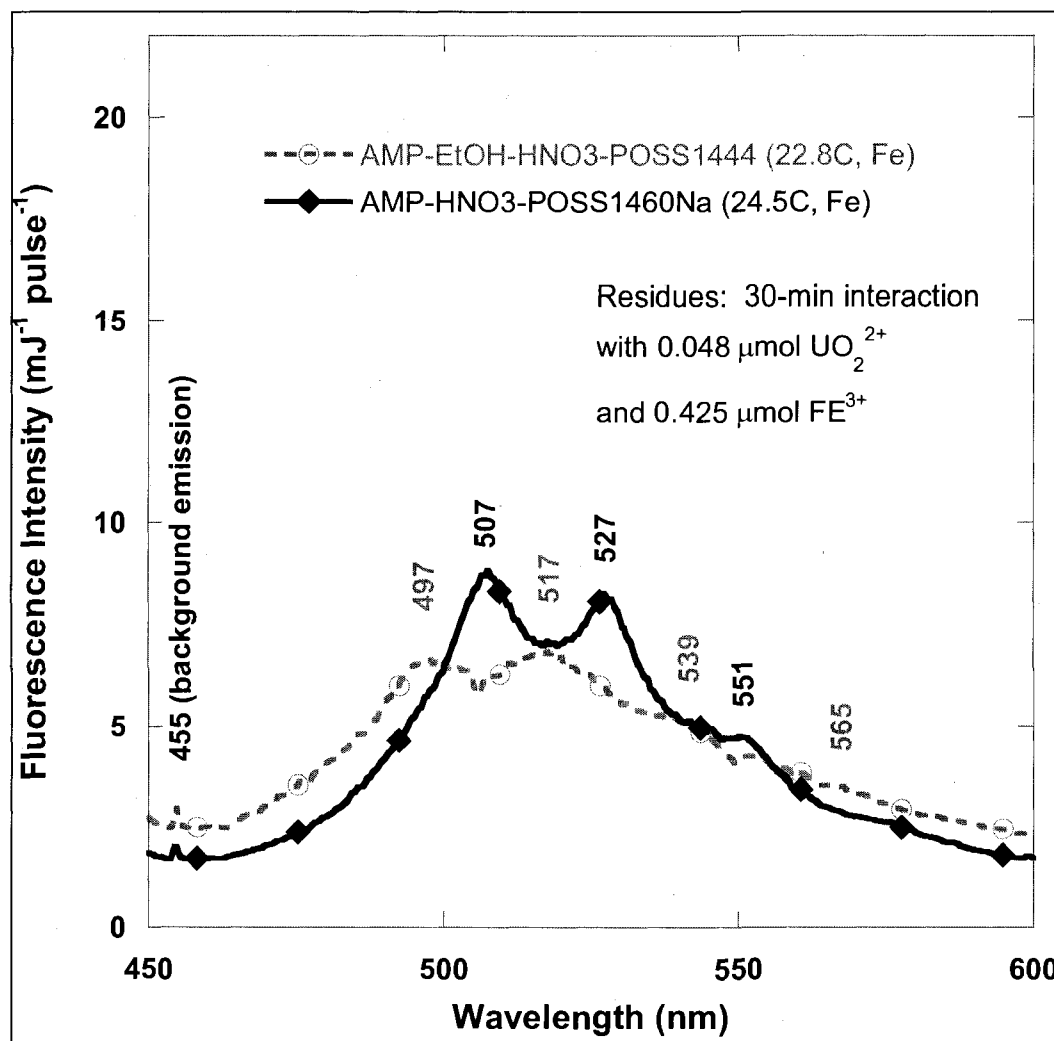


Figure 4-25. AMP-based residue fluorescence intensity with POSS[®] SO1444 and POSS[®] SO1460Na in the presence of iron. Measurement temperature (°C) listed in legend..

4.4.4.2 Residue Fluorescence Lifetime Measurements

The calculated monoexponential lifetimes for the residues of EtOH-based solutions contacted with solid 0.048 $\mu\text{mol UO}_2^{2+}$ and 0.425 $\mu\text{mol Fe}^{3+}$ samples are listed in Table

4-13. The ratio τ_o/τ for each sample was calculated using the lifetime of the 0.048 μmol UO_2^{2+} sample (225 μs) as τ_o .

Table 4-13. Residue fluorescence lifetimes (μs) in the presence of iron at room temperature. Monoexponential fits with $\sigma \gg$ mean near zero are reported as zero.

Sample	Filtrand Lifetime (μs)	τ_o/τ
τ_o : 0.048 μmol UO_2^{2+}	225 ± 2 ($R^2=0.999$)	1.00
0.048 μmol UO_2^{2+} and 0.425 μmol Fe^{3+}	124 ± 5 ($R^2=0.9826$)	1.81
EtOH	15.4 ± 4.7 ($R^2=0.864$)	14.6
EtOH + 20mM POSS1444	34.1 ± 5.5 ($R^2=0.836$)	6.60
500mM AMP-EtOH	0	n/a
500mM AMP-EtOH + 20mM POSS1444	17.6 ± 3.0 ($R^2=0.932$)	12.8
500mM AMP-EtOH-HNO ₃	0	n/a
500mM AMP-EtOH-HNO ₃ + 20mM POSS1444	13.4 ± 3.8 ($R^2=0.926$)	16.8
500mM TEA-EtOH	0	n/a
500mM TEA-EtOH + 20mM POSS1444	0	n/a
500mM TEA-EtOH-HNO ₃	0	n/a
500mM TEA-EtOH-HNO ₃ + 20mM POSS1444	0	n/a
500mM AMP-EtOH-HNO ₃ + 20mM POSS1460Na	46.4 ± 5.3 ($R^2=0.897$)	4.85

The presence of iron quenches all of the residue lifetimes over those in its absence (Table 4-10). Without POSS[®], only the EtOH residue had a measurable lifetime, which contrasts with the results obtained without iron. The presence of iron seems to result in the formation of a dark complex with both buffers, where it was only likely before with the TEA. This explains the similarity in spectra in Figure 4-24, the very high I_o/I ratios, and the lifetime values reported as zero. Adding POSS[®] SO1444 doubles the intensities, halves the I_o/I ratios, and results in lifetimes of 10 to 20 μs for the AMP-based residues. Adding POSS[®] SO1460Na further enhances the intensity and results in a mean lifetime of 46 μs for the AMP-based residue. This difference in lifetime between the two ligands

is significant and warrants further study. Based on their differing structures (Figure 4-5 and Figure 4-6) and pH in EtOH⁴, the POSS[®] SO1460Na should result in complexes of higher coordination that result in increased fluorescence intensity and longer lifetime over POSS[®] SO1444. This is likely due the speciation and coordination of the POSS[®] SO1460Na as it provides additional shielding of the uranyl from iron which would in turn increase fluorescence.

4.5 Conclusions

Preparation of a uranyl perchlorate stock solution resulted in absorption and emission peak locations, as well as a lifetime, that were in agreement with other published values for comparable media and temperatures. Samples prepared using this stock solution were diluted with a pH-adjusted diluent to prevent uranyl hydrolysis. The use of a monoexponential fit resulted in a lifetime of $4.08 \pm 0.02 \mu\text{s}$ for a 4.8 mM $\text{UO}_2(\text{ClO}_4)_2$ solution at 23 °C. A dried aliquot of this solution resulted in emission peaks that were more intense and red-shifted compared to those in solution. The lifetime of this solid 0.048 $\mu\text{mol UO}_2(\text{ClO}_4)_2$ sample was $225 \pm 2 \mu\text{s}$ at 23 °C.

Incremental additions of Fe^{3+} in the form of $\text{Fe}(\text{ClO}_4)_3$ to the solutions decreased uranyl fluorescence intensity linearly with increasing $[\text{Fe}^{3+}]$ for aqueous solutions containing $\leq 85 \text{ mM Fe}^{3+}$ and for solid samples containing $\leq 0.85 \mu\text{mol Fe}^{3+}$. In the solutions, intensities were quenched $< 10\%$ by the presence of 42.5 mM Fe^{3+} ; however in the solid samples, quenching exceeded 75% due to 0.425 $\mu\text{mol Fe}^{3+}$, a similar mole ratio of UO_2^{2+} and Fe^{3+} for both the solution and solid samples. Lifetimes of the solution and solid samples were $3.83 \pm 0.03 \mu\text{s}$ and $123.7 \pm 4.9 \mu\text{s}$, respectively, at room temperature.

⁴ 20 mM POSS[®] SO1444 in EtOH (pH = 7.5) and 20 mM POSS[®] SO1460Na (pH = 11.9)

The reduction in both fluorescence intensity and lifetime is observed in conditions of high excess of iron to uranyl. Electron transfer in the interaction of Fe^{3+} and the excited uranyl, $(\text{UO}_2^{2+})^*$ occurs very effectively in these high ratio environments, especially as the solution dries, and the distances between ions and their ability to reorient relative to each other decreases.

Ethanol is known to quench uranyl fluorescence intensity and lifetime by the same mechanism as iron, namely dynamic quenching. EtOH and buffered-EtOH solutions were contacted with solid 0.048 μmol $\text{UO}_2(\text{ClO}_4)_2$ samples and vacuum filtered to baseline the fluorescence intensities of the resulting residues prior to the addition of POSS[®] ligands. The EtOH solution reduced the detected fluorescence intensity of the resulting residue by greater than 20-fold and its lifetime by greater than three-fold when compared to those of the initial solid $\text{UO}_2(\text{ClO}_4)_2$. However, a portion of the uranyl perchlorate was redissolved into the EtOH, resulting in reduced EtOH residue fluorescence intensity and correspondingly increased EtOH filtrate fluorescence intensity. Fluorescence intensities and lifetimes of residues resulting from the contact of EtOH-based solutions with solid uranyl and iron perchlorate samples are summarized in Table 4-14.

Table 4-14. Comparison of residue fluorescence intensities and lifetimes in the presence and absence of Fe^{3+} .

Sample	Residue I_0/I		Residue τ_0/τ	
	$\text{Fe}^{3+} = 0$	$\text{Fe}^{3+} = 0.425$ μmol	$\text{Fe}^{3+} = 0$	$\text{Fe}^{3+} = 0.425$ μmol
Solid 0.048 μmol UO_2^{2+}	1	6	1	1.8
AMP-EtOH- HNO_3	7	73	3.4	n/a
AMP-EtOH- HNO_3 + POSS [®] SO1444	10	28	3.3	16.8
AMP-EtOH- HNO_3 + POSS [®] SO1460Na	10	37	2.9	4.9
TEA-EtOH- HNO_3	21	32	n/a	n/a
TEA-EtOH- HNO_3 + POSS [®] SO1444	44	48	n/a	n/a

Recall that uranyl fluorescence quenching increases as the residue $I_o/I \rightarrow \infty$ or $\tau_o/\tau \rightarrow \infty$. The addition of iron in the solid samples itself effects a six-fold decrease in intensity and nearly two-fold decrease in lifetime. The use of AMP or TEA-buffered EtOH solutions results in large variations in residue intensities and lifetimes between them and upon the addition of iron or POSS[®]. The presence of iron further quenches intensities and lifetimes, regardless of the ligand solution. However, the addition of POSS[®] to AMP-buffered EtOH counters over half of that additional intensity quenching and restores the lifetime to a measurable value. The use of POSS[®] SO1460Na provides a longer lifetime for detection, especially in the presence of iron, than the use of POSS[®] SO1444 despite additional intensity quenching. The use of TEA-buffered solutions significantly quenches fluorescence intensity and results in lifetimes that are essentially zero. The higher pH (9.4) of the AMP-buffered solutions compared to those of EtOH or TEA-buffered solutions (~ 8) is expected to increase uranyl hydrolysis and therefore accounts for at least some of the increased fluorescence intensity due to fundamental changes in speciation.

Prior to POSS[®] addition, all residue fluorescence spectra were similar in peak locations to those of solutions in the pH range of 5 to 8.5, indicating the uranyl speciation and chemical environment was similar for the examined samples. Upon addition of POSS[®] SO1460Na, the spectrum red-shifts approximately 10 nm, consistent with the increased uranyl hydrolysis at the higher pH of 11.9.

The use of ethanol as a solvent quenches the fluorescence of solid samples at least seven-fold in intensity and three-fold in lifetime, prior to the addition of buffers, additional acids, ligands, or iron. Buffering the EtOH with AMP or TEA, resulted in

residue fluorescence intensities that were quenched up to 44-fold in the absence of iron(III) and up to 73-fold in its presence at high excess relative to uranyl. Fluorescence lifetimes were not measurable for any of the TEA-buffered solutions or for the AMP-buffered solution without POSS[®] in the presence of iron.

Solvents that are effective for ligand dissolution and do not quench uranyl fluorescence are essential. For example, tetrahydrofuran dissolves POSS[®] ligands and does not quench uranyl fluorescence, but does itself fluoresce in an overlapping wavelength region. Stepwise investigation of the uranyl-ligand coordination should include further spectrometry and structural analysis of the complexes. Application of ligand solutions to residual uranyl or iron-containing solids should not be vacuum filtered since dissolution of the uranyl into the filtrate decrease the reliability of the resulting residue intensity measurements.

The successful use of a ligand solution to enhance the fluorescence intensity or lifetime of uranyl in the presence of quenchers, including iron(III), has been demonstrated in this work and in the provided references. The initial use of phosphate-based solutions in this work, to include phosphoric acid, sodium phosphate dibasic, and pH 7 buffer solutions, validated the theory that significant enhancement in uranyl fluorescence is achievable through their use. Several studies indicate an aqueous concentration of 10% H₃PO₄ optimizes the fluorescence intensity of uranyl under various conditions (Arruda et al., 1999; Bonhoure et al., 2007; Geipel, 2006; Kaminski et al., 1981). In addition, uranyl-specific complexation is possible using ion imprinted polymers. It is thought that in the presence of iron(III), the complexed uranyl would be shielded from the quenching effects of the iron such that fluorescence intensity is

maintained or enhanced (Preetha et al., 2006; Say et al., 2003; Noyes et al., 2002).. The availability of alternative, non-quenching solvents as well as ligands or polymers known to enhance uranyl fluorescence provides ample opportunity for future studies to optimize their development and future application.

CHAPTER 5

CONCLUSIONS AND RECOMMENDATIONS

5.1 Conclusions

This research developed and investigated the performance of scintillator-loaded polymer films and ligand solutions to enhance the detection of induced fluorescence from residual radioactive materials. The use of scintillation counting to measure the fluorescence (scintillation) intensity induced by radioactive material decays is dependent on background, the source radiation activity and type, the scintillator properties, and signal losses. Measurement of laser-induced fluorescence intensity and its time-dependent decay similarly depends on background, the fluorescent material properties, and signal losses. Both studies evaluated conditions to achieve the maximum photon emission from the induced fluorescence for the detection of radionuclides. For each system, chemical environments or media were identified to achieve maximum fluorescence within the experimental range.

5.1.1 Radioactive Material-Induced Fluorescence Experiments

Barium fluoride (BaF_2) is a common inorganic scintillator and was chosen based on its characteristic ultraviolet scintillations. These scintillations at 195, 220, and 310 nm occur in a solar-blind region (< 315 nm) where nearly all solar ultraviolet (UV) radiation is absorbed by atmospheric ozone. The transmission of BaF_2 at its scintillations wavelengths is nearly 100% and self-absorption can therefore be neglected. However,

the sizes of the BaF₂ particles used ranged from 0.25 – 5 μ m, based on scanning electron microscopy (SEM) imaging, which could introduce significant scatter and subsequent absorption of the scintillations by adjacent crystals or polymer in loaded films.

Poly(ethylene-co-vinyl acetate), or EVA, dissolved in carbon tetrachloride (CCl₄) was used to produce clear, flexible, and strippable films even though the EVA absorbs at the scintillations wavelengths of 195 and 220 nm. Since nearly 80% of the BaF₂ scintillations at room temperature occur at 310 nm, where EVA photon transmission is 61 \pm 6%, the potential intensity loss due to absorption in the polymer was deemed acceptable. Kinetic scanning using UV-visible spectrometry verified that the films were thoroughly dried after 90 minutes and there was no residual absorption attributable to CCl₄. Polymer thin films were prepared by vortex and ultrasonic mixing of varying mass percentages of BaF₂ powder into EVA-CCl₄ solutions, drawing the films to a desired thickness, and drying them 24-48 hours to remove residual water and solvent.

BaF₂-loaded films were exposed to a 1.445 mCi ⁹⁹Tc source to simulate application of a scintillator-loaded strippable coating to a contaminated surface. Although the source strength likely exceeds that expected on surfaces, and the decay type and energy (β^- , E_{max} = 294 keV) may differ, this source permits characterization of the films with adequate signal-to-noise and is suitable to demonstrate the principles of the interaction. The Bremsstrahlung radiation from ⁹⁹Tc was shown not to contribute to the response of the UV-sensitive CCD camera. Heat exhausted due to thermoelectric cooling of the camera inside a dark box potentially increases the background noise, since near-IR wavelengths are transmitted up to 50% through the UV-transmittive filter attached to the camera lens. Density thickness, calculated as the product of the film effective density and dry

thickness, increased exponentially with increasing BaF₂ mass loading. When the film density thickness equals that of the beta particle range, 0.076 g/cm³, the scintillations produced from a given source are fully attenuated and absorbed within the film. This causes a plateau in the detectable intensity. As the film thickness increases beyond the range of the source, losses due to increased scatter and absorption decrease the fraction of scintillations detected. As the scintillations are produced isotropically within the film, a 50-cm film-to-CCD distance was used as the detection geometry to minimize solid angle losses. The resulting scintillations measured during a 45-minute exposure showed predictable increases for a given film thickness as a function of BaF₂ load. Intensities for a given BaF₂ load as a function of film thickness varied as a result of the dependence on the beta particle range and associated losses. Maximum scintillations were measured in films drawn to 508 μm and loaded to 80% BaF₂ by mass. These thin films, with high BaF₂ loading, illustrate the balance between scintillation production due to the interaction of beta particles with the scintillator and loss due to attenuation of the produced photons. Although films of 102 μm dry thickness and 80% BaF₂ have a density thickness less than the range of the beta particle, they provide a high scintillator density. This density attenuates the source beta particles in a thin linear layer and serves to minimize the scatter and absorption of the resulting scintillations. The detection of radioactive materials by application of scintillator-loaded polymer films requires optimization increase light yields and to overcome scatter and absorption losses; however, its feasibility has been demonstrated.

5.1.2 Laser-Induced Fluorescence Experiments

Functionalized silicon-based ligands, polyhedral oligomeric silsesquioxane (POSS[®]), were chosen based on their potential to complex UO_2^{2+} or Fe^{3+} and thereby shield uranyl from the quenching of iron that inhibits its detection. The ligands are not water-soluble and were therefore dissolved in ethanol and deposited onto prepared solids of dried uranyl perchlorate, in the absence and presence of iron(III). Ethanol quenching of uranyl fluorescence is well known (Sakuraba and Matsushima, 1971; Wheeler and Thomas, 1984) and was consistently observed in the decreased intensity and lifetime of the measured fluorescence. The aqueous uranyl perchlorate used as the fluorophore had lifetime of $4.08 \pm 0.02 \mu\text{s}$ for a 4.8 mM $\text{UO}_2(\text{ClO}_4)_2$ solution at pH 0.6 and of $225 \pm 2 \mu\text{s}$ for a dried aliquot (0.048 μmol $\text{UO}_2(\text{ClO}_4)_2$ residue), both at 23 °C. Lifetimes calculated from the time-dependent fluorescence decay had high correlations using a monoexponential fit but were reported as zero if the standard deviation greatly exceeded a measured lifetime near zero. The emission peaks of the residue were more intense and red-shifted by 6 nm compared to those in solution due to increased coordination of water to the uranyl in preference to perchlorate as the solution dries. Neither sample demonstrated a spectral shift in the presence of Fe^{3+} , indicating Fe(III) did not influence the speciation of uranyl. The chosen $[\text{Fe}^{3+}]$ of 42.5 mM quenched solution intensity < 10% compared to the $\text{UO}_2(\text{ClO}_4)_2$ solution, and quenched residue intensity by greater than 75%. With 8.85 times molar excess Fe(III) added, dynamically quenched lifetimes at 23 °C were $3.73 \pm 0.03 \mu\text{s}$ for the $4.8 \pm 0.2 \text{ mM}$ $\text{UO}_2(\text{ClO}_4)_2$ (aq) solution at pH 0.6 and $124 \pm 5 \mu\text{s}$ for the 0.048 μmol $\text{UO}_2(\text{ClO}_4)_2$ solid.

Contact of ethanol with the solid $\text{UO}_2(\text{ClO}_4)_2$ sample and subsequent vacuum filtration resulted in the expected dissolution of uranyl into the filtrate. However, addition of 2-amino-2-methyl-1-propanol (AMP) or triethanolamine (TEA) buffers, due to their high pH and subsequent formation of insoluble species, decreased the solubility of uranyl in ethanol sufficiently for fluorescence to be observed in the residue rather than in the filtrate. EtOH-based solutions prepared with the two investigated ligands, POSS[®] SO1444 and POSS[®] SO1460Na, resulted in no enhancement to either the uranyl fluoresce intensity or lifetime, with or without iron present, compared to the $\text{UO}_2(\text{ClO}_4)_2$ residue. The combined quenching effects of EtOH and Fe^{3+} yielded intensities that were reduced up to 73-fold compared to the $\text{UO}_2(\text{ClO}_4)_2$ residue and lifetimes that in some cases were not feasibly measurable. However, improvements in both measured intensities and lifetimes were observed upon the addition of POSS[®] SO1444 and POSS[®] SO1460Na to pH-adjusted AMP-EtOH solutions. Within 1σ , there is no significant difference in the residue lifetime resulting from contact with the AMP-EtOH- HNO_3 solutions of POSS[®] SO1444 ($69.3 \pm 3.4 \mu\text{s}$) compared to those of POSS[®] SO1460Na ($77.1 \pm 5.2 \mu\text{s}$). The detection of uranyl fluorescence has not been enhanced by the application of either of the POSS[®] ligand investigated, with dynamic quenching primarily the result of the solvent ethanol. Laser-induced uranyl fluorescence requires optimization of the ligand solutions to minimize quenching and to increase light yields; however, its feasibility has been demonstrated.

5.2 Recommendations

5.2.1 Radioactive Material-Induced Fluorescence Experiments

Detectable scintillation intensity may be further optimized by increasing the scintillation production and decreasing absorption losses within the films. Lutetium aluminum garnet activated with scandium, LuAG(Sc) has a high light yield of 22.4 photons $(\text{keV } \gamma)^{-1}$ at 275 nm, is non-hygrosopic, and can be synthesized as nanoparticles for use as a scintillator (Ryskin et al., 1994; Zorenko et al., 2005). Since scatter increases with the scintillator particle size, the use of nanoparticles would significantly decrease absorption by the surrounding polymer and afford high loading into thin films. Many solvents are available with UV cutoff wavelengths below those of potential scintillations and that would effectively dissolve other candidate polymers. Finally, the polymer choice needs to be based on the scintillation wavelengths to ensure absorption is negligible. Polyethylene and polypropylene are transparent to solar-blind wavelength photons but may require the use of UV-transparent plasticizers to enhance their flexibility and ease of removal.

5.2.2 Laser-Induced Fluorescence Experiments

The detection of uranium via laser-induced fluorescence requires minimization of the competitive processes that result in the non-radiative deactivation of the excited fluorophore, assumed to be uranyl. Sequestration of the uranyl from available quenching agents is practical by selective coordination with a ligand in solution. Unlike the ethanol investigated in this research, the solvent must not quench fluorescence, regardless of whether the matrix effects are assumed to dissipate with its evaporation. Aqueous-based solutions are recommended for initial experiments since speciation models are available

to assist in optimizing the conditions favorable to specific uranyl-ligand coordination. Often, dissolved oxygen is considered a quencher of the triplet state, as it promotes intersystem crossing, conversions, and oxidization of the fluorescing species (Skoog et al., 2007). However, oxygen reportedly does not affect $(\text{UO}_2^{2+})^*$ (Wheeler et al., 1984), assists in maintaining uranium in the hexavalent oxidation state, and may result in a doubling of the lifetime (Hill et al., 1974).

The use of phosphates and fluorides to enhance uranyl fluorescence is well studied (Arruda et al., 1999; Bonhoure et al., 2007; Geipel, 2006; Kaminski et al., 1981). The coordinated anions shield the uranyl ion resulting in significant increases in fluorescence intensities. Solutions containing phosphoric acid, sodium phosphate dibasic, pH 7 buffer solutions, or sodium fluoride were investigated in this research, and while not presented here, validate the observed fluorescence enhancement, especially in solutions containing 10% H_3PO_4 . In addition, ion imprinted polymers have recently been developed and characterized for the selective complexation of uranyl in the presence of other metals, including Fe(III), with up to 100% recovery (Preetha et al., 2006; Say et al., 2003; Noyes et al., 2002).

With further research, the detection of residual radioactive materials based on their laser-induced fluorescence or the scintillations from coatings applied to them is practical. Signal enhancement can be accomplished with the use of well-characterized scintillators or ligands that are optimized for the radiation decay type or metal of interest. In addition, minimization of background interferences and quenching is essential to preserve and detect the produced fluorescence. Scintillation counting in the solar-blind region nearly eliminates background solar UV radiation. Scrutiny in selection of the matrix used to

suspend or dissolve the chosen scintillator or ligand is essential to reduce absorption of the fluorescence or its prevention by quenching. These recommendations serve as starting point for future research that may result in a fielded system with high efficiency and selectivity in the detection of residual radioactive materials.

BIBLIOGRAPHY

- Arruda, A. F.; Campiglia, A. D.; Chauhan, B. P. S.; Boudjouk, P. New organosilicon polymer for the extraction and luminescence analysis of uranyl in environmental samples. *Analytica Chimica Acta* **1999**, 396(2-3), pp 263-272.
- Bae, S. Y.; Southard, G. L.; Murray, G. M. Molecularly imprinted ion exchange resin for purification, preconcentration and determination of UO_2^{2+} by spectrophotometry and plasma spectrometry. *Analytica Chimica Acta* **1999**, 397(1-3), pp 173-181.
- Baumann, N.; Brendler, V.; Arnold, T.; Geipel, G.; Bernhard, G. Uranyl sorption onto gibbsite studied by time-resolved laser-induced fluorescence spectroscopy (TRLFS). *J Colloid Interface Sci.* **2005**, 290, pp 318-324.
- Bell, J.T.; Biggers, R.E. The Absorption Spectrum of the Uranyl Ion in Perchlorate Media. Part I. Mathematical Resolution of the Overlapping Band Structure and Studies of the Environmental Effects. *J. Mol. Spectrosc.* **1965**, 18, pp 247-275.
- Billard, I.; Rustenholtz, A.; Semon, L.; Lutzenkirchen, K. Fluorescence of UO_2^{2+} in a non-complexing medium: $\text{HClO}_4/\text{NaClO}_4$ up to 10 M. *Chem. Phys.* **2001**, 270(2), pp 345-354.
- Bonhoure, I.; Meca, S.; Marti, V.; De Pablo, J.; Cortina, J.-L. A new time-resolved laser-induced fluorescence spectrometry (TRLFS) data acquisition procedure applied to the uranyl-phosphate system. *Radiochim. Acta* **2007**, 95(3), pp 165-172.
- Bouby, M.; Billard, I.; Bonnenfant, A.; Klein, G. Are the changes in the lifetime of the excited uranyl ion of chemical or physical nature? *Chem. Phys.* **1999**, 240(3), pp 353-370.
- Burrows, H.D.; Cardoso, A.C.; Formosinho, S.J.; Miguel, M.M. Photophysics of the Excited Uranyl Ion in Aqueous Solutions. Part 4.—Quenching by Metal Ions. *J. Chem. Soc., Faraday Trans. 1*, **1985**, 81, pp 49-60.
- Burrows, H.D.; Formosinho, S.J. Uranyl Luminescence Quenching. *J. Chem. Educ.* **1978**, 55(2), pp 125-126.
- Cember, H. *Introduction to Health Physics*, 3rd ed.; McGraw-Hill: New York, NY, 1996; pp 125-129.

- Cordfunke, E.H.P. *The Chemistry of Uranium*; Elsevier: Amsterdam, The Netherlands, 1969; p 114.
- DeNeufville, J.P.; Kasdan, A.; Chimenti, R.J.L. Selective detection of uranium by laser-induced fluorescence: a potential remote-sensing technique. 1. Optical characteristics of uranyl geologic targets. *Appl. Optics* **1981**, 20(8), p 1286.
- Geipel, G.; Bernhard, G.; Rutsch, M.; Brendler, V.; Nitsche, H. Spectroscopic properties of uranium(VI) minerals studied by time-resolved laser-induced fluorescence spectroscopy (TRLFS). *Radiochim. Acta* **2000**, 88, p 757.
- Geipel, G. Some aspects of actinide speciation by laser-induced spectroscopy. *Coordin. Chem. Rev.* **2006**, 250(7-8), pp 844-854.
- Günther, A.; Geipel, G.; Bernhard, G. Complex formation of uranium(VI) with the amino acids L-glycine and L-cysteine : A fluorescence emission and UV-Vis absorption study. *Polyhedron* **2007**, 26, pp 59-65.
- Hill, R.J.; Kemp, T.J.; Allen, D.M.; Cox, A. Absorption Spectrum, Lifetime and Photoreactivity towards Alcohols of the Excited State of the Uranyl Ion (UO_2^{2+}). *J. Chem. Soc. Faraday Trans.* **1974**, 70, 847 -857.
- Kaminski, R.; Purcell, F.J.; Russavage, E. Uranyl phosphorescence at the parts-per-trillion level. *Anal. Chem.* **1981**, 53(7), pp 1093-1096.
- Kirishima, A.; Kimura, T.; Tochiyama, O.; Yoshida, Z. Speciation study on complex formation of uranium(VI) with phosphate and fluoride at high temperatures and pressures by time-resolved laser-induced fluorescence spectroscopy. *Radiochim. Acta* **2004**, 92, pp 889-896.
- Knoll, G. F. *Radiation Detection and Measurement*, 3rd ed.; John Wiley & sons: New York, NY, 2000; pp 235-241.
- Lakowicz, J.R. *Principles of Fluorescence Spectroscopy*, 2nd ed.; Kluwer Academic/Plenum Publishers: New York, NY, 1999; pp 241-242.
- Lide, D.R. *CRC Handbook of Chemistry and Physics*, 87th ed. (Internet Version 2007); CRC Press/Taylor and Francis: Boca Raton, FL.
- Lopez, M.; Birch, D.J.S. Characterisation of the dimer formed by hydrolysis of uranyl in aqueous solution and its role in the biexponential luminescence decay. *Chem. Phys. Lett.* **1997**, 268, pp 125-132.
- Matsushima, R.; Fujimori, H.; Sakuraba, S. Quenching of the Uranyl (UO_2^{2+}) Emission by Inorganic Ions in Solution. *J. Chem. Soc., Faraday Trans. 1* **1974**, 70, pp 1702 – 1709.

- Meinrath, G.; Kato, Y.; Yoshida, Z. Spectroscopic study of the uranyl hydrolysis species $(\text{UO}_2)_2(\text{OH})_2^{2+}$. *J. Radioanal. Nucl. Chem.* **1993**, *174*(2), pp 299-314.
- Meinrath, G. Uranium(VI) speciation by spectroscopy. *J. Radioanal. Nucl. Chem.* **1997**, *224*(1-2), pp 119-126.
- Meinrath, G. Aquatic Chemistry of Uranium: A Review Focusing on Aspects of Environmental Chemistry, Vol. 1. *Freiberg On-Line Geoscience* [Online] **1998**, pp 17-21, 59.
- Moriyasu, M.; Yokoyama, Y.; Ikeda, S. Quenching Mechanisms of Uranyl Luminescence by Metal Ions. *J. Inorg. Nucl. Chem.* **1977**, *39*, pp 2205-2209.
- Morss, L.R., Edelstein, N.M., Fuger, J.; eds. *The Chemistry of the Actinide and Transactinide Elements*; Springer: The Netherlands, 2006, p 326, 3308.
- Moulin, C.; Decambox, P.; Moulin, V.; Decaillon, J. G. Uranium Speciation in Solution by Time-Resolved Laser-Induced Fluorescence. *Anal. Chem.* **1995**, *67*, pp 348-353.
- National Council on Radiation Protection and Measurements (NCRP) Report 58. *Handbook of Radioactivity Measurement Procedures*. 2nd ed.; NCRP Publications: Bethesda, MD, 1985.
- Noyes, K.L.; Draye, M.; Favre-Reguillon, A.; Foos, J.; Guy, A.; Czerwinski, K.R. Synthesis and evaluation of uranium and thorium imprinted resins. *Materials Research Society Symposium Proceedings* **2002**, *713*(Scientific Basis for Nuclear Waste Management XXV), pp 901-906.
- Preetha, C.R.; Gladis, J.M.; Rao, T.P.; Venkateswaran, G. Removal of Toxic Uranium from Synthetic Nuclear Power Reactor Effluents Using Uranyl Ion Imprinted Polymer Particles. *Environ. Sci. Technol.* **2006**, *40*(9), pp 3070-3074.
- Ryskin, N.N.; Dorenbos, P.; van Eijk, C.W.E.; Batygov, S.Kh. Scintillation properties of $\text{Lu}_3\text{Al}_{5-x}\text{Sc}_x\text{O}_{12}$ crystals. *J. Phys.: Condens. Matter* **1994**, *6*, pp 10423-10434.
- Sakuraba, S.; Matsushima, R. Photochemical Reactions of Uranyl Ions with Organic Compounds. IV. The Uranyl Fluorescence Quenching by Aliphatic Alcohols. *Chem. Soc. Jap.* **1971**; *44*(11), pp 2915-2918.
- Say, R.; Ersoez, A.; Denizli, A.. Selective Separation of Uranium Containing Glutamic Acid Molecular-Imprinted Polymeric Microbeads. *Sep. Sci. Technol.* **2003**, *38*(14), pp 3431-3447.

- Shleien, B.; Slaback L.A.; Birky, B.K.; eds. *Handbook of Health Physics and Radiological Health*, 3rd ed.; Lippincott Williams & Wilkins: Baltimore, MD, 1998, pp 3-5, 5-50.
- Skoog, D.A.; Holler, F.J.; Crouch, S.R. *Principles of Instrumental Analysis*, 6th ed.; Thomson Brooks/Cole: Canada; 2007; pp 132, 254-255, 368-370, 399-410.
- Spiers, F.W. Effective Atomic Number and Energy Absorption in Tissues. *Brit. J. Radiology* **1946**, 19, p 52.
- Syt'ko, V.V.; Umreiko, D.S. Spectroscopic Properties and Electronic Structure of Uranyl Complex Compounds (Review). *Journal of Applied Spectroscopy* **1998**, 65(6). pp 857-870.
- Tsoufanidis, N. *Measurement and Detection of Radiation*, 2nd ed.; Taylor & Francis: Washington, DC, 1995; p 222.
- Valeur, B. *Molecular Fluorescence*; Wiley-VCH: Weinheim, Germany, 2002; pp 77-90.
- Wheeler, J. and Thomas, J. K. Photochemistry of the uranyl ion in colloidal silica solution. *J. Phys. Chem.* **1984**, 88(4), pp 750 – 754.
- Zorenko, Y.; Gorbenko, V.; Voloshinovskii, A.; Stryganyuk, G.; Nedilko, S.; Degoda, V.; Chukova, O. Luminescence of Sc-related centers in single crystalline films of Lu₃Al₅O₁₂ garnet. *Phys. Status Solidi C: Conferences and Critical Reviews* **2005**, 2(1), pp 105-108.

VITA

Graduate College
University of Nevada, Las Vegas

Craig-Alan Crawford Bias

Home Address:

101 Haskin Road
San Antonio, Texas 78209

Degrees:

Bachelor of Science, Astrophysics, 1989
Michigan State University

Master of Engineering, Environmental Engineering, 1995
Old Dominion University

Master of Science, Health Physics, 2002
Colorado State University

Special Honors and Awards:

U.S. Air Force Meritorious Service Medal, 2005

U.S. Air Force Health Physicist of the Year, 2004

Air Force Material Command Health Physicist of the Year, 2004

Outstanding M.S. Candidate in Radiological Health Sciences, 2002

Dissertation Title: Enhanced Detection of Induced Fluorescence from Residual
Radioactive Materials

Dissertation Examination Committee:

Chairperson, Kenneth Czerwinski, Ph. D.
Committee Member, Kenton Moody, Ph. D.
Committee Member, Cynthia-May Gong, Ph. D.
Graduate Faculty Representative, Ralf Sudowe, Ph. D.